A test of the gravitational inverse-square law at short distance

Ted S. Cook

A dissertation
submitted in partial fulfillment of the
requirements for the degree of

Doctor of Philosophy

University of Washington

2013

Reading Committee:

Eric G. Adelberger, Chair

Jens H. Gundlach

Blayne R. Heckel

Program Authorized to Offer Degree:
Department of Physics

University of Washington

Abstract

A test of the gravitational inverse-square law at short distance

Ted S. Cook

Chair of the Supervisory Committee:
Professor Eric G. Adelberger
Department of Physics

Proposed theories that unify gravity and quantum mechanics often require Newton's gravitational inverse-square law to fail below some length scale. Additionally, some theorists have proposed the discovery of Dark Energy may imply altered gravitational dynamics at short length scales. These facts motivated our previous and continued efforts to test gravity at the smallest achievable distances.

This dissertation describes an improved test of gravity using a torsion pendulum and attractor designed with 120-fold azimuthal symmetry. We tested the inverse-square law at separations down to 60 μm and have excluded gravity-strength Yukawa interactions with length scale $\lambda > 42$ μm at the 95% confidence level. However, our data preferred the inclusion of a Yukawa potential at longer length scales, in a region of parameter space previously excluded by experiment, indicating some yet unresolved systematic issues. This dissertation provides a complete description of the experiment and gives guidance for improved future measurement.

TABLE OF CONTENTS

Page

LIST OF FIGURES

LIST OF TABLES

ACKNOWLEDGMENTS

There are many individuals who were indispensable in the completion of this work. Eric Adelberger, Blayne Heckel, Dan Kapner, C.D. Hoyle and Erik Swanson were an amazingly competent group of colleagues whose fingerprints are all over this experiment (figuratively and, I suppose, literally), without whose help and instruction this endeavor would not have proceeded. I must acknowledge the exquisite skill and patience of machinists Hank Simmons and Ted Ellis. I want to thank all the many members of the Eöt-Wash group who have helped and challenged me over my graduate career (there have been too many to name), they are truly an extraordinary group of individuals. The staff at CENPA were always a joy to work with, and I credit the lunchtime trivia crew for preserving of my sanity.

I also thank my parents for years of love, support, and encouragement. My wife Beth for being my #1 cheerleader, the loveliest of distractions, and for patiently enduring. And Darcy and Sam, who are a boundless source of joy.

Chapter 1

INTRODUCTION

Gravity stands alone among the known forces in having no quantum description. For decades, theoretical physicists have been proposing new quantum theories of gravity in the hope of unifying gravity with the rest of standard model physics. As recently as the late 1990s, modifications to gravity that would unify physics were generally assumed to occur near the Planck length scale (10^{-35} m), beyond the reach of any experiment yet devised.

Then in 1998, developments in string theory prompted theorists to suggest gravity may behave quite differently at scales much larger than Planck. In fact, mechanisms may exist for gravity to behave differently at scales as large as a millimeter that would not have been detected by any experiment yet performed. This revelation prompted the Eöt-Wash Group here at the University of Washington to do a test the inverse-square law of gravity (ISL) at length scales below 1 mm.

The work presented here is the Eöt-Wash Group's latest achievement in testing the ISL at short length scales.

1.1 Theoretical Motivations

1.1.1 Large Extra Dimensions

The 1998 paper that started this recent interest in testing the ISL argued the extra spatial dimensions of String- and M-theory, which were traditionally assumed to be highly compactified loops with characteristic scale near the Planck length, were in fact free to be arbitrarily large, limited only by known ISL constraints [2]. This proposal raised two exciting prospects. First, these large extra dimensions provided an elegant mechanism for explaining why the force of gravity is so weak in comparison to the other forces: it is diluted

into higher-dimensional space. Second, it provided the potential for an experimental result that could verify String theory (or at least elements of it), a popular theory which has long been derided for making no testable predictions.

As only the force of gravity is free to probe these extra dimensions (all other forces are confined to the 3-brane that makes up our conventional 3-dimensional universe), their presence, though possibly macroscopic in scale, would be hidden from everyday experience. If we measured gravity at length scales these extra dimensions occupy, the force would morph from an inverse-square law (indicative of 3-spatial dimensions) to an inverse-cube, or high order, law, depending on the number of dimensions encountered.

1.1.2 Cosmological Constant

The cosmological constant (or dark energy) that appears to be pushing the universe apart is not understood except in its phenomenological impact. It has been measured through redshift observations of Type 1a supernovae, and the cosmic microwave background anisotropies, to have a characteristic length scale of ~ 80 μm. Because the phenomenon appears (anti) gravitational in effect, this length may indicate a new fundamental length scale of gravity [3]. If this is the case, probing the ISL below this scale should reveal a change in gravitational physics.

1.1.3 Fat Gravitons

R. Sundrum further proposed a mechanism that explains why the observed cosmological constant is as small as it is [4](quantum vacuum calculations suggest it should be as much as 120 orders of magnitude larger). Rather than being essentially point-like, gravitons may be in fact fuzzy, or fat. This fuzziness prevents them from mediating forces at length scales smaller than their size, and provides an integration limit to the quantum vacuum calculations that bring them in line with observation. This theory predicts that gravity would become weaker below the dark energy length scale.

1.1.4 Chameleons and Other Exotic Particles

A peculiar class of particles that exhibit short-ranged interactions are known as chameleons [5]. These particles have a mass and coupling strength that scales with the density of their local environment. Short-ranged gravity experiments, which by design place high density regions in close proximity to each other, are well suited for detecting these particles.

There are also a wide range of proposed particles (dilaton, radion, moduli), mostly arising from various String theories, that would mediate new forces over short distances. Any of these are potentially detectable as deviations of the ISL.

1.2 A Brief History of ISL Tests

1.2.1 Yukawa Parameterization

The standard parameterization of non-Newtonian physics uses the Yukawa potential. The Newtonian potential of a point mass, whose gradient gives rise to the ISL, is

$$V_N = -\frac{\mathrm{G}m}{r}. \tag{1.1}$$

The Yukawa potential is expressed in terms of the Newtonian potential

$$V_Y = V_N \; \alpha e^{-r/\lambda} \; , \tag{1.2}$$

and introduces new physics with a strength α relative to V_N that "turns on" for separations r less than the characteristic length scale λ. Experiments searching for ISL deviations compare their data against calculations from the combined potential

$$\begin{aligned} V &= V_N + V_Y \\ &= V_N \left(1 + \alpha e^{-r/\lambda}\right) \; , \end{aligned} \tag{1.3}$$

with α as a free fit paramter for a given choice of λ. Figure 1.1 shows experimental limits placed on the $(\lambda, |\alpha|)$ parameter space for Yukawa deviations across a wide range of length scales.

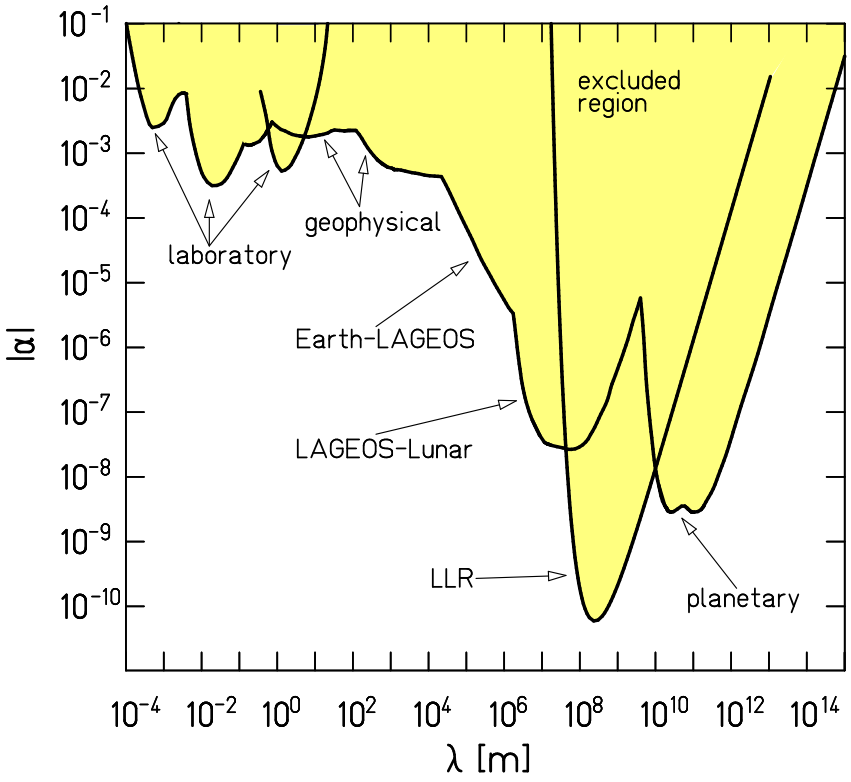

Figure 1.1: 95% exclusions on α for various ranges of λ. The most precise verification of the ISL comes from lunar laser ranging near $\lambda = 10^8$ m, which precisely studies the orbit of the moon around the earth and sun. Limits from the experiment described in this thesis come at the far left of this plot, in the $\lambda = 10^{-5}$ to 10^{-4} m range.

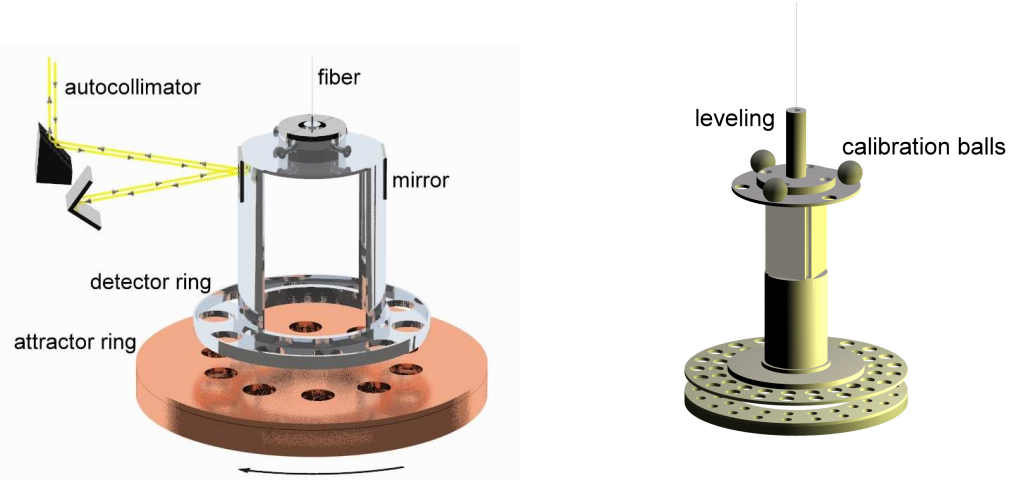

Figure 1.2: Illustrations of previous Eöt-Wash balances. LEFT: The 10-fold symmetric pendulum and attractor of Hoyle[1]. Gravitationally induced oscillations of the pendulum were monitored with the autocollimator. RIGHT: The 21-fold symmetric pendulum and attractor of Kapner[6]. This experiment introduced a continuous calibration mechanism and more sophisticated leveling adjustment.

1.2.2 Eöt-Wash Experiments

The Eöt-Wash Group has so far published two experimental tests of the ISL that used torsion pendulums to measure gravitationally induced twists [1][6]. As illustrated in Figure 1.2, these experiments employed horizontal planar disks – a rotating attractor and a suspended detector ring on the pendulum – with holes removed in a rotationally periodic pattern. If the holes were not present, the gravitational force between the disks would merely pull normal to the near surfaces and cause no twist. The m-fold symmetric holes allow gravity to apply a torque on the pendulum's detector ring, so a full rotation of the attractor induced m oscillations of the pendulum. The gravitational interaction can be mathematically modeled simply as cylinders with negative mass. The planar geometries allowed for small attractor-pendulum separations which probed gravity at short distance.

Some key elements of these experiments were

- Suspension fiber : These were made of tungsten which provided high oscillation quality factors, $Q \approx 3000$, and high breaking strengths. They were about 80 cm in length,

and 20 μm in diameter. The torsional spring constant of the fiber, κ, set the twist-to-torque scale.

- Autocollimator : This monitored the pendulum's twist by bouncing a laser beam off the pendulum's mirror and detecting it on a split photo-diode.
- Electrostatic screen : A thin beryllium-copper foil, 10 μm thick, was stretched between the attractor and pendulum to shield electrostatic communication between them. Without this shield, patch charges on the surfaces of the pendulum and attractor would have overwhelmed the experiments.

These two experiments hold the distinction of placing the shortest constraints on $|\alpha| \leq 1$, confirming the ISL to 200 μm and 56 μm, respectively. Their 95% exclusion constraints on α and λ are shown if Figure 1.3.

1.3 Fourier-Bessel Experiment

This thesis describes the Fourier-Bessel experiment (so named for our torque solution which had angular-Fourier and radial-Bessel functions (Chapter 2)) which had a goal of testing the ISL to below 50 μm.

1.3.1 Design

The pendulum was designed to be smaller and lighter than previous measurements, while using denser active materials. The design of the experiment departed from our earlier measurements in four key ways:

- The removed masses were pie-shaped slots.
- The rotational symmetry was considerably greater.
- There was a single, un-cancelled, attractor disk.
- There were two pattern symmetries.

Slots

The hole geometry of our previous experiments was dictated largely by engineering considerations: round holes are easy to make and easy to measure. But the hole geometry was

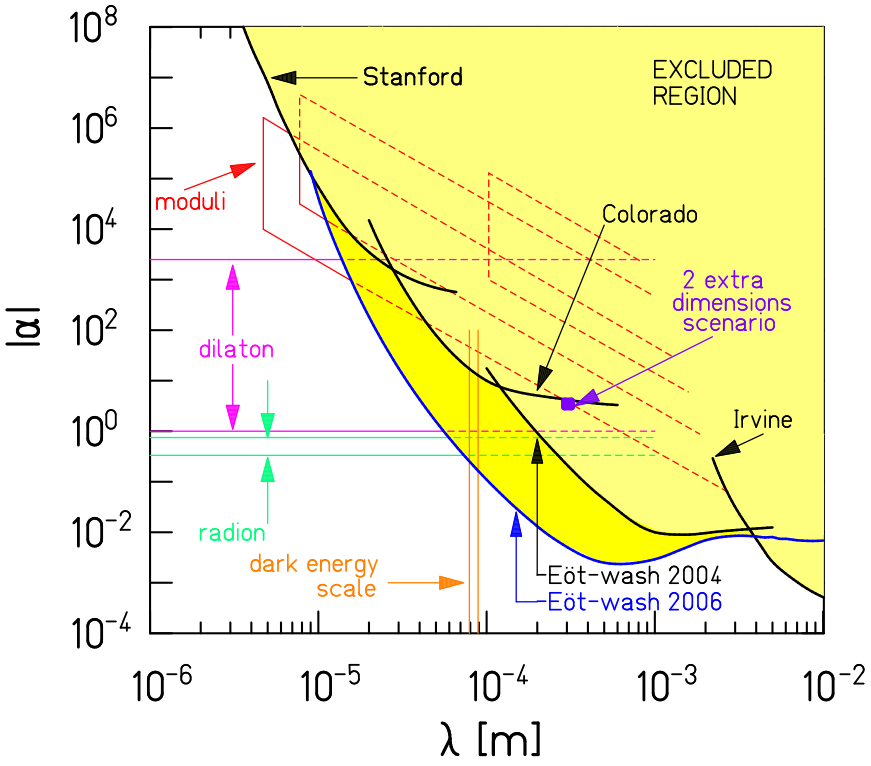

Figure 1.3: Previous short-ranged ISL constraints. The Eöt-Wash 2004 line was from [1], and the Eöt-Wash 2006 line came from [6].

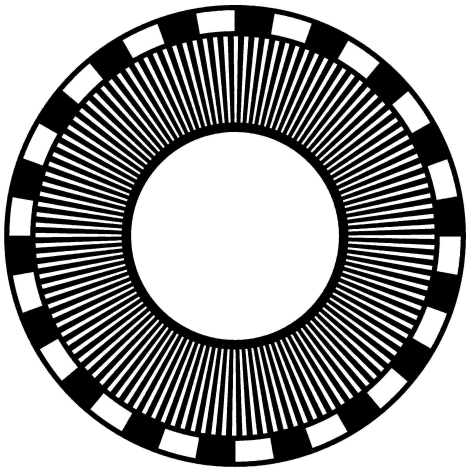

Figure 1.4: Slot pattern used for both the Fourier-Bessel pendulum and attractor. The interior slots have 120-fold symmetry and are sensitive to new short-ranged physics. The exterior slots have 18-fold symmetry and are insensitive to new short-ranged physics, providing a systematic check to our measurements. The patterns were cut from 0.05 mm thick tungsten foils.

not ideal for measuring short-ranged physics.

The torque on the pendulum from a rotating attractor goes like the derivative of the interaction energy, U, with respect to ϕ, the rotation angle of the attractor (Equation 2.5). For a fixed separation distance, s, between the attractor and pendulum that is small relative to the dimension of the holes, and for a short-ranged $\tilde{U}(r)$ that "turns on" for $r \leq s$, the interaction energy is essentially proportional to the overlap area, A, of material in the pendulum and attractor. The short-ranged torque, $\tilde{T}$, is then

$$\tilde{T}(\phi) \propto \frac{\partial A}{\partial \phi} \, . \tag{1.4}$$

In other words, to maximize the torque sensitivity of the experiment to short-ranged interactions, we wanted to maximize the change in overlap area for a given change in attractor angle. The pie-shaped slots of the Fourier-Bessel experiment (Figure 1.4) are clearly favored over cylindrical holes for this reason.

High Symmetry

Equation 1.4 similarly leads to the observation that $\tilde{T} \propto m$, where m is the rotational symmetry number. If half the area in the pattern is comprised of equally spaced slots, then the angle to transition from total overlap to no overlap is π/m. E.g. a pattern with 10 slots is twice as sensitive to short-ranged torques as a pattern with 5 slots.

The Fourier-Bessel experiment employed a 120-fold symmetric pattern to take advantage of this fact. The choice of 120 came primarily from engineering considerations, limited by the minimum slot width we were capable of machining. Additionally, the choice of 120 allowed for analyzing our data in cuts equal to 60° of attractor rotation.

Single Attractor

Our previous measurements employed two-part attractors. The plate closest to the pendulum provided short-ranged interactions, and the plate farther from the pendulum, with hole pattern rotated out of phase, provided long-ranged gravity cancellation to prevent signal amplitudes overwhelming the detector. The addition of the bottom plate, which was necessitated by the large thicknesses of the pendulum and top attractor plate ($\geq$ 1 mm), complicated both construction and analysis of the experiments.

The Fourier-Bessel experiment used a pendulum and attractor both cut from 0.05 mm thick tungsten foils. The thickness was chosen to coincide with our goal of testing the ISL below 50 μm. Thicker foils would have added unwanted long-ranged gravitational signal without appreciably increasing our sensitivity to physics below 50 μm. The thinness of the foils kept the signal sizes at manageable levels and removed the need for a second attractor to provide cancellation.

The thinness of the foils also meant that, unlike previous measurements, the pendulum and attractor were not self-supporting. Therefore, the foils were glued to flat Pyrex disks that provided structural stability. Unfortunately, the gluing requirement introduced perhaps as many complications to the construction and analysis of the experiment (Chapter 5) as forgoing a second attractor avoided.

Two Patterns

The pendulum and attractor foils additionally had an 18-fold slot pattern. This provided a second, simultaneous torque measurement that shared in common with the 120-fold pattern many of the same physical parameters (density, xyz-location, etc.), but had a vastly decreased sensitivity to short-ranged physics due to its lower symmetry. This provided a systematic check for the experiment. If the experiment were to uncover new short-ranged physics, we would expect it to appear only in the 120ω signal. It also served simply as a sanity check. Given that this experiment was quite different from our previous efforts in terms of geometry and construction, being able to accurately measure and fit a signal that we knew should not experience any new physics would build confidence in our methods.

18 was chosen as the symmetry number to be as different from 120 as possible, while maintaining divisibility by six for data-cutting, but without being a sub-harmonic of 120 to avoid signal pollution.

1.3.2 Data Sets

As of the writing of this thesis, we have taken three complete sets of data with the Fourier-Bessel setup – termed W1, W2, and W3. We experienced numerous setbacks as we embarked on the W1 data set, but we made many needed changes to critical apparatus and achieved incremental improvements in sets W2 and W3. The third set of data achieved much improved statistical errors (Figure 7.2), had the most complete collection of relevant environmental sensor data, and was followed by a thorough systematics investigation. For these reasons, this thesis refers almost exclusively to the data, procedures, analysis, etc. of the W3 data set. Additionally, because of the improved error bars of W3, and various gaps in information for W1 and W2, only W3 was used to place new limits on the ISL.

Chapter 2

CALCULATION OF THE PREDICTED NEWTONIAN AND YUKAWA TORQUES

This chapter describes the derivation of the analytic Fourier-Bessel solution for calculating torques when the attractor and pendulum are co-axial, the numerical solutions for calculating torques when the pendulum is off-center, and the development of empirical off-center functions.

The on-center Fourier-Bessel solution described below was used with the full pendulum and attractor models (Chapter 5) to calculate look-up tables of expected torques given a set of adjustable parameters (Section 5.3).

The empirical off-center functions (Section 2.3) calculated the *relative* impact of moving the pendulum off-center, and were built from off-center calculations (Section 2.2) that used simplified versions of the pendulum and attractor models. This method of off-center calculation kept the first-order scaling effects of the adjustable parameters (torque tables), without complicating the off-center calculations with parameters whose effect would be at most second-order to the relative shape.

2.1 On-Center Fourier Bessel Solution

This derivation of the torque solution was originally suggested by George Bertsch, applied by Blayne Heckel and subsequently typed up in [7]. I will briefly reproduce the highlights of that work as it applies to this experiment.

Both Newtonian and Yukawa potentials are special solutions of the modified Helmholtz equation,

$$\left(\nabla^2 - \mu^2\right) V(\vec{r}) = -\rho(\vec{r}) \tag{2.1}$$

which, for a potential that vanishes at infinity and is finite near the origin, has a Green's

function solution

$$G(\vec{r},\vec{r}\,') = \frac{e^{-\mu|\vec{r}-\vec{r}\,'|}}{|\vec{r}-\vec{r}\,'|} \ , \tag{2.2}$$

where $G(\vec{r},\vec{r}\,')$ satisfies the equation

$$\left(\nabla^2 - \mu^2\right) G(\vec{r},\vec{r}\,') = -4\pi\ \delta(\vec{r}-\vec{r}\,'). \tag{2.3}$$

The Newtonian solution corresponds to $\mu = 0$ and the Yukawa solution to $\mu = 1/\lambda$.

We can calculate the energy U of the attractor-pendulum system by integrating the Green's functions over the density functions of the attractor and pendulum

$$U(\phi) = -\mathrm{G}\int \mathrm{d}^3r\ \rho_{\mathrm{pen}}(\vec{r}) \int \mathrm{d}^3r\,'\ \rho_{\mathrm{att}}(\vec{r}\,',\phi)\ G(\vec{r},\vec{r}\,') \ . \tag{2.4}$$

The energy is a function of the attractor rotation angle ϕ and we can calculate the torque by taking the derivative,

$$T(\phi) = -\frac{\partial U(\phi)}{\partial \phi}. \tag{2.5}$$

To solve Equation 2.4, we start out by rewriting Equation 2.3 explicitly in cylindrical coordinates

$$\left(\frac{1}{r}\frac{\partial}{\partial r}r\frac{\partial}{\partial r} + \frac{1}{r^2}\frac{\partial^2}{\partial\theta^2} + \frac{\partial^2}{\partial z^2} - \mu^2\right) G(\vec{r},\vec{r}\,') = 4\pi\ \frac{1}{r}\delta(r-r')\ \delta(\theta-\theta')\ \delta(z-z') \ . \tag{2.6}$$

Knowing that the solution must be zero far away and finite near the origin, we can use the identities,

$$\delta(\theta-\theta') = \frac{1}{2\pi}\sum_{m=-\infty}^{\infty} e^{im(\theta-\theta')} \ , \tag{2.7}$$

$$\delta(z-z') = -\left[\frac{\partial^2}{\partial z^2} - k^2 - \mu^2\right]\frac{e^{-\sqrt{k^2+\mu^2}(z_>-z_<)}}{2\sqrt{k^2+\mu^2}} \ , \tag{2.8}$$

and

$$\frac{1}{r}\delta(r-r') = \int_0^\infty \mathrm{d}k\ k\ J_m(kr)\ J_m(kr') \ , \tag{2.9}$$

along with Bessel's differential equation,

$$\left(x\frac{\partial}{\partial x}x\frac{\partial}{\partial x} + k^2x^2 - m^2\right)\ J_m(kx) = 0, \tag{2.10}$$

to show that

$$G(\vec{r},\vec{r}\,') = \sum_{m=-\infty}^{\infty} e^{im(\theta-\theta')}\int_0^\infty \mathrm{d}k\ k\ J_m(kr)\ J_m(kr')\ \frac{e^{-\sqrt{k^2+\mu^2}(z_>-z_<)}}{\sqrt{k^2+\mu^2}}. \tag{2.11}$$

Throughout this chapter unprimed coordinates $\vec{r}$ refer to the pendulum, and primed coordinates $\vec{r}\,'$ refer to the attractor. Since the z-axis points vertically upward and the pendulum is above the attractor, $z_> = z$ and $z_< = z'$. Our expression for the energy (Equation 2.4) now becomes

$$U_m(\phi) = -\frac{\mathrm{G}}{4\pi}\int_0^\infty \mathrm{d}k \frac{k}{\sqrt{k^2+\mu^2}}\; I_m(k)\; I_m^{'}(k,\phi)\;, \tag{2.12}$$

where we have separated pendulum and attractor coordinates into

$$I_m(k) \equiv \int \mathrm{d}^3 r\; \rho_{\mathrm{pen}}(\vec{r})\; e^{-im\theta}\; J_m(kr)\; e^{+\sqrt{k^2+\mu^2}z} \tag{2.13}$$

$$I_m^{'}(k,\phi) \equiv \int \mathrm{d}^3 r'\; \rho_{\mathrm{att}}(\vec{r}\,')\; e^{+im(\theta'-\phi)}\; J_m(kr')\; e^{-\sqrt{k^2+\mu^2}z'}. \tag{2.14}$$

To calculate these integrals we must choose the general form of the density functions ρ_{pen} and ρ_{att}. If we choose them to be N-fold rotationally symmetric about the z-axis sets of annulur sectors (wedges), then Equations 2.13 and 2.14 become analytically solvable. Let r_1 and r_2 be the wedge inner and outer radii, h the z-offset of the wedge's vertical center, t the vertical half thickness, β the half angle in θ subtended by a wedge, and θ_0 the offset in θ of one of the wedges. With H representing the Heaviside step function, and

$$\begin{aligned}\Psi(\vec{r}) \equiv\; & [H(r-r_1) - H(r-r_2)]\; [H(z-h+t) - H(z-h-t)]\; \times \\ & \sum_{n=1}^{N}\left[H\left(\theta-\theta_0-\frac{2\pi n}{N}+\beta\right) - H\left(\theta-\theta_0-\frac{2\pi n}{N}-\beta\right)\right]\;,\end{aligned} \tag{2.15}$$

the density functions take the general form $\rho = \sum \rho_j \Psi_j$, where each j is a single layer of wedges with independently defined $r_1,\ r_2,\ h,\ t,\ \beta,$ and θ_0. Equations 2.13 and 2.14 can be analytically integrated, giving

$$I_m(k) = \sum_j \frac{2N\rho_j}{m\gamma}\sin(m\beta_j)e^{-im\theta_{0j}}\;\sinh(t_j\gamma)e^{+h_j\gamma}\; R_m^{(1)}(r_{1j}, r_{2j}, k) \tag{2.16}$$

$$I_m^{'}(k,\phi) = \sum_j \frac{2N\rho_j}{m\gamma}\sin(m\beta_j)e^{+im(\theta_{0j}-\phi)}\;\sinh(t_j\gamma)e^{-h_j\gamma}\; R_m^{(1)}(r_{1j}, r_{2j}, k)\;, \tag{2.17}$$

where $\gamma \equiv \sqrt{k^2+\mu^2}$ and

$$R_m^{(1)}(r_1, r_2, k) = \frac{2m}{k}\sum_{i=0}^{\infty}\frac{m+2i+1}{(m+2i)(m+2i+2)}\left(r_2 J_{m+2i+1}(kr_2) - r_1 J_{m+2i+1}(kr_1)\right)\;. \tag{2.18}$$

These solutions are zero unless $m = Nl$. Therefore, the torque amplitude at the lth harmonic of the signal frequency is

$$T_{Nl} = -\left.\frac{\partial U_{Nl}(\phi)}{\partial \phi}\right|_{\phi_0} = NlU_{Nl}(\phi_0) \ , \tag{2.19}$$

where ϕ_0 is the attractor angle that maximizes the energy.

The Fourier-Bessel solution gives a nearly analytic solution for calculating torque amplitudes at particular signal frequencies of the attractor rotation. An infinite sum (Equation 2.18) and an integral over an infinite range (Equation 2.12) must be numerically evaluated. The calculation requires *a priori* knowledge of ϕ_0 when defining the mass distribution models, which is trivial for most geometries and corresponds to the pendulum and attractor being anti-aligned rotationally (or aligned, which merely introduces a negative sign).

The infinite sum of Equation 2.18 converges very quickly, so choosing a finite limit does not impact the accuracy of the Fourier-Bessel calculation. The infinite k integral of Equation 2.12 does not converge so quickly, however, so choosing an appropriate integration limit is necessary. Figure 2.1 plots the integrands for the 18ω and 120ω models and shows the error associated with truncating the integrals at various $k_{\max} < \infty$.

2.2 Off-Center Calculation

Moving the pendulum in the xy-plane breaks the cylindrical symmetry of the Fourier-Bessel solution and requires an alternate method for calculating the torques. We calculated the off-center torques with two very different integration methods as a way to check our work.

Both methods used Monte Carlo integration, meaning the solutions statistically approached stable values through random sampling of the integration variables. Each solution point was normally distributed about the unknown exact solution with an error bar indicating the calculation precision. Even though Monte Carlo integration is the most efficient method when integrating many variables [8], it can be an enormously time consuming calculation. To decrease error bars by a factor of n, the calculation time increases by n^2. For this reason, the integrations described below were performed on the *Athena* computer cluster, taking full advantage of its highly parallel architecture.

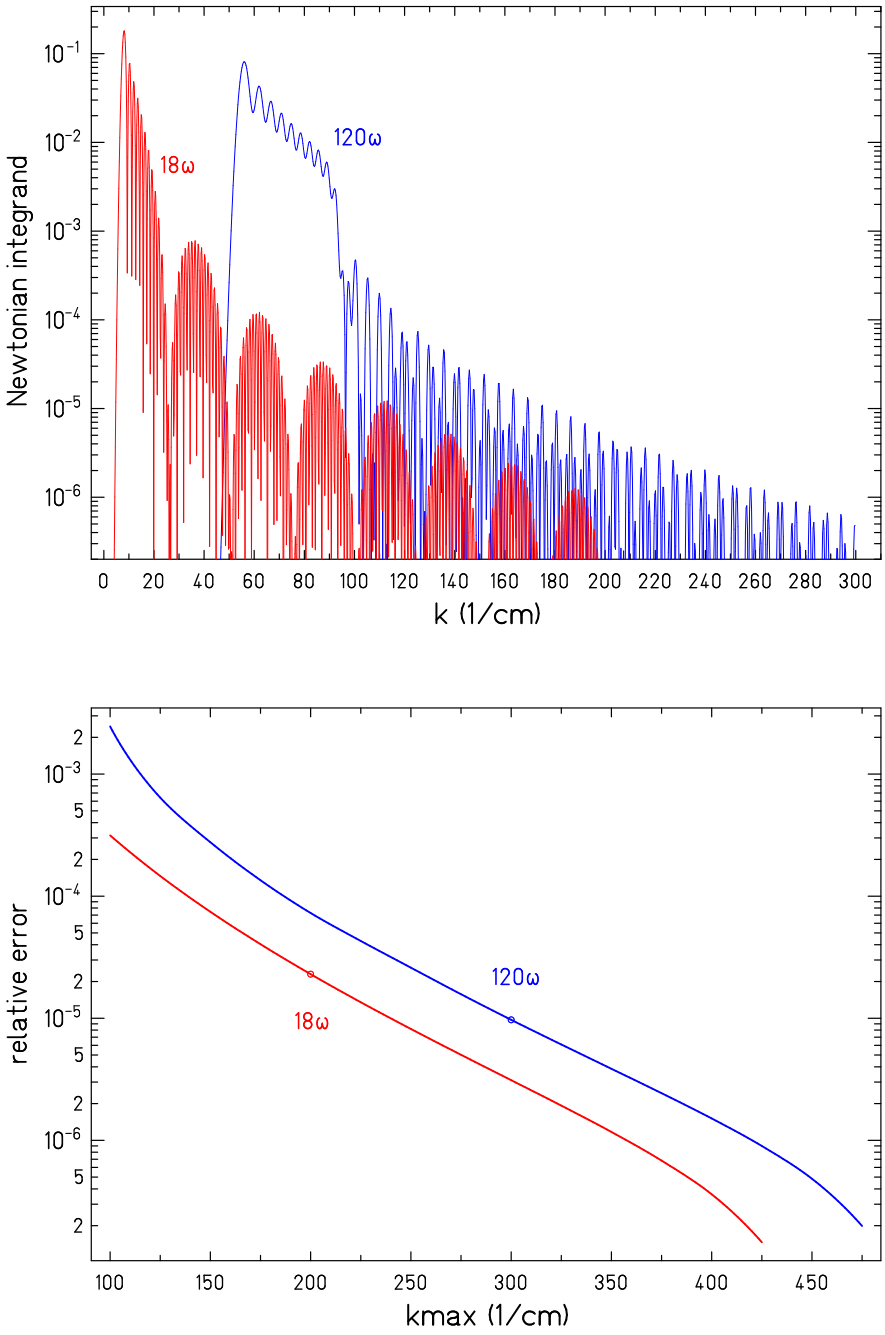

Figure 2.1: Numerical integrals of the on-center Newtonian Fourier-Bessel calculations. TOP: 18ω and 120ω FB integrands for $s = 0.050$ mm. The functions turn on very sharply for small k, but trail off slowly at large k. All 18ω calculations were integrated from $k = 1$ to 200 and all 120ω calculations were integrated from $k = 30$ to 300. BOTTOM: The relative error associated with different choices of $k_{\max}$. Larger values of $k_{\max}$ increased the calculation time, so values were chosen that provided adequate precision.

2.2.1 Cartesian Monte Carlo Integration

The simplest approach was to go back to the Cartesian form of the Green's function solution, Equation 2.2, and do a point by point integration of Equation 2.4. This method involves choosing a random point in the pendulum volume (x, y, z) and another in the attractor volume (x', y', z'). The energy is calculated between the two points for the attractor in-phase (ϕ_0) and out-of-phase $(\phi_0 + \pi/N)$, and the difference in energies is an estimate of the torque contribution of those points. This is repeated until both volumes have been adequately sampled. This procedure gives the *total* torque on the pendulum, but we are interested in the torque at particular harmonic frequencies. To extract the amplitude of a particular harmonic, the calculation must be repeated multiple times with a changing attractor phase in order to map the torque function and Fourier decompose it. The entire algorithm is repeated and averaged until the solution converges to the desired precision.

2.2.2 Fourier-Bessel Monte Carlo Integration

The other method is to retain as much of the on-axis Fourier-Bessel solution as possible and numerically integrate only those integrals that are no longer analytic. Moving the pendulum in the xy-plane breaks the r and θ analytic solutions of Equation 2.16, but the solution for z remains valid. The attractor by definition remains on-axis, so Equation 2.17 also remains valid. The calculation involves random sampling a single (r, θ) point in the pendulum volume then performing the k integral of Equation 2.12. This is repeated until the full pendulum volume is adequately sampled and the solution converges to the desired precision.

2.2.3 Comparison of Monte Carlo Methods

The CMC method had 6 Monte Carlo degrees of freedom and the need for Fourier decomposition. The FBMC method was much more efficient because it had only 2 Monte Carlo degrees of freedom (plus the k integral), and it gave the harmonic solutions directly. The FBMC converged about 18 times faster than the CMC for 120ω calculations, and upwards of 70 times faster for 18ω calculations. Figure 2.2 demonstrates that both methods gave statis-

tically equivalent torque solutions, providing confidence that we did not have programming errors.

2.3 Off-center Empirical Functions

The FBMC was used to develop empirical functions, $R_m(r_p, s, \lambda)$, that described the relative change in torque for $r_p > 0$ for $m = 18$ and $m = 120$. This was done to provide smooth fitting functions that were not randomly stepping around due to the scatter in the calculated points. For instance, occasionally an off-center calculation near $r_p = 0$ had an unphysical value greater than the on-center calculation (though within errors). Additionally, the uncertainty of the empirical functions benefited from the ensemble uncertainty (roughly $\sigma/\sqrt{N}$, where σ is the precision goal and N is the total number of calculations), whereas a simple linear interpolation between points would have had an uncertainty scaled only by the two nearest neighbors.

We calculated off-center torques for 15 points in r_p (from 0 - 0.28 mm), at 20 values of s (from 0.04 - 1 mm), and 38 values of λ (from 0.005 - 10 mm) plus Newton ($\lambda = \infty$). Newtonian torques were calculated with a fixed absolute precision goal for all values of s, which was chosen to be roughly equivalent to a pendulum twist amplitude of 0.5 nrad. Yukawa torques were calculated with a relative precision goal equal to 0.5% of the on-center value.

We constructed the following empirical functions based solely on their ability to fit the normalized calculations with no theoretical underpinning.

$$R_m(r_p, s, \lambda) = c_1 + (1 - c_1)\cos(r_p\ f_m(s, \lambda)) \tag{2.20}$$

$$f_m(s, \lambda) = c_2 + c_3\ e^{(c_4\ y_m(s,\lambda))} \tag{2.21}$$

$$y_m(s, \lambda) = \begin{cases} s & \text{Newton } (\lambda = \infty) \\ b_m(\lambda) + m_m(\lambda)s & \text{Yukawa} \end{cases} \tag{2.22}$$

$$b_m(\lambda) = c_5\ e^{(c_6\lambda)} \tag{2.23}$$

$$m_m(\lambda) = 1 - e^{(c_7\lambda)} \tag{2.24}$$

Values of the c_n coefficients for the $m = 18$ and $m = 120$ calculations are listed in Table 2.1.

Table 2.1: Coefficients for the empirical off-center torque functions, for s and λ in mm. We did not need to model the 18ω $c_5 - c_7$ coefficients as the signal was effectively insensitive to Yukawa torques.

coefficient	$m = 18$	$m = 120$	coefficient	$m = 18$	$m = 120$
c_1	0.5	0.367392	c_5	0	-0.203585
c_2	0.942844	4.92841	c_6	-1	-5.69768
c_3	0.24823	0.886262	c_7	$-\infty$	-7.55179
c_4	-3.78842	-1.0726			

The c_1 coefficients were chosen to have reasonable values, and all other c_n were the result of least-squares fitting. Alternative functions, or even just other c_n values, may provide a better fit to the calculations, but this formulation does an adequate job representing the calculated values.

Figures 2.3 and 2.4 show the Newtonian fits for $R_{120}(r_p, s, \infty)$ and $f_{120}(s, \infty)$. Figures 2.5, 2.6, and 2.7 show the Yukawa fits for $y_{120}(s, \lambda)$, $b_{120}(\lambda)$, and $m_{120}(\lambda)$. Figure 2.8 shows the calculated curves for 120ω $\lambda = 5$ μm, 120ω $\lambda = \infty$, and 18ω.

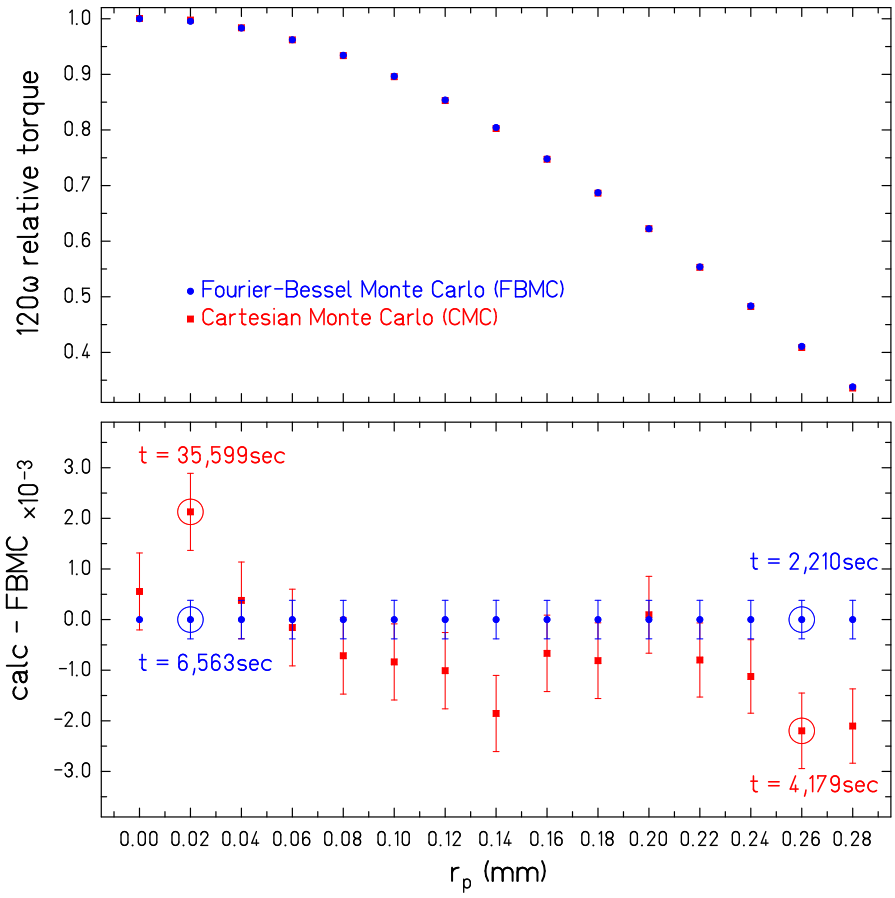

Figure 2.2: Comparison of 120ω Fourier-Bessel and Cartesian Monte Carlo Newtonian integrations for $s = 0.040$ mm. All points have been normalized by the on-center FB calculation. As noted on the plot, the FBMC achieved error bars half the size of the CMC in considerably shorter time. The apparent downward bias of the CMC solution is likely due to an insufficient number of points in the torque vs ϕ mapping for the Fourier decomposition.

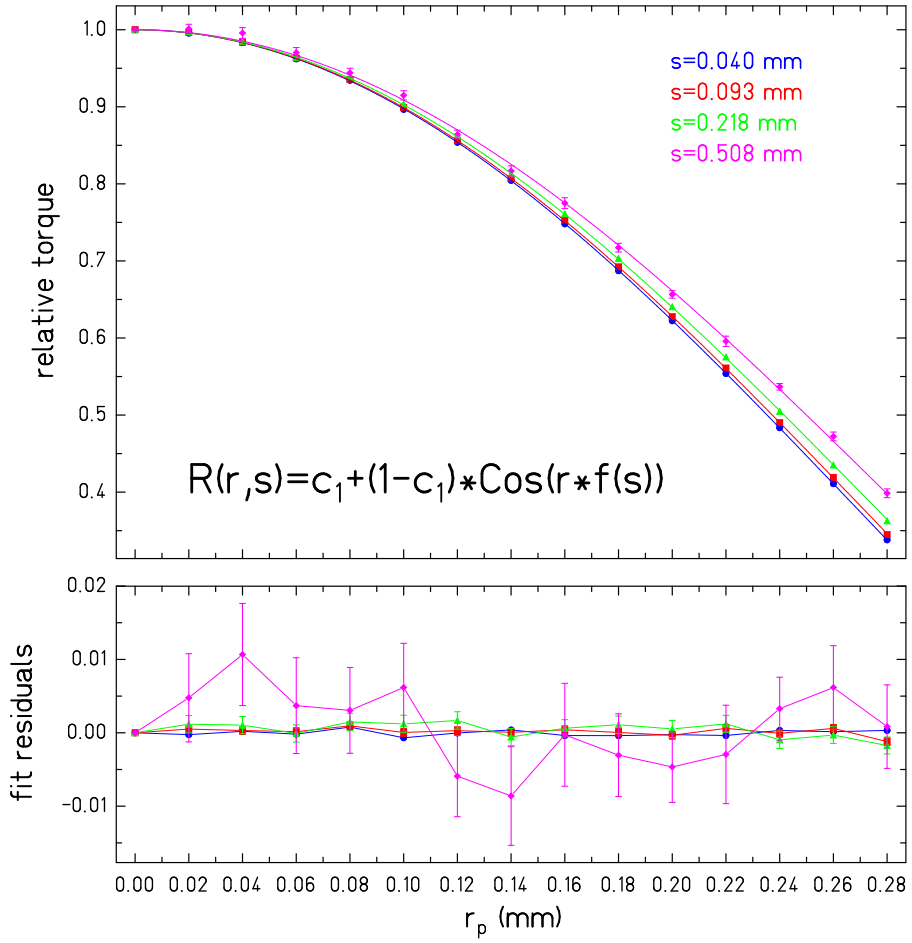

Figure 2.3: Off-center empirical function: $R_{120}(r_p, s, \infty)$. Four of the 20 s values calculated are shown. c_1 was assigned a constant value and f was the free fit parameter for each value of s. Relative error bars increase for larger s because we used an absolute precision requirement for Newtonian calculations.

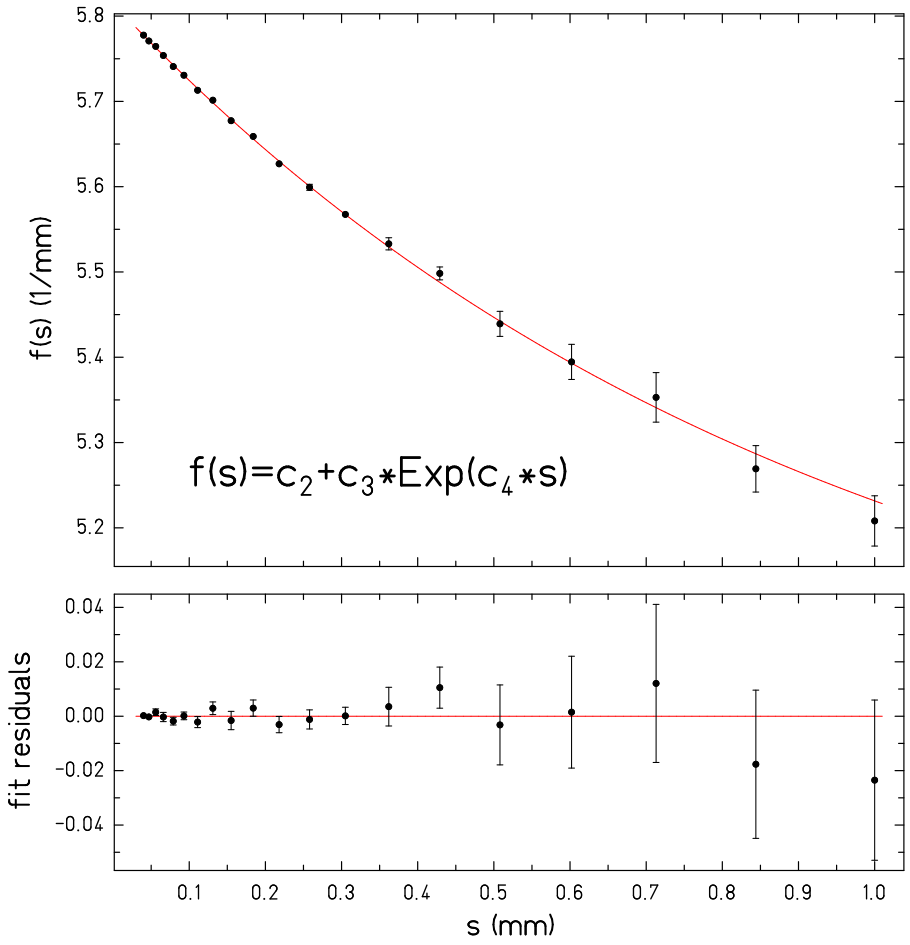

Figure 2.4: Off-center empirical function: $f_{120}(s, \infty)$. The points represent all the best-fit values of f from fitting Equation 2.20 at different values of s. For this fit, c_2, c_3, and c_4 were free fit parameters.

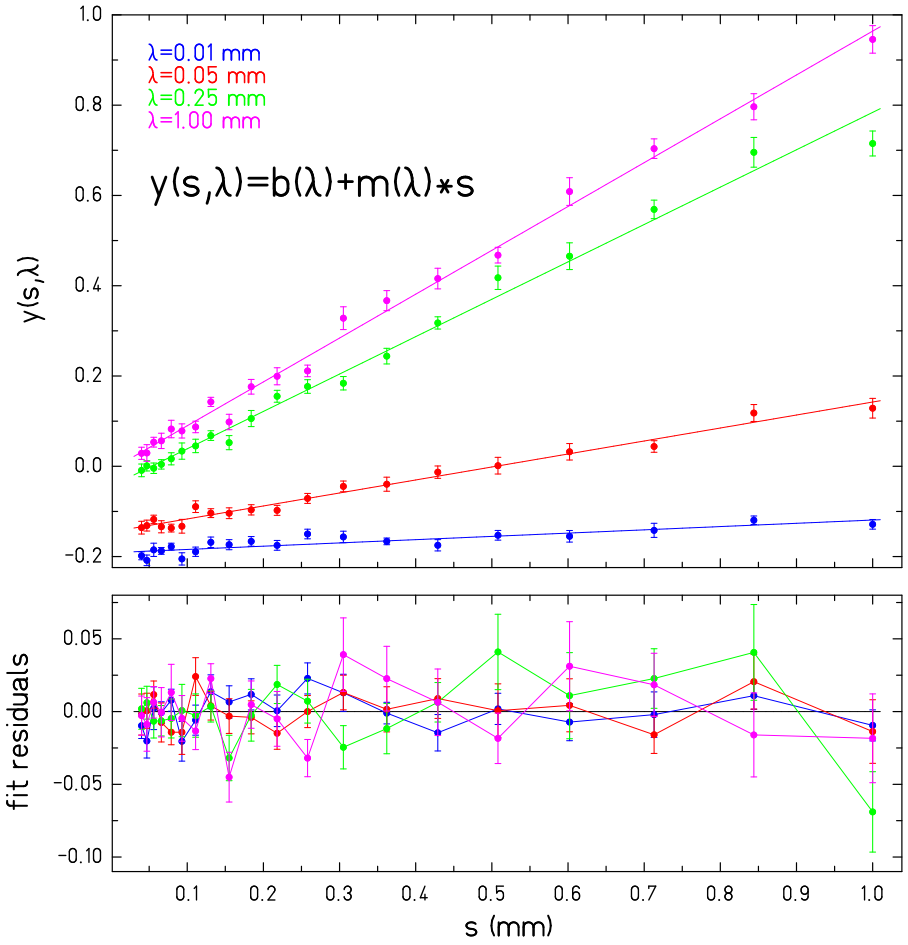

Figure 2.5: Off-center empirical function: $y_{120}(s, \lambda)$. With c_2, c_3, and c_4 fixed by Newtonian data (Figure 2.4), y in Equation 2.21 was a free fit parameter for each value of (s, λ), and those fits are the points plotted here. Four of the 38 λ values calculated are shown. b and m are free fit parameters for each value of λ.

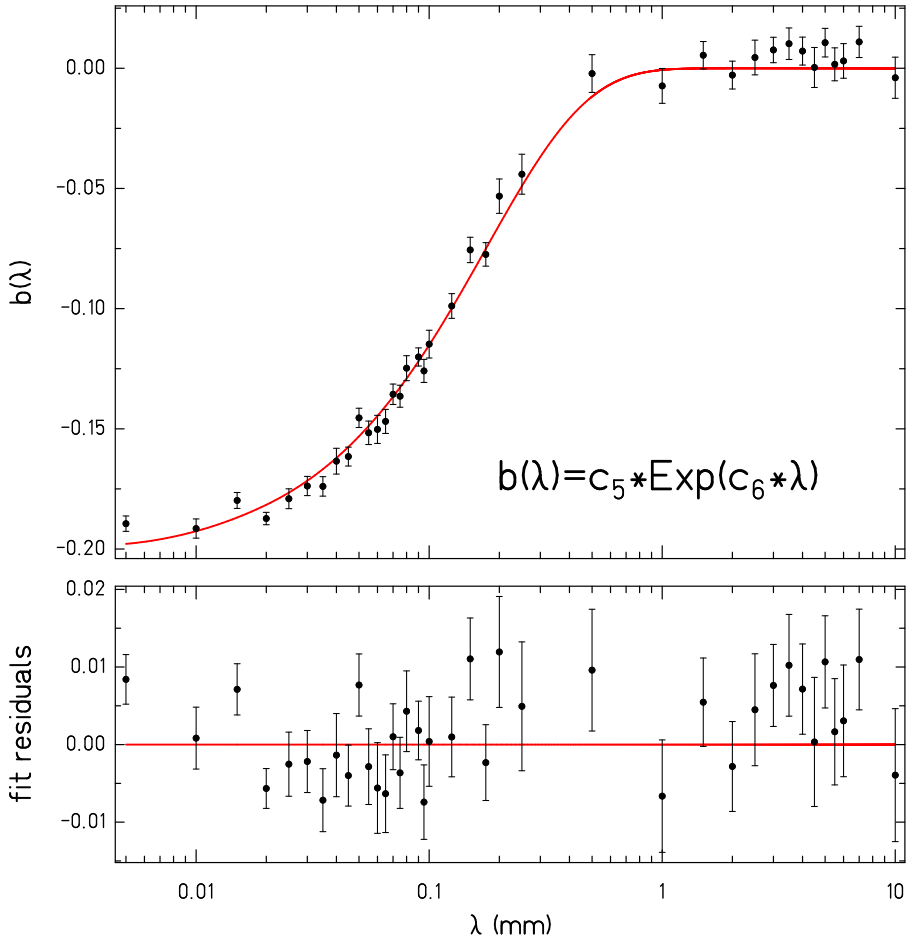

Figure 2.6: Off-center empirical function: $b_{120}(\lambda)$. The best-fit b values from Equation 2.22 are plotted for each λ calculated. While the values appear to favor a slight positive offset at long λ, the fitting function was chosen to have $b = 0$ at $\lambda = \infty$ for consistency with the Newtonian version of $y(s, \lambda)$.

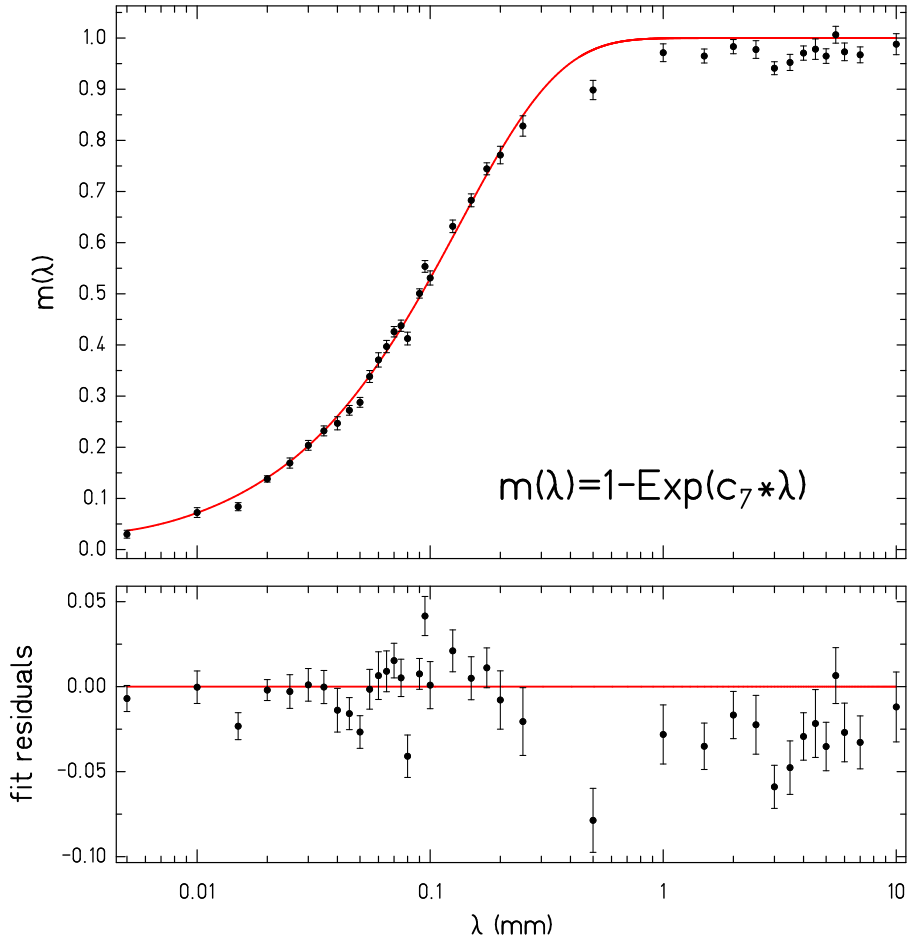

Figure 2.7: Off-center empirical function: $m_{120}(\lambda)$. The best-fit m values from Equation 2.22 are plotted for each λ calculated. While the values appear to favor a slight offset from 1 at long λ, the fitting function was chosen to have $m = 1$ at $\lambda = \infty$ for consistency with the Newtonian version of $y(s, \lambda)$.

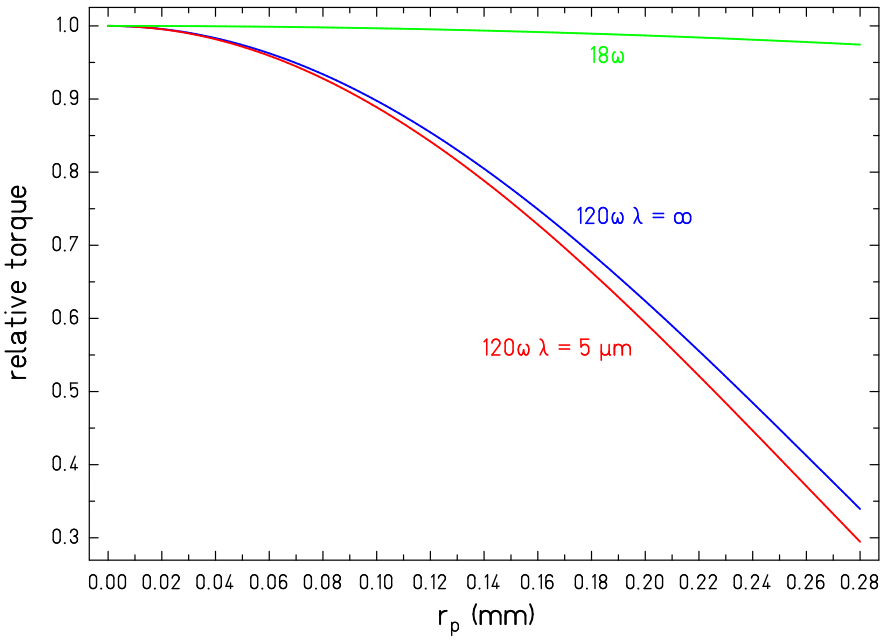

Figure 2.8: Off-center empirical function: calculated curves for $s = 0.050$ mm.

Chapter 3

APPARATUS UPGRADES

Much of the experimental infrastructure was already in place to perform our measurements as this project was a continuation of similar previous work. However, in addition to designing and building a new attractor-pendulum pair, many improvements were made to the supporting experimental systems. Nearly everything sitting below the torsion fiber (pendulum body, pendulum, electrostatic screen, attractor, bearing assembly, attractor drive, calibration turntable) was re-engineered. This chapter discusses the building of our pendulum and attractor and other essential improvements made to the apparatus.

Figure 3.1 gives an overview of the whole apparatus.

3.1 Pendulum and Attractor

The active masses of both the pendulum and attractor were made from 50 μm thick tungsten foils. The 18-fold and 120-fold slots were removed from the foils using an electric discharge mill (EDM). The foils were then glued, using Dow Integral E100 adhesive film, to 3 mm thick Pyrex glass substrates to provide structural support. Finally, the inner and outer radii of the foils were cut with the EDM.

3.1.1 Material Selection

Tungsten was chosen as the active mass because it has high density, is non-magnetic, and it was not cost-prohibitive to obtain flat foils. Other materials considered were Rhenium (could not source foils that met flatness requirement) and Platinum (cost-prohibitive).

Pyrex was chosen as the support substrate because it has low density (to minimize passive weight), high strength, high flatness, and has a coefficient of thermal expansion (CTE) that is close to, but less than, Tungsten. We also considered titanium, but found its higher CTE to be problematic when gluing it to tungsten. Because our gluing process

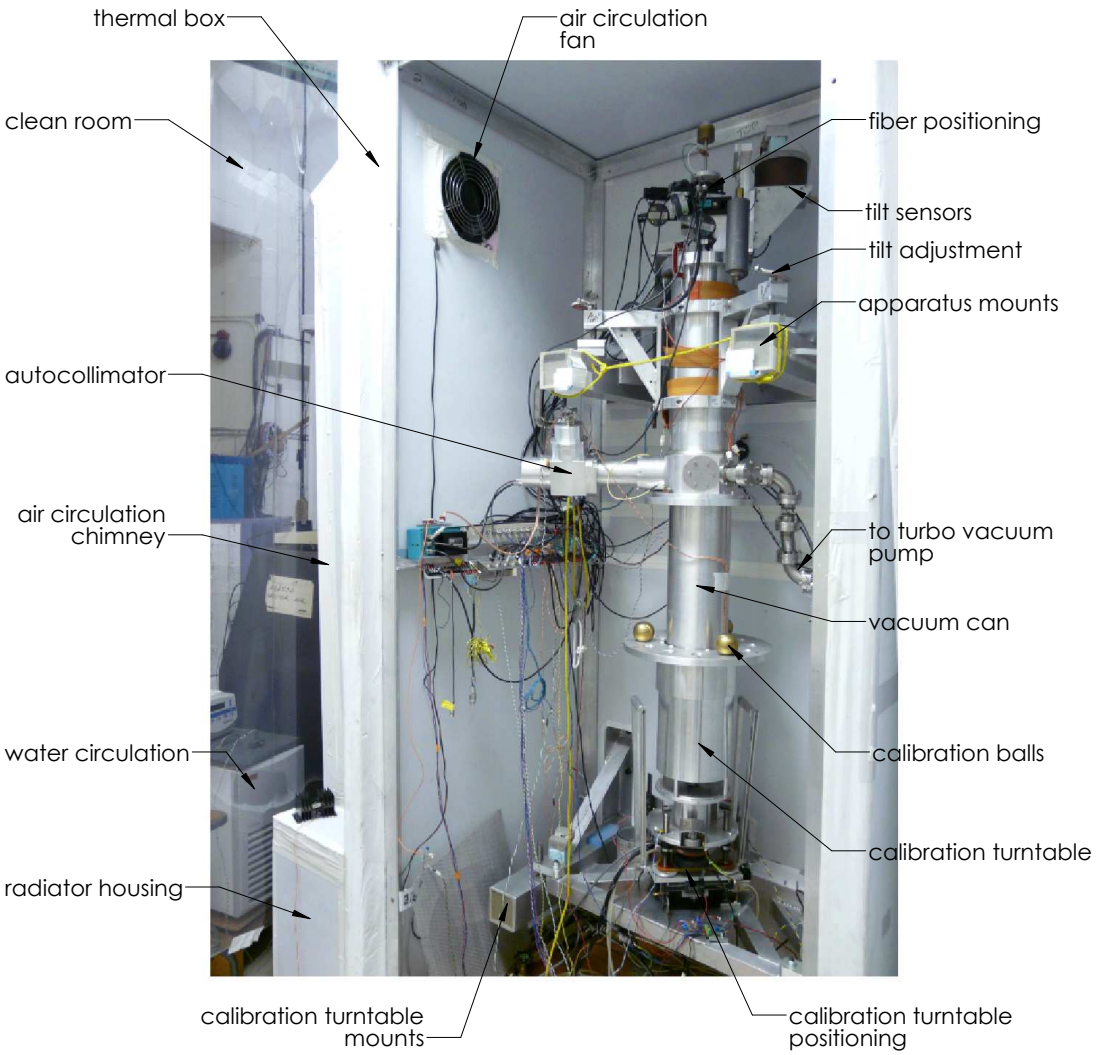

Figure 3.1: Photograph of apparatus. The pendulum hangs approximately at the height of the calibration balls from a 0.8 m long fiber attached to the fiber positioning stages (known as "phi-top"). The vacuum flange with attractor motor attaches at the bottom of the vacuum can, which is obscured in this picture by the calibration turntable.

required heating, the titanium-glue-tungsten bond created bulges in the tungsten as the pieces cooled. The Pyrex-glue-tungsten bond, on the other hand, kept the tungsten taut when cooled. A drawback of Pyrex, however, is that as an insulator it cannot be cut by the EDM. This prevented cutting the final inner and outer radii cleanly and led to the unintended consequence of an 18-fold rim-protrusion (Section 5.1.5).

Dow Integral E100 adhesive film was chosen because it provided a uniform thickness of glue, demonstrated good adhesion between tungsten and Pyrex, and bonded at a relatively low temperature compared to similar glues. We also considered various liquid two-part epoxies, but found them to be difficult to handle with unreliable adhesion. A drawback of Dow Integral E100 is that it has no known solvent, so we could not easily remove unwanted glue or separate the pieces if desired.

3.1.2 Machining

The pendulum and attractor tungsten foils were loaded in a jig and machined simultaneously. The process for cutting the slots was

1. Pre-cut foils with clocking holes for alignment in jig
2. Clean and weigh foils
3. Cut 18-fold slots
4. Clean and weigh foils
5. Cut 120-fold slots
6. Clean and weigh foils

The jig was made of two 1 mm thick molybdenum plates with the wedge patterns pre-cut a fraction of a millimeter larger than the final requirement. One jig plate had two clocking pins that ensured consistent alignment of corresponding clocking holes in the tungsten foils and other jig plate.

By using a molybdenum jig and EDM to cut the foils, the attractor and pendulum never came in contact with steel tools that could have magnetically contaminated the pieces (the clocking pins, though steel, only contacted the foils in regions that were eventually cut off).

After the foils were glued onto the Pyrex, the pieces were returned to the EDM to trim excess material from the inner and outer radii.

3.1.3 Gluing

The data sheet for Integral E100 adhesive suggests bonding with both heat and pressure. The stated activation temperature of the glue is 102° C.

We built a spring-loaded press to provide pressure while gluing (Figure 3.2). It had a removable centering pin to concentrically align the tungsten foil and the Pyrex disk. The bottom pressing surface was lapped flat and hard anodized. A 0.002" thick Teflon sheet was placed on the bottom pressing surface to avoid gluing the pieces to the press. A 1/16" thick Teflon pad was placed between the Pyrex and top pressing surface to prevent pressure points cracking the Pyrex.

We used a Cascade TEK TV0-1 vacuum oven with digital controller to precisely control the temperature and timing of bonding. We did all gluing under rough vacuum pressure ($\approx 10^{-2}$ torr) to prevent air bubbles being trapped in the glue. Our baking cycle for bonding the pieces was

1. Turned on oven with set temperature of 90° C.
2. When temperature reached 90° C, started 20 minute timer.
3. After 20 minutes, changed set temperature to 130° C.
4. When temperature reached 102° C, started 45 minute timer.
5. After 45 minutes, turned off oven.

A feature of the glue was that it did not "cure" (chemically change after heating), but could be heated and cooled multiple times. Our gluing process was

1. Bead blasted one side of the Pyrex to provide textured bonding surface.
2. Applied glue to Pyrex by assembling press with all pieces excluding the tungsten foil.
3. Baked the press in the oven.
4. After press was cool, removed Pyrex and trimmed excess glue from inner and outer radii with razor blade.

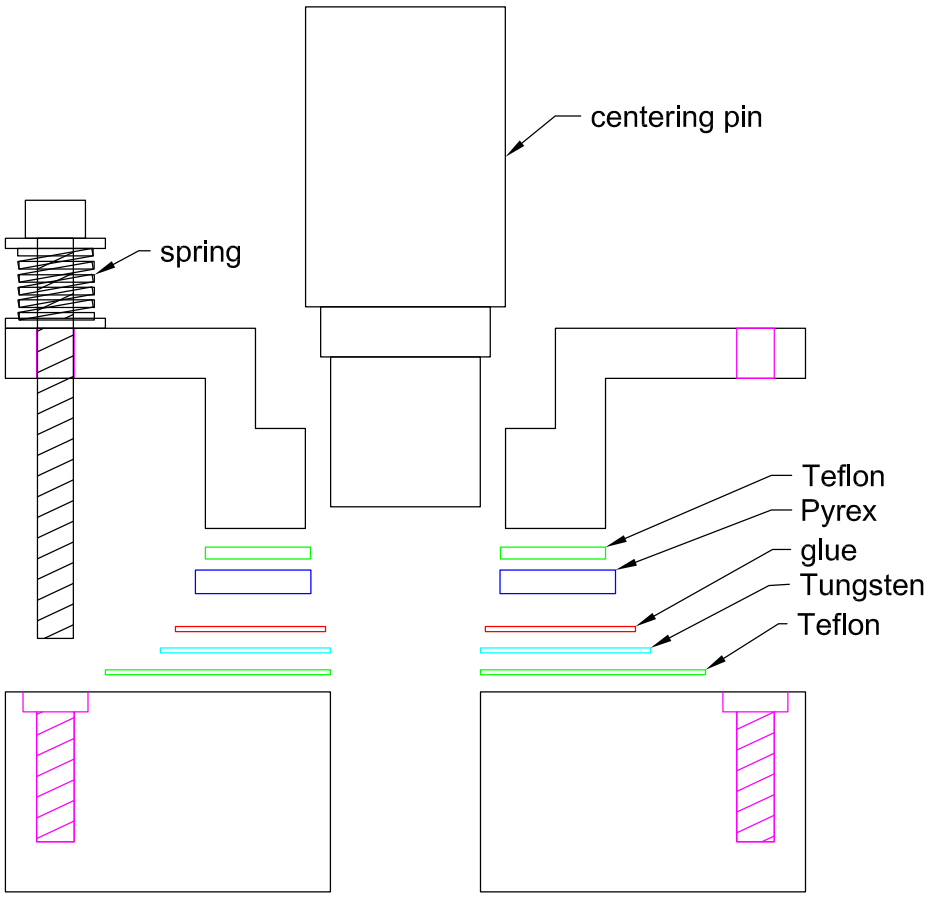

Figure 3.2: Schematic of glue press cross section. Six spring-loaded bolts applied pressure to the stack. The vertical scale of the glue, tungsten, and Teflon pieces have been exaggerated for clarity.

5. Reassembled press with all pieces including tungsten foil.
6. Baked the press again.

This process was repeated for the pendulum and attractor. Despite our efforts to ensure the repeatability of the process, we observed some differences in the outcome of the pieces. One tungsten-Pyrex pair exhibited much less cratering than the other (cratering and other glue anomalies are discussed in Section 5.1), so we chose it to be the pendulum to make pendulum-screen capacitance calculations less complicated.

3.1.4 Gold Coating

The assembled attractor and pendulum pieces were gold coated using an electron-beam evaporator. The pieces were rotated a few inches above the evaporator crucible while under high vacuum (1×10^{-6} torr). We put down adhesion layers of titanium $\approx$ 500 Å thick, and gold layers $\approx$ 1000 Å thick. This was repeated in different configurations until all sides were well coated.

3.2 Pendulum Body

The body of the pendulum consisted of a titanium post, a mirror cube, aluminum calibration balls, and a "top hat" leveling mechanism (Figure 3.3).

The post was made of titanium to be light weight and have a similar CTE as the Pyrex disk. The post and Pyrex were glued together with four small beads of conducting epoxy. The holes in the post provided pumping channels to the interior volume and were configured to partially cancel the q_{44} gravitational moment of the mirror cube.

The mirror cube, made by Red Optronics in Mountain View, CA, was 0.5" per side with a 0.25" bore hole through the vertical center. It was made of BK7 glass, which has a CTE closely matched to titanium. Each gold coated face of the mirror was electrically connected to the titanium post with a small bead of conducting epoxy.

The 0.25" diameter aluminum calibration balls sat on an aluminum tray. The tray had six positioning holes, instead of just the required three, so it would not gravitationally contribute to the calibration torque (calibration is discussed in Section 6.4). The tray was

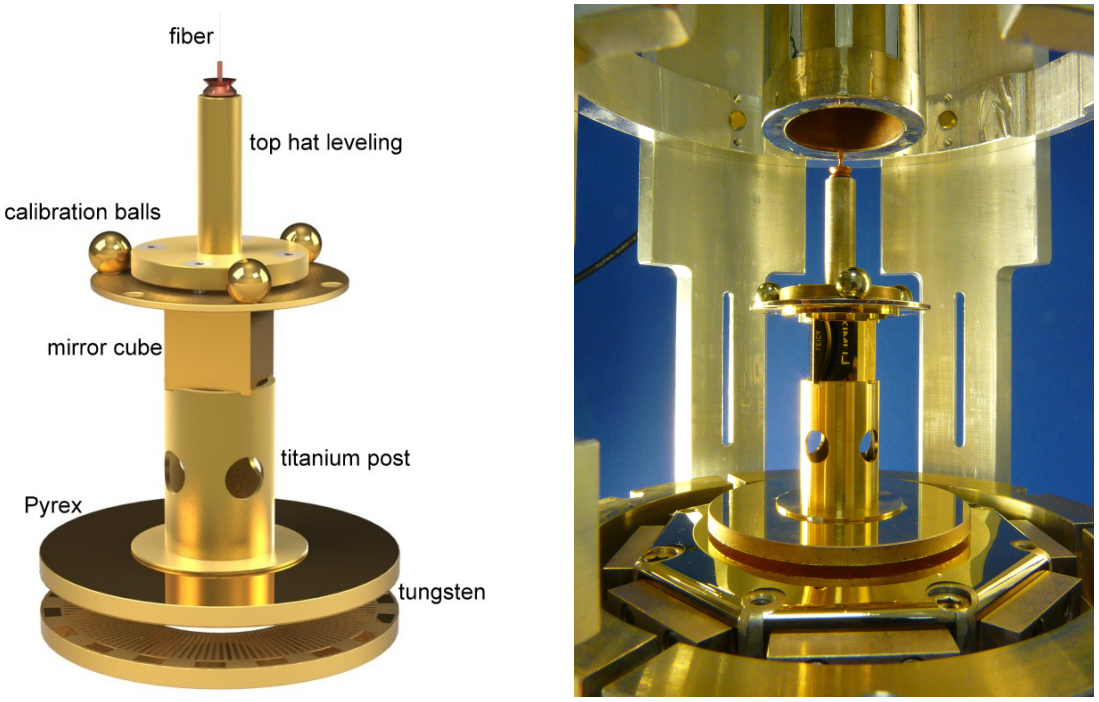

Figure 3.3: LEFT: Render of pendulum and attractor. RIGHT: Photograph of the pendulum above the drumhead electrostatic screen.

fastened to the titanium post via a threaded titanium extension passing through the bore hole of the mirror cube and a brass securing nut.

The "top hat" leveling mechanism consisted of an aluminum post that received the fiber screw, a beryllium-copper wave washer, and four titanium machine screws. The wave washer allowed arbitrary adjustment of the screws which translated the fiber connection point relative to the center of mass of the pendulum, causing a change in the overall tilt. We used this adjustment to ensure the bottom of the pendulum was perpendicular to the twist axis of the fiber (Section 6.1.4). Similar to the holes in the titanium post, the four titanium machine screws were configured to partially cancel the q_{44} gravitational moment of the mirror cube.

3.3 Drumhead Electrostatic Screen

We designed the electrostatic screen to provide a direct line of sight to the bottom of the pendulum, which made dust detection and removal far easier (Section 6.2). The screen is visible below the pendulum in Figure 3.3.

The 0.0005" thick beryllium-copper screen was mounted on an octagonal aluminum rim and stretched over an aluminum drum with four tensioning bolts. The aluminum drum had clearance for the attractor to turn inside it. The screen could be removed and replaced without changing the position adjustment of the drum, which was useful when aligning the attractor and screen.

3.4 Bearing Assembly

The bearing assembly provided smooth rotation of the attractor, precise angle information via an optical encoder, kinematic adjustment of the attractor alignment, and isolated electrical contact to the attractor for capacitance measurements. Figure 3.4 shows a schematic of the bearing assembly.

The rotating elements of the attractor were all built from non-magnetic materials. The clutch nut, shaft, encoder scale hub, flywheel, and cup were all made of pure grade 2 titanium. The slip ring electrical contact was copper, the encoder scale was glass, the

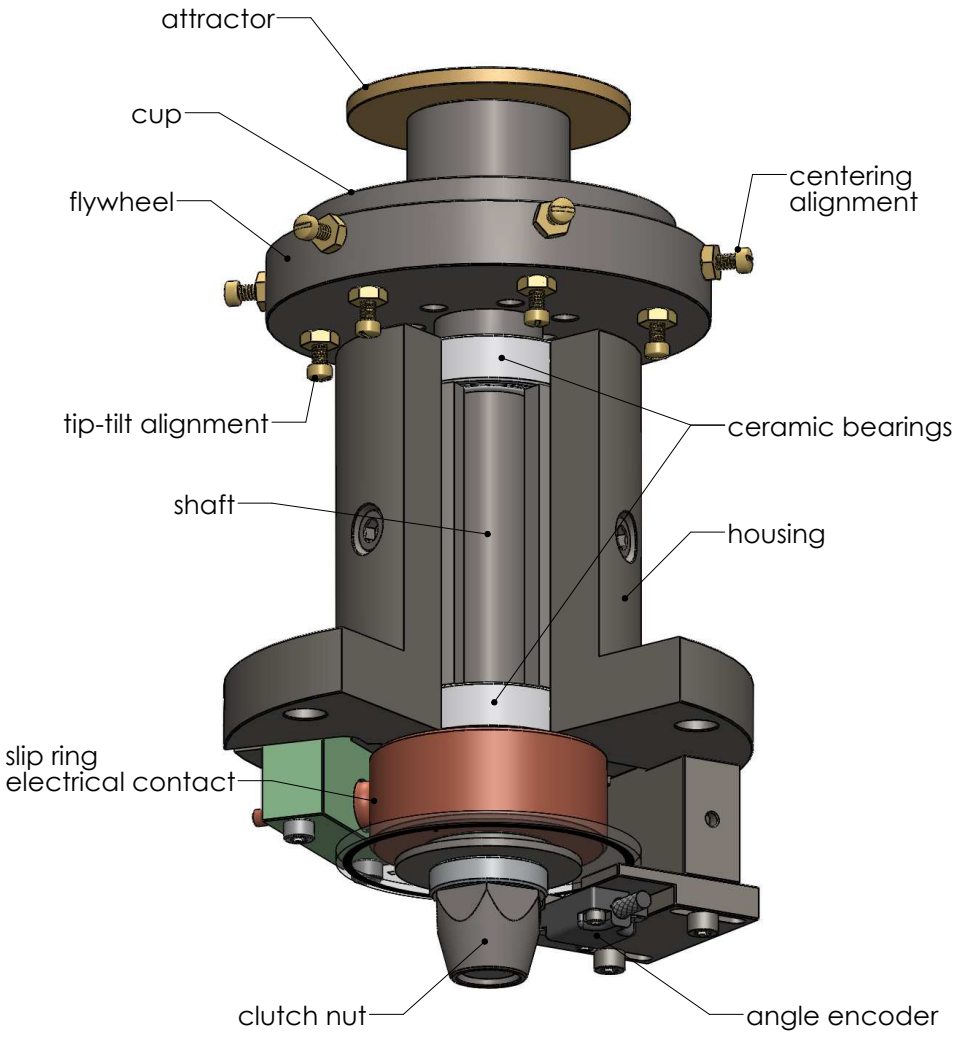

Figure 3.4: Schematic of bearing assembly. A section of the housing has been removed for illustrative purposes.

bearing balls and races were zirconium dioxide (ZrO_2) ceramic, the adjustment screws were silicon bronze 655, and the adjustment springs were beryllium-copper.

The angle encoder was a MicroE Systems Mercury 3000V high vacuum rotary encoder that provided 2^{21} pulses per revolution, plus a once-per-revolution index pulse. The encoder scale was marked on a glass disk and mounted on the rotating shaft. The scale was optically tracked by a stationary read-head mounted a few millimeters below.

The kinematic attractor mount, that provided centering and tip-tilt adjustment of the cup and attractor, is discussed in Section 6.1.2.

The slip ring electrical contact had a spring loaded copper pin with polished head riding on a rotating polished copper bushing. A lubricant of Apiezon AP100 vacuum grease doped with graphite lessened the friction and improved the contact fidelity. It enabled measurement of the attractor-screen capacitance while the attractor was turning.

3.5 Attractor Rotation

The attractor was turned by a 480000 steps-per-revolution geared stepper motor located outside the vacuum. The stepping pulses were dictated by a control loop that synchronized angle encoder readings from the bearing assembly with clock pulses from a function generator. This method of stepping achieved angle error 100× smaller than stepping the motor directly with clock pulses (Figure 3.5).

The stepper motor was mounted on a 6" vacuum flange and coupled to a ferrofluidic rotary feedthrough that provided nearly frictionless rotation (Figure 3.6). A coupling bellows was secured to the vacuum side drive shaft and engaged the clutch nut on the bearing assembly with a tapered collet when the flange was in place.

We kept the stepper motor at a constant temperature using a water-cooled peltier device. The motor settled at a temperature several degrees above ambient while the motor was running, but our data protocol required taking data with the motor off a couple hours each day (Section 6.3.1), so the peltier prevented temperature fluctuations of the apparatus.

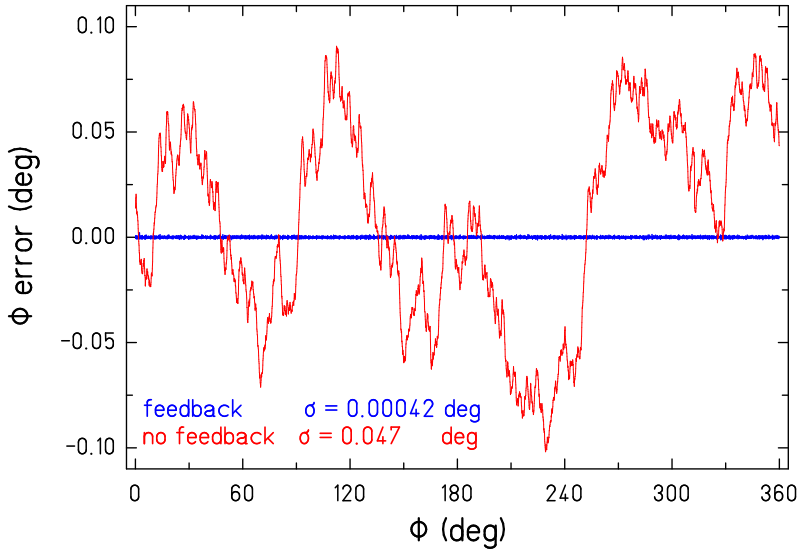

Figure 3.5: Attractor rotation angle error when driven directly by clock pulses (no feedback), and when pulses were in feedback to readings from the angle encoder.

3.6 Calibration Turn Table

The calibration turntable rotated three brass balls outside the vacuum vessel to provide a known gravitational torque on three smaller balls on the pendulum. The turntable could be translated in xyz to match movements of the pendulum, maintaining a constant relative position between the calibration balls.

We mounted the turntable to the cyclotron magnet with supports similar to those supporting the vacuum vessel. This decoupled the turntable from the floor of the thermal box, which was not designed to be mechanically stable. (These supports required moving the air circulation system – a fan and radiator that thermally coupled the air to the circulating water system – outside the main thermal box volume.)

We also motorized the turntable's xyz-positioning to eliminate opening of the thermal box each time we moved the pendulum. A Danaher Motion XYR-6060 table with 4" $\times$ 4" of travel provided xy-translation of the turntable. Three chain-and-sprocket driven lead screws provided z-translation of the turntable. All axes were stepper motor driven and

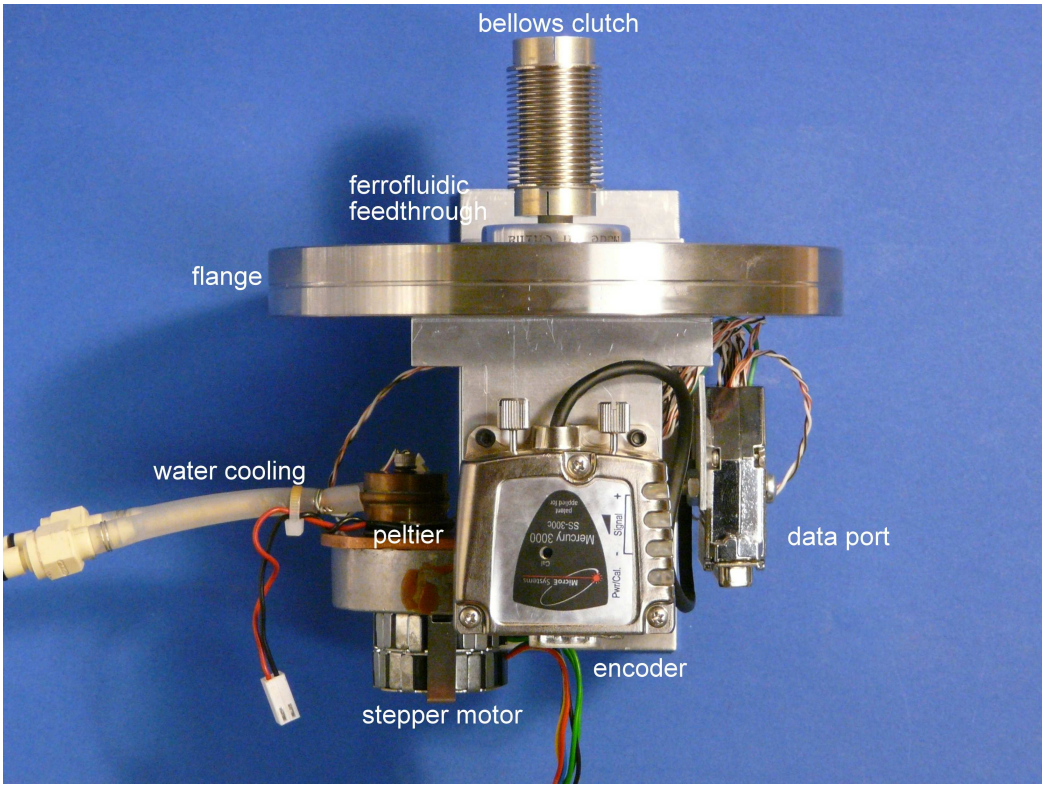

Figure 3.6: Attractor drive vacuum flange. The flange mounted at the bottom of the vacuum can, directly below the bearing assembly. The data port provided connections to multiple in-vaccumm temperature sensors and to the attractor and screen for capacitance measurements.

position changes were monitored at 0.01 mm precision with Mitutoyo linear scales.

Cabling to run the attractor systems (encoder, peltier, water cooling, temperature sensors) all passed through the center of the turntable's bearing when the turntable was in place. As discussed in Section 6.4, this introduced problems as the space was very confined and the turntable was removed for the majority of short-range data taking.

Chapter 4

PENDULUM AND ATTRACTOR CHARACTERIZATION

The following sections detail our measurements of the key physical parameters describing the pendulum and attractor. The use of these measurements to build accurate models is discussed in Chapter 5.

4.1 Thickness

The thicknesses of the tungsten foils were determined prior to making any cuts in the material. The foils were cleaned, then a grid was drawn with non-permanent marker in the center regions of the 10cm $\times$ 10cm foils. Thickness measurements were taken in each grid square using a Mitutoyo sheet metal micrometer (model 389-711-30) that had a digital readout to 1 μm. Figure 4.1 shows the thickness measurements for each foil. After the measurement, the grid markings were washed off.

Average thickness measurements of 54.5 ± 1.1 μm and 54.4 ± 0.8 μm were found for the pendulum and attractor, respectively.

4.2 Total Removed Mass

The foils were weighed three times before gluing them to the Pyrex disks: 1) after clocking holes had been cut but before any slots were removed, 2) after the 18-fold slots were removed, and 3) after the 120-fold slots were removed. All measurements were taken with a Sartorius LA310S balance with digital readout to 0.1 milligrams.

For each weighing, the foils were repeatedly cleaned until all measurable amounts of dirt were removed and the measurement stabilized to within the readout of the scale. Our typical cleaning procedure was to soak the foils in an ultrasonic bath with a detergent (20% solution of potassium hydroxide or MERI-SUDS) or solvent (acetone) for 30 minutes, followed by a rinse with de-ionized water.

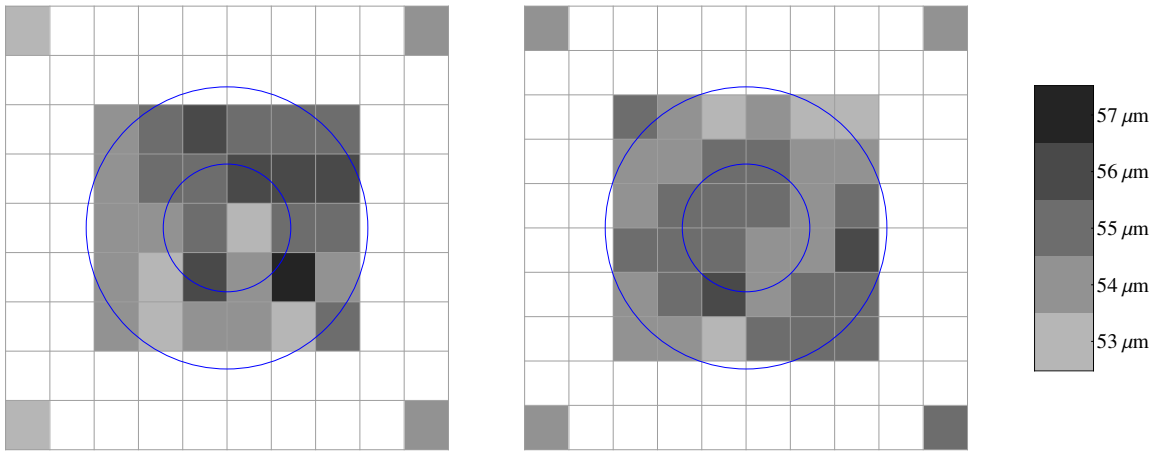

Figure 4.1: (dimensions not to scale) Thickness measurements of the pendulum foil (left) and attractor foil (right). The corner measurements were not used to determine the average thicknesses as the center is the area out of which the final foils were cut.

These measurements were complicated, however, by unintentional corrosion of exposed areas that occurred during the EDM'ing of the slots. The corrosion was likely due to either the deionized cooling water directly attacking the tungsten, or, if the cooling water had acquired electrolytes, galvanic corrosion of the tungsten which was in direct electrical contact with the more noble molybdenum jig.

The areas exhibiting corrosion were the 120-fold slot regions of both foils and two small circles on the pendulum foil where an extra set of clocking holes had been removed from the jig. The corrosion in the 120-fold regions made the 2^{nd} weighing an unreliable determiner of the 18-fold removed masses, but would not effect the reliability of the 3^{rd} weighing for determining the total removed masses. The corrosion in the clocking circles, however, would have an effect on the 3^{rd} weighing of the pendulum foil that would require correction.

After our 2^{nd} weighing, the foils were placed in the jig and allowed to sit in the cooling water stream over night ($\approx$16hrs), then the foils were weighed again. The pendulum foil lost an additional 0.0057 grams and the attractor foil lost 0.0050 grams. Using the 120-fold area of 565.5 mm^2 and the clocking circles area of 98.8 mm^2, we determined the pendulum foil corrosion rate was 5.4×10^{-7} g/hr/mm^2, with the attractor foil in good agreement at

5.5×10^{-7} g/hr/mm^2. We estimate the foils spent a total of 24 hrs in the EDM, so the mass of all slots removed from the pendulum foil was corrected by 0.0015 g to account for the clocking circle corrosion. Table 4.1 summarizes the mass measurements.

Although we did not observe significant corrosion on the attractor foil outside the 120-fold area, there may have yet been corrosion not accounted for, so we placed an uncertainty on our measurement of 0.0005 g. We estimate the uncertainty in our corrosion calculation for the pendulum foil to be as large as 50%, so we have conservatively chosen an uncertainty of 0.001 g for that measurement.

Table 4.1: Mass of foils at each stage of manufacture. The total removed slot mass of the pendulum foil has been corrected down by 0.0015 g to account for observed corrosion elsewhere on the foil. All units are in grams.

	weighing	pendulum foil	attractor foil
1st	clocking holes cut	3.4372	3.7551
2nd	18-fold slots cut	3.2356	3.5541
	corrosion test	3.2299	3.5491
3rd	120-fold slots cut	2.6531	2.9704
mass of removed slots		0.7826 ± 0.001	0.7847 ± 0.0005

4.3 Slot Dimensions

We inspected the tungsten foils with an OGP SmartScope to verify slot dimensions before gluing them to the Pyrex substrates. The SmartScope provided precise xy-data along all edges of the slot patterns.

As a check against systematic bias in the SmartScope, we repeated our inspections with the foils flipped over and rotated by 90°. The flip with rotation resulted in an equivalent layout of the wedge pattern, which meant we did not have to reprogram the inspection routines. This check revealed no significant artifacts inherent in the SmartScope. The plots in the following sections show four sets of data corresponding to the two inspections of the two foils.

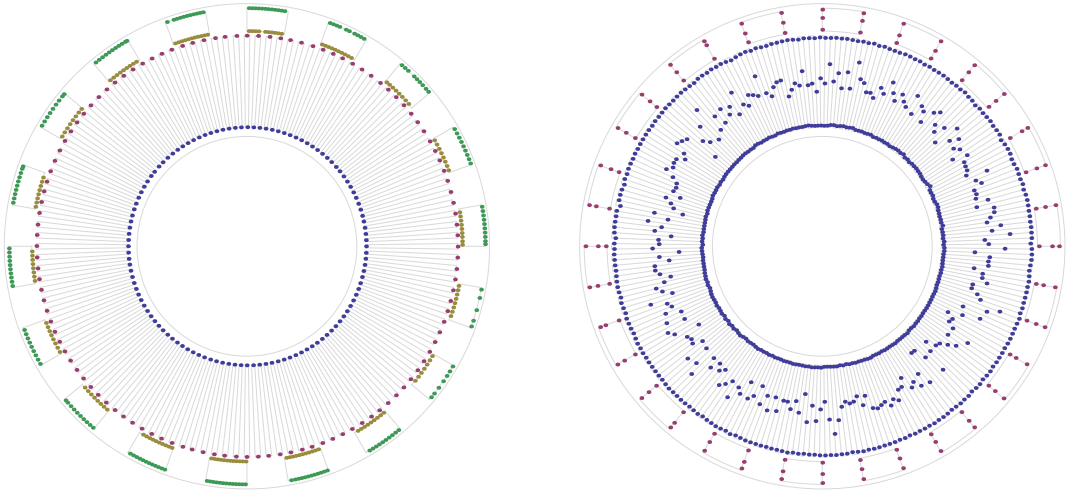

Figure 4.2: SmartScope data used for slot dimensions (1 of 4 inspections shown). Radius data (left) determined concentricity and radii values. Spoke data (right) determined subtended angles. Slot outlines are included as a visual aid.

We estimate the effect on the torque signals of some of the resolved manufacturing defects in the following sections. The effects are compared to the cumulative statistical sensitivity of the experiment, which is calculated to have a lower limit of $0.01/\sqrt{60} \approx 1\times10^{-3}$, where 0.01 is the smallest noise-to-signal ratio per day encountered in the W3 data set and 60 is roughly the number of days we took data.

4.3.1 Concentricities

The slot patterns were designed to be perfectly concentric. We checked the actual concentricity by analyzing xy-data of edges along the four slot radii (Figure 4.2).

Circles were fit to each set of radii data with the radius and xy-center as free parameters. The xy-center fits (Figure 4.3) show that the 120-fold radii were non-concentric by 0.36 ± 0.25 μm, the 18-fold radii were non-concentric by 0.9 ± 0.1 μm, and on average the 18-fold slots and 120-fold slots were non-concentric by 7.9 ± 0.2 μm.

Non-concentricity implies that the slot patterns don't remain aligned as the attractor rotates. This effects the torque amplitudes similar to an attractor centering misalignment (Equation 6.4). Adding these effects to the measured attractor runout (Section 6.1.2) of

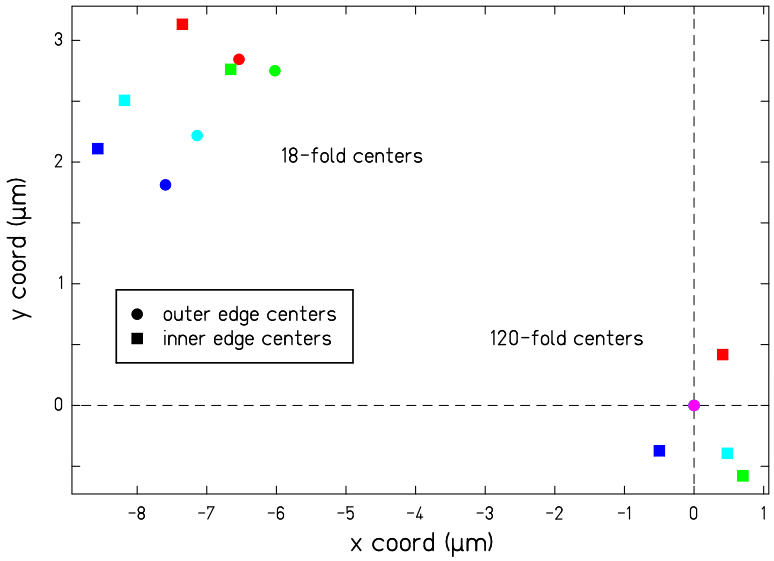

Figure 4.3: xy-centers of all slot radii. 120-fold centers are grouped at the bottom right corner, with the outer radius defined as the origin. 18-fold centers are grouped in the top left corner. Flipped-rotated data have been corrected.

$r_a = 10$ μm, and assuming a centered pendulum, gives a relative torque correction of $1{\times}10^{-4}$ for the 120ω and $7{\times}10^{-5}$ for the 18ω. These are roughly ten times smaller than the cumulative statistical sensitivity of the experiment.

4.3.2 Radii

Figure 4.4 shows the radius data of all inspections as a function polar angle, and Table 4.2 lists the best-fit radii and their statistical uncertainty.

The slot patterns were designed with all slots of a given symmetry having the exact same inner and out radius. As seen in all panels of Figure 4.4, there is resolved structure in the radius measurements as a function of polar angle. The structure is on the order of 15 μm peak-to-peak for the 120-fold slots, and 5 μm peak-to-peak for the 18-fold. The structures appear similar in amplitude and phase between inner and outer radii, indicating that the length of the slots is well preserved while the placement of them with respect to the center is meandering.

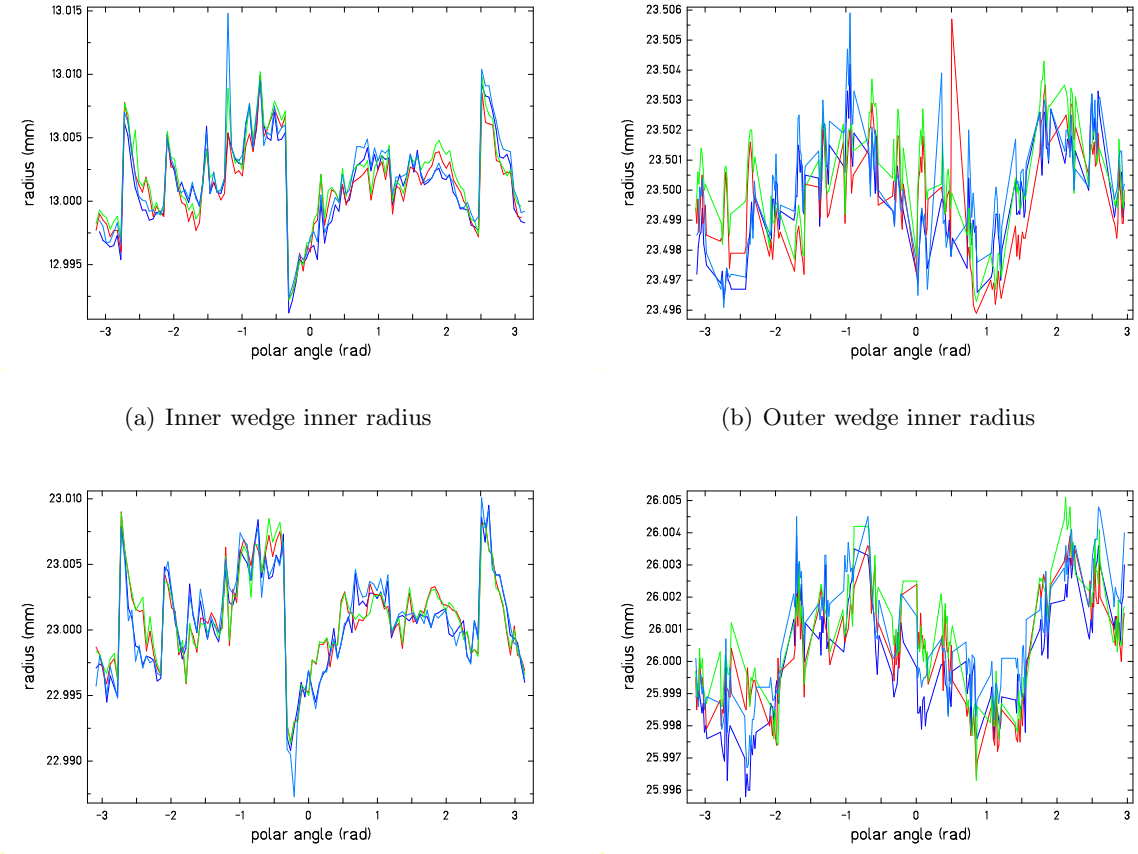

(a) Inner wedge inner radius

(b) Outer wedge inner radius

(c) Inner wedge outer radius

(d) Outer wedge outer radius

Figure 4.4: Radii measurements as a function of polar angle. Data have been corrected for flipped-rotated inspections.

The result of these slot placement defects, similar to the concentricity defects, is pattern misalignment as the attractor turns, which affects the torques similar to an attractor centering misalignment. Adding 7.5 μm and 2.5 μm to $r_a = 10$ μm, with $r_p = 0$, in Equation 6.4, gives a relative effect of $2{\times}10^{-3}$ for the 120ω and $2{\times}10^{-5}$ for the 18ω. The effect on the 120ω may be near the cumulative statistical sensitivity of the experiment, but can be accommodated by the multiplicative systematic factor in the fit to data (Section 7.2.8).

Table 4.2: Average slot radii. Units are in mm.

radius	design	measured
120 IR	13	13.0016 ± 0.0002
120 OR	23	23.0008 ± 0.0002
18 IR	23.5	23.5000 ± 0.0001
18 OR	26	26.0004 ± 0.0001

4.3.3 Subtended Angles

The slot patterns were designed to have all slots subtend an angle exactly half of the repeated symmetry angle. We collected three points along each radial edge (spoke) of the slots to check these angles (Figure 4.2).

We subtracted the average of the two 120-fold best-fit xy-centers from all 120-fold spoke data for each inspection, and similarly for the 18-fold data. Then we fit each spoke with a line that passed through the origin. The polar angle for each spoke was determined as the arctangent of the best-fit slope. The subtended angle of a slot was the difference in polar angle of that slot's spokes. Figure 4.5 shows the subtended angles of the slots for the 18-fold and 120-fold slots as a function of the polar angle.

The average subtended angle of the 120-fold slots was 1.5001 ± 0.0004 deg, with an RMS deviation from nominal of 0.008 deg. The average subtended angle of the 18-fold slots was 9.9983 ± 0.0009 deg, with an RMS deviation from nominal of 0.007 deg.

As derived in Section 2.1, the torque is proportional to $\sin^2(m\beta)$, where $\beta = \pi/(2m)$ rad is the nominally designed subtended half-angle. Because this is an even function for deviations from nominal, it is the RMS deviation from nominal (not the average values, which are essentially nominal) that is pertinent to the torque. This gives a $3{\times}10^{-4}$ relative correction for the 120ω torque, and a $5{\times}10^{-6}$ relative correction for the 18ω torque. Both are well below the cumulative statistical sensitivity of the experiment.

4.4 Surface Roughness

The EDM did not make perfectly smooth cuts through the tungsten, but left a rough surface with peaks and valleys. The SmartScope finds the edges as defined by the peaks but cannot see the valleys, therefore the edge measurements did not measure the true (gravitationally defined) edges of the slots. We analyzed a sample of tungsten foil with an atomic-force microscope (Veeco Dimension 3100 AFM at the Nanotechnology User Facility on campus), measuring RMS surface variations of 0.25 μm for the EDM'd surface and 0.015 μm for the broad surface (Figure 4.6). These values compare to 2.2 μm and 1.2 μm RMS for the molybdenum pieces used in [6].

We should note that there was visible roll chatter on the broad surface of the tungsten foils, but we were unsuccessful in measuring the structure of this chatter. The SmartScope had inadequate resolution to resolve the structure and the AFM had too small a scan area. It is possible our thickness measurements were overestimated due to the roll chatter by roughly two times the SmartScope laser probe resolution of ≈ 0.5 μm.

4.5 Glue Density

The data sheet for Dow Integral E100 adhesive claims a yield of 42.6 $m^2/kg/25\mu m$, which translates to a density of 0.939 g/cm^3. This number is presumed to indicate the density of the pre-bonded glue, however the density may change after bonding due to mass loss of volatiles during heating. The final density of the bonded glue is of interest.

We cut a small square of the glue (approximately 2cm x 2cm) that weighed 0.0178 ± 0.0001 g. This square was glued to a flat piece of glass using the same press and baking routine used to assemble the pendulum and attractor (Section 3.1.3).

The volume of the bonded glue was measured with the SmartScope. The glue had an average thickness of 0.003666 ± 0.000001 cm, as measured with the laser sensor collecting data on a 0.2 mm grid. The glue had an area of 5.179 ± 0.002 cm^2, as measured with optically collected perimeter data at 10 μm spacing, and assuming an xy-uncertainty of 1 μm for each point.

These values give an un-bonded density of 0.939 ± 0.005 g/cm^3, confirming nicely the

value provided in the data sheet. Weighing the glass with bonded glue gave a mass 0.0006 ± 0.0001 g less than the sum of the un-bonded glue and glass masses, resulting in a bonded glue density of 0.935 ± 0.007 g/cm^3.

4.6 Final IR and OR

We measured the contours of the final inner and outer radii using the SmartScope, after the foils were glued to the Pyrex substrates and the excess tungsten foil was removed with the EDM. The best-fit radii values (Table 4.3) were important for determining the overall area used in the capacitance models.

The contours of the outer radii revealed 18-fold structure (Figure 4.7) that was significant to the gravitational modeling and is discussed in detail in Chapter 5.

Table 4.3: Final foil radii of the pendulum and attractor. Units are in mm.

radius	measured		
pendulum IR	12.0963	$\pm$	0.0001
pendulum OR	26.6024	$\pm$	0.0005
attractor IR	12.1232	$\pm$	0.0007
attractor OR	26.6237	$\pm$	0.0008

4.7 Surface Contours

We collected detailed surface-height maps of the final pendulum and attractor pieces using the laser attachment of the SmartScope (Figure 4.7). These scans were taken with the pendulum mounted to the pendulum body and the attractor mounted on the bearing cup so that any influence to the macroscopic shapes due of the mounting would be accounted for in the maps. These maps largely dictated the gravitational and capacitance models and are fully discussed in Chapter 5.

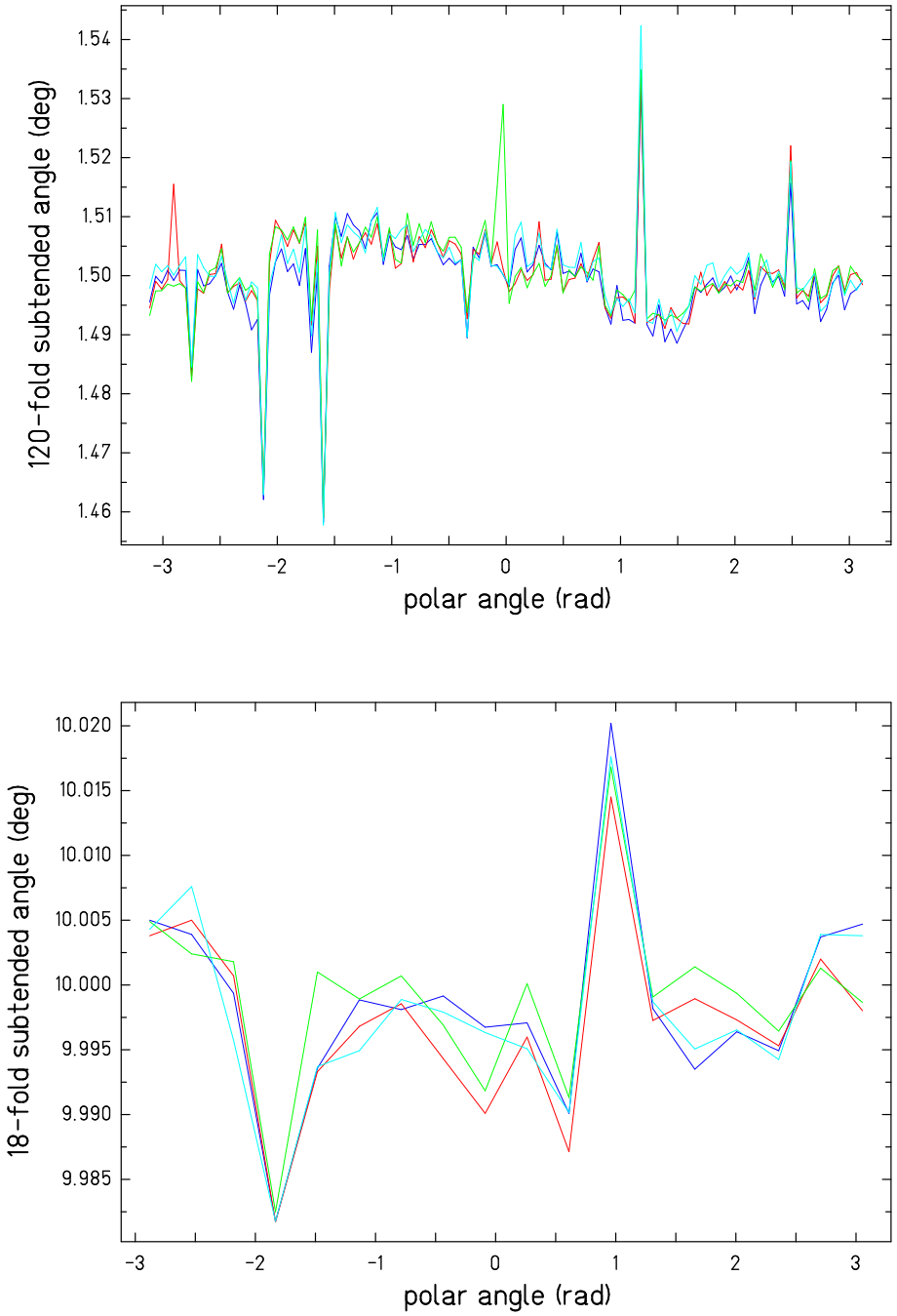

Figure 4.5: The subtended angle of slots as a function of polar angle. Data have been corrected for flipped-rotated inspections.

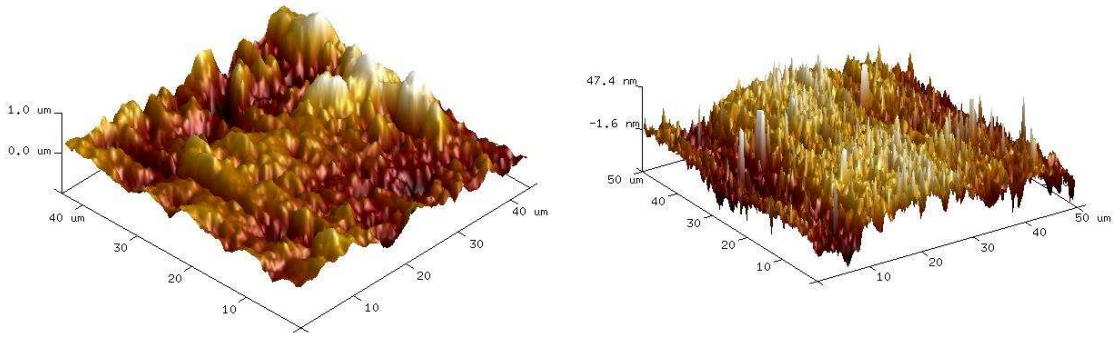

Figure 4.6: Surface roughness of a tungsten foil sample as measured with an AFM. LEFT: measurement of EDM'd surface. Scan area covers nearly the full thickness of the foil. The scan indicates RMS variation of 0.25 μm. RIGHT: measurement of the broad surface of the foil. The scan indicates RMS variation of 0.015 μm.

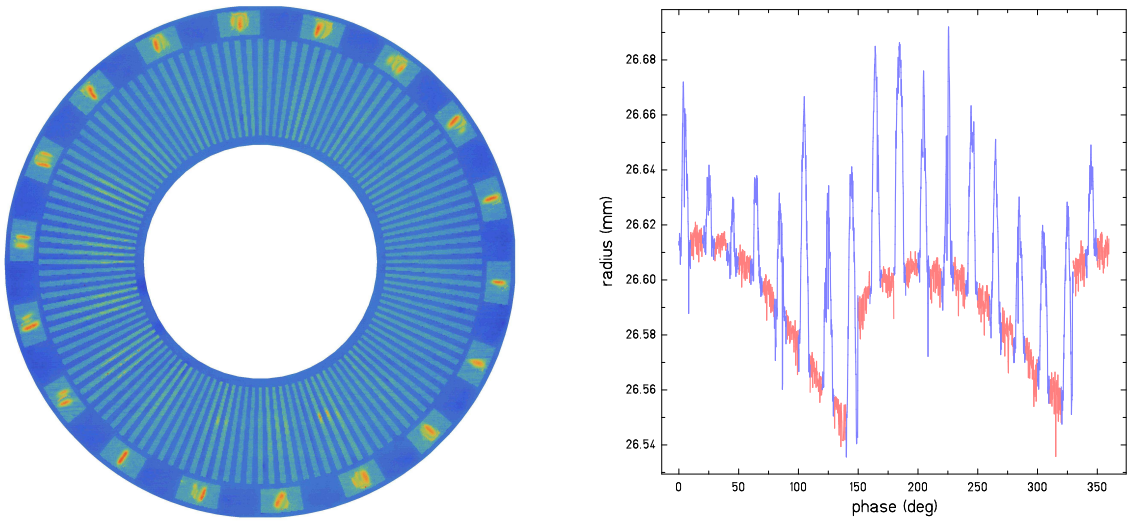

Figure 4.7: SmartScope data of the pendulum. LEFT: Laser scan of tungsten-glue surface. Lighter colors are farther from the laser sensor. Laser data was collected on a 0.1×0.1 mm grid, and $\sim$175000 points are represented. RIGHT: Optical scan of outside rim. Blue data are aligned with 18-fold tungsten and red data aligned with 18-fold slots. The roughly 2-fold oscillation of the data was caused by trimming half the outer rim with the EDM, re-clamping the piece, then completing the trim.

Chapter 5

GRAVITY AND CAPACITANCE MODELS

Detailed geometrical models of the attractor and pendulum were needed to interpret our twist data. A mass-distribution model (gravity model) was needed to calculate the Newtonian and Yukawa torques. A surface-geometry model (capacitance model) was needed to translate capacitance measurements into separation values z_p and z_a.

Both models were based on data collected with the Optical Gaging Products SmartScope Zip Lite 250 measuring microscope with DRS-500 laser sensor. The laser sensor provided detailed, non-contact surface maps of the pieces, and the optical microscope provided precise edge-location data.

The SmartScope data revealed a number of anomalies which arose from gluing the tungsten foils to the Pyrex substrates. The gluing process required heating the parts above 102° C, the temperature at which the adhesive film was activated, and this led to the following unintended consequences,

Dishing: Both the pendulum and attractor were dished such that the 18-fold patterns were closer to each other than the 120-fold patterns. This dishing was a result of the different thermal expansions of the tungsten and Pyrex (4.5 and 3.3 μm/(m K)) and the resulting stress in the glued pieces after they cooled.

Glue-fill: Heated glue flowed into the slots of removed tungsten, partially filling them.

Craters: The glue did not fill to an even height in all locations, leaving craters in the middle of all 18-fold slots and most of the 120-fold slots on the attractor.

Rim-protrusion: Glue pressed out from beneath the 18-fold tungsten (but not from the 18-fold slots) when the foils were glued to the glass substrates. This glue interfered with the EDM machine as it cut the final outer radius and produced parasitic 18-fold

mass distributions of both tungsten and glue on the outer rims. No similar protrusions at 120-fold symmetry were observed on the inner rims.

Figure 4.7 shows an example of the data collected with the SmartScope and clearly illustrates the crater and rim anomalies.

In the following sections we discuss the details of how we built our gravity and capacitance models from the SmartScope data, and how those models were used to inform our analysis of twist data.

5.1 Gravity model geometry

Our gravitational models were constructed of annular sectors (wedges) which could be used in the Fourier-Bessel calculation (Section 2.1). Thanks to the symmetric design, we needed to model only a single "unit cell" which was repeated 18 or 120 times. We used wedges of varying size, location, and density to approximate the average mass distributions indicated by the SmartScope data. Figure 5.1 illustrates how the 18-fold and 120-fold gravity models were built from a collection of wedges. Figure 5.2 illustrates the relationship of the pendulum models to the attractor models as well as to the copper electrostatic screen.

Each individual wedge was described by z-height (defined as distance from wedge bottom surface to z_p for the pendulum, and wedge top surface to z_a for the attractor), inner radius ir, outer radius or, subtended angle β, positional angle ϕ_0, thickness t, and density ρ.

We began with the nominal models, then made adjustments and additions to accommodate the glue-anomalies.

5.1.1 Nominal geometries

The pendulum and attractor were designed to be identical, with co-planar patterns of 18-fold and 120-fold slots of empty vacuum.

The basis for the nominal 18-fold pattern, repeated every 20°, was a single wedge of tungsten with $ir = 23.5$ mm, $or = 26$ mm, $\beta = 10°$, and $t = 54.5$ μm.

The basis for the nominal 120-fold pattern, repeated every 3°, was a single wedge of tungsten with $ir = 13$ mm, $or = 23$ mm, $\beta = 1.5°$, and $t = 54.5$ μm.

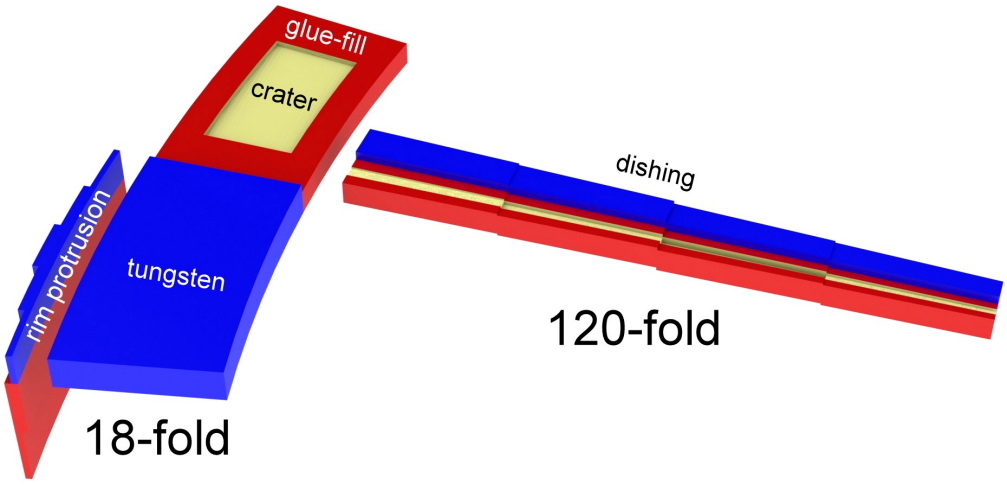

Figure 5.1: 3D diagram of the attractor gravitational models. This diagram illustrates how the dishing, glue-fill, craters, and rim-protrusion anomalies were modeled with wedges. The pendulum model has a few minor differences, most notably the absence of craters in the 120-fold glue-fill. The z-dimension, radial size of the rim-protrusion, and amount of dishing have been exaggerated.

5.1.2 Dishing anomaly

To account for dishing, we divided the 120-fold basis wedge of the pendulum (attractor) radially into 5 (4) equally spaced wedges that had varying z-heights relative to z_p (z_a). The 18-fold basis remained a single wedge with the bottom (top) surface set to $z = 0$, creating the reference surface by which we define z_p (z_a) for the pendulum (attractor). The amount of dishing is seen in Figure 5.3, which shows surface data vs. radius with gravity models overlaid.

The amount of pendulum dishing in set W1 was significantly greater than in later sets, as we were able to reduce the dishing before taking the W2 data. We took advantage of the thermal expansion of titanium (8.6 μm/(m K)) to partially reverse the dishing by gluing the Pyrex-tungsten assembly to the titanium pendulum body at an elevated temperature ($\sim$40° C). After cooling, the titanium provided a tension on the Pyrex that cancelled (at least partially) the tension from the tungsten.

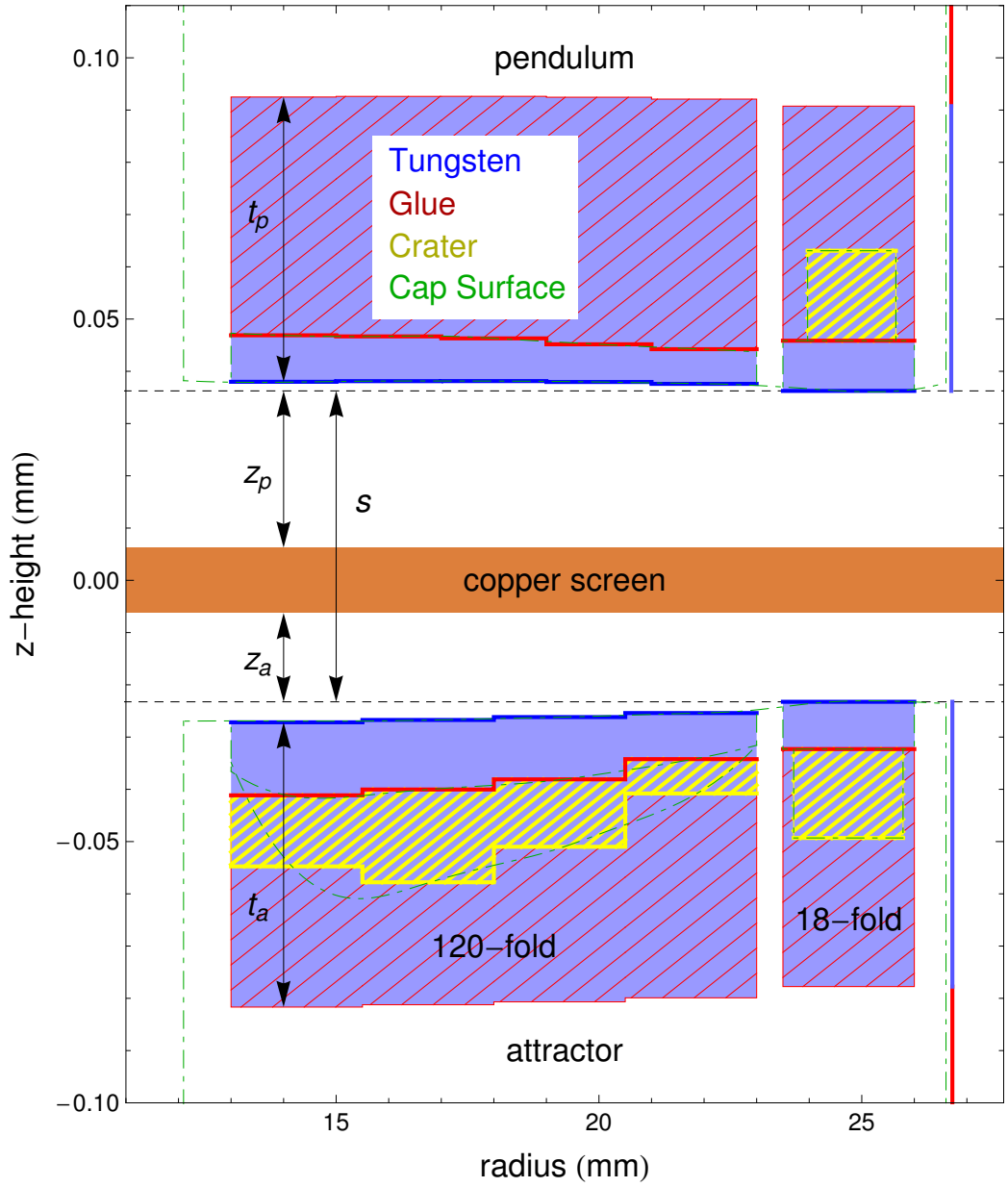

Figure 5.2: Cross-sections of the gravity and capacitance models. Slicing the gravity model through all tungsten reveals the blue surface in the 18 and 120-fold regions, as well as the blue and red rim-protrusion on the outer radii (the red lines extend beyond the plot region). Slicing the gravity model through the slots reveals surfaces of glue shown with red hatching and regions of craters shown with yellow hatching. The surfaces of the capacitance model are indicated by green, dash-dotted curves that similarly correspond to tungsten, glue, and crater regions. Additional surfaces of the capacitance model are beyond the plot region.

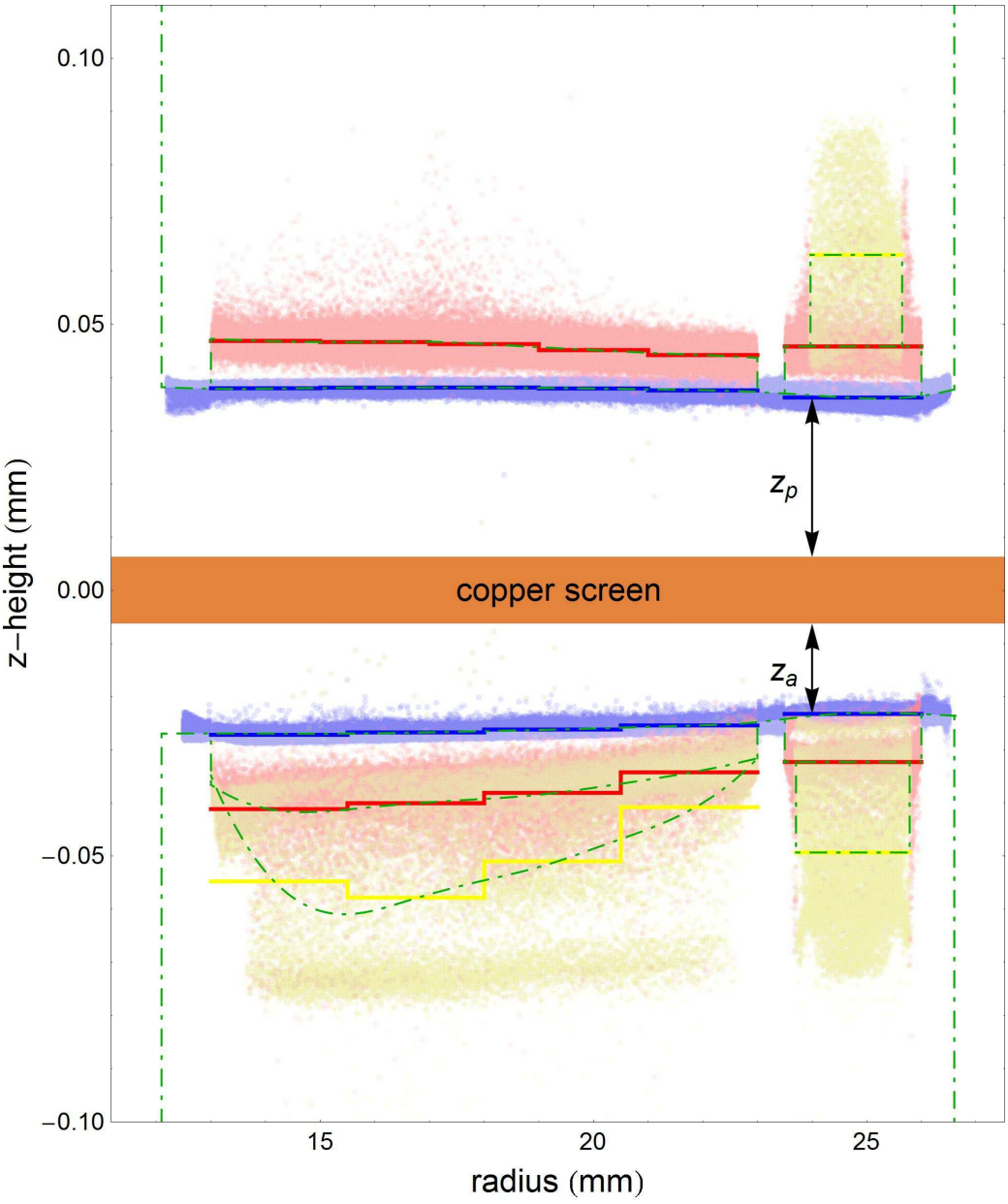

Figure 5.3: All laser scan data for the pendulum and attractor are plotted vs. radius. The blue data represent the surface height of tungsten, red data the surface height of glue in the non-crater regions, and yellow data the surface height of the crater regions. The gravity model surfaces are indicated with blue, red, and yellow solid lines. The capacitance model surfaces are indicated with green dash-dotted lines.

There remains uncertainty, however, as to how constant the dishing was. It is unknown if the dishing changed significantly under vacuum (though we don't have reason to suspect it did), and it is feasible the stresses in the glue relaxed over time, allowing the dishing to lessen. We were unable to collect reliable surface data before *and* after a data set to check this stability.

5.1.3 Glue-fill anomaly

Glue-fill was modeled with positive-density glue (p-glue) wedges added in the slot regions. The p-glue wedges had $\beta = 10^\circ$ (1.5°) and were offset in ϕ_0 by 10° (1.5°) from the tungsten wedges of the 18-fold (120-fold) models. The 120-fold p-glue wedges were divided radially similar to the 120-fold tungsten wedges. The z-location of a p-glue wedge was the average of all slot surface-data exclusive of points in the crater region.

5.1.4 Crater anomalies

Craters were modeled with negative-density glue (n-glue) wedges that effectively subtracted volume from the p-glue. The z-location of an n-glue wedge was the same as the associated p-glue wedge, and the thickness was determined by surface-data in the crater region. The 120-fold crater region was defined as the central 0.5° expanse of the attractor slot, divided into radial sections similar to the p-glue. The 18-fold crater regions were assigned *ad hoc* as single wedges and were of different sizes and locations for the pendulum and attractor.

The glue-fill and craters of all models are illustrated in the color map data of Figure 5.4.

5.1.5 Rim-protrusion anomaly

The tungsten protrusion was modeled with multiple wedges that approximated the shape seen in the outer radius edge data (Figure 5.5). The models had 2 (3) wedges located at $z = 0$ and centered in angle on the nominal 18-fold tungsten for the pendulum (attractor).

The glue protrusion was studied by taking laser scans of the walls of the Pyrex. We found that the glue filled a region about 0.1 mm thick between the foil surface and the chamfered edge of the Pyrex, and that the squeezed out glue traveled up the wall of the

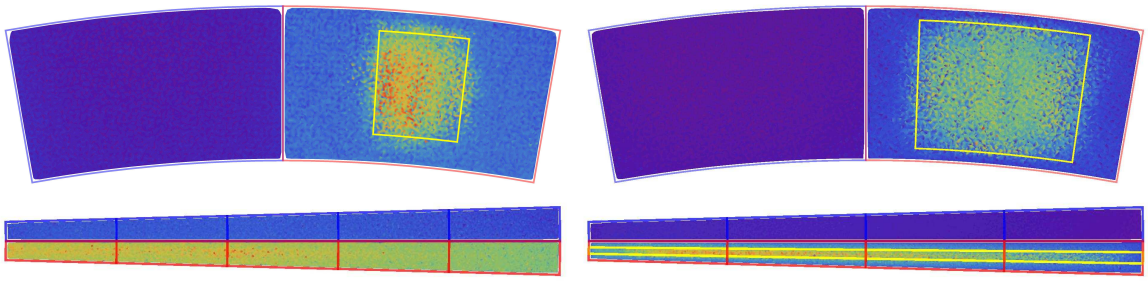

Figure 5.4: 18-fold (top) and 120-fold (bottom) laser scan data and gravity models for the pendulum (left) and attractor (right). For the gravity models, the tungsten boundaries are indicated by blue lines, positive-density glue boundaries by red lines, and negative-density glue boundaries by yellow lines. Color maps, indicating z-height, are not normalized across all figures. See Figure 5.3 for comparitive z-height information.

Pyrex for approximately 0.2 mm. We also determined the total volume of glue contributing to the 18ω signal. The 18-fold pattern of the glue was both in the chamfer region and along the Pyrex wall, so we modeled the glue as two simple wedges, 0.1 and 0.2 mm thick, $\beta = 10°$, with the appropriate radii to match the volume as determined by our scans. It was not necessary to make a more elaborate model because of the low density of the glue and because it was relatively far away from the rest of the model.

5.2 Effects of modeling on torque calculations

The desired accuracy of the torque calculations dictated the level of complexity required in the gravitational models. As mentioned in Section 4.3, the cumulative statistical certainty of the W3 data set was about 1%, so we set an accuracy goal for the gravitational models of 0.05% to ensure that modeling uncertainties were negligible.

We compensated for dishing by dividing the 120-fold wedges into 5(4) radial sections for the pendulum (attractor). The top panel of Figure 5.6 indicates that this number of sections was adequate to meet our accuracy goal, as the variation in the calculation by further refining the model was much less than 0.05%. This analysis used the W1 surface data, which showed the greatest dishing of any set and was therefore most sensitive to this sort of modeling perturbation.

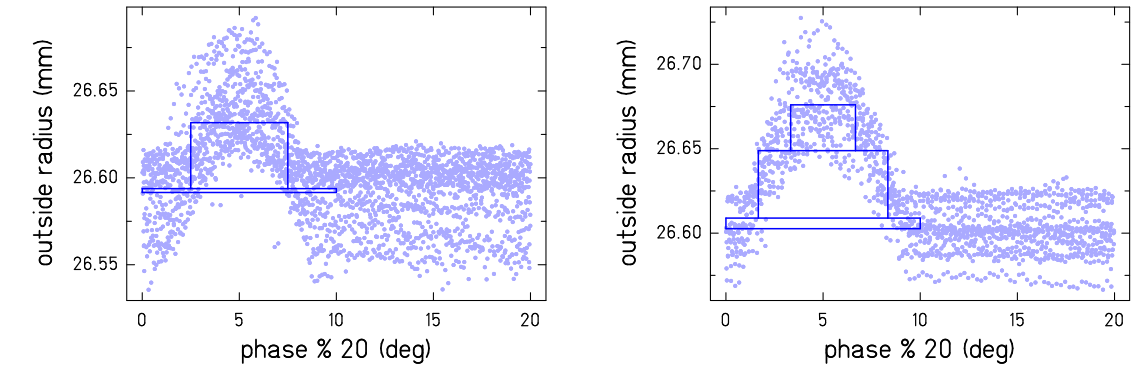

Figure 5.5: Edge location data of tungsten outer rims and rim-protrusion models for the pendulum (left) and attractor (right).

Similarly, the rim-protrusion models indicated refining the number of wedges beyond those chosen in the models resulted in corrections to the torque calculations of much less than 0.05%.

An 18-fold model with glue-fill that didn't include (i.e. averaged over) craters gave a ≈7.34% correction to the nominal, no glue-fill 18ω torques (approximate amount is because it depends on s, not because it was not well calculated). Adding craters, as described above, corrected that model by ≈0.47%, which was a 15× smaller correction. Any further refinement of the crater model would likely yield another 15× reduction in effect, and it would be a $< 0.05\%$ correction. We believe, therefore, that our models for the glue-fill and craters were adequate to meet our accuracy goal.

The cumulative effect of all corrections to the nominal model is shown in the bottom panel of Figure 5.6.

5.3 Gravitational torque tables

The purpose of the gravity model was to generate accurate look-up tables listing expected 18ω and 120ω torques for a given set of parameter values. A separate table was calculated for each value of the Yukawa range λ with which we wished to fit the twist data. ($\lambda = \infty$ is Newtonian gravity.)

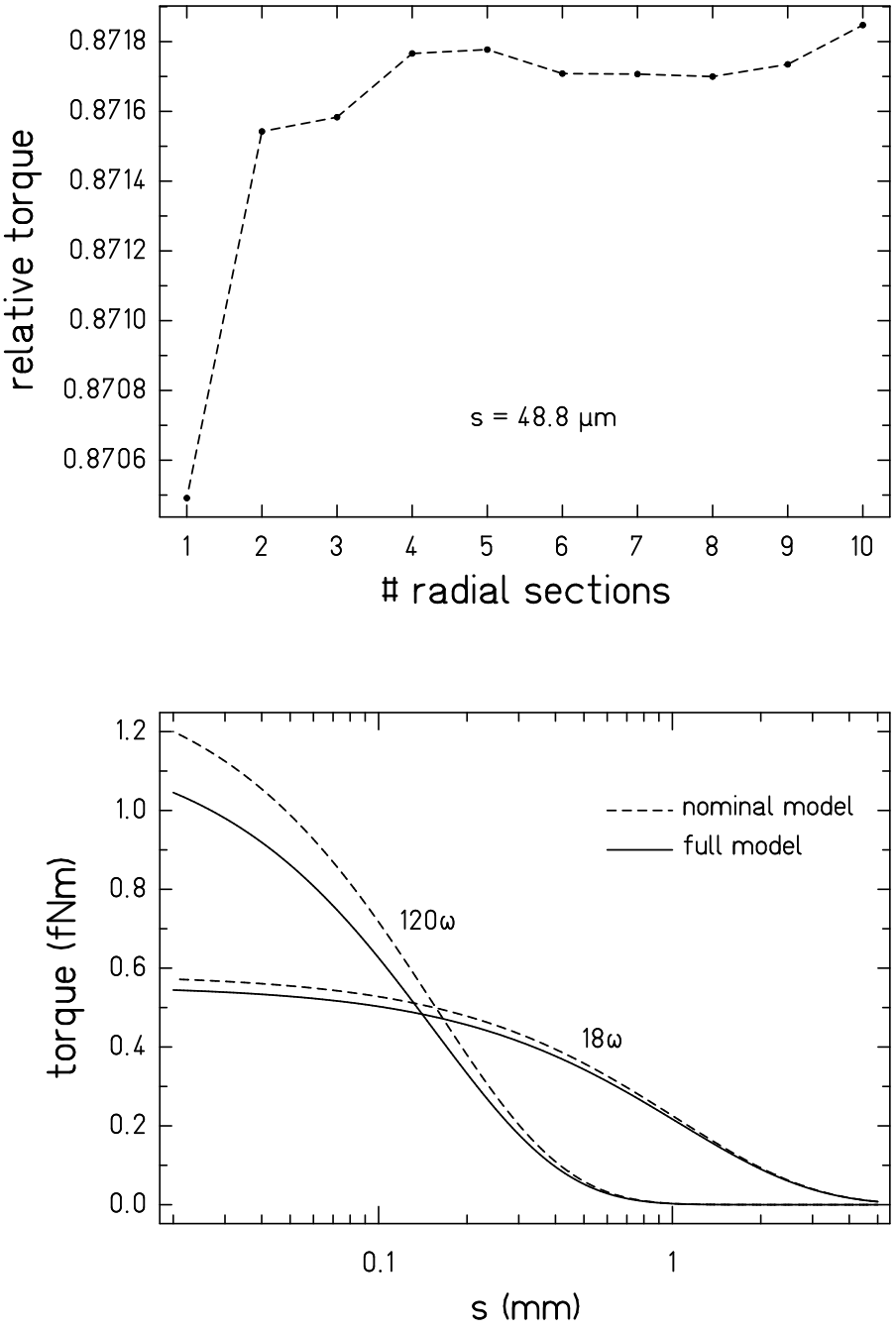

Figure 5.6: Modeling effects on torque for gravity model. TOP: The 120ω Newtonian torque calculation converges as more radial sections are used to model dishing. At around 4 or 5 sections it levels off. The data are plotted relative to the nominal torque. BOTTOM: The cumulative effect of the anomaly modeling on the 18ω and 120ω torques. The glue-fill and dishing both lower the 120ω torque amplitude. Glue-fill also lowers the 18ω torque amplitude, while craters and the rim-protrusion mitigate the effect.

Parameters that defined the torque model fell into three categories:

1. Static parameters were constrained so well by independent measurements that they did not need to be adjusted in the model when fitting the data. (e.g. wedge radii and surface contour)
2. Analytic parameters had measured uncertainties large enough that varying them within errors had a significant effect on the expected torque, and the effect could be calculated analytically. (e.g. foil masses)
3. Table parameters also had significant uncertainties, but adjusting their value required the full Fourier-Bessel calculation to determine the effect on the torque.

The adjustable table parameters were pendulum thickness t_p, attractor thickness t_a, glue density relative to that of tungsten $\hat{\rho}_g$, and an over-cut parameter ϵ, which accounted for surface roughness along all EDM cuts. We calculated the torque tables with high-low bounds for these parameters, chosen to safely encompass their independently measured values (Chapter 4). The [low, high] values used were [51.5, 57.5] μm for both t_p and t_a, [0.0463, 0.0523] for the unit-less $\hat{\rho}_g$, and [0, 3] μm for ϵ.

Each table had calculated torques at 100 values of s (logarithmically spaced from 20 μm to 5 mm) for all permutations of the high-low parameters. ($100\times2^4\times$(two signal frequencies) = 3200 calculated torques per λ value.) The large number of s values accommodated spline interpolation of torques that varied exponentially, while the high-low values accommodated multi-linear interpolation of torques that varied (essentially) linearly.

A simplified version of the gravity model (without dishing, craters, or rim-protrusion, but including average glue-fill) was also used in the off-center calculations discussed in Section 2.2.

5.3.1 Over-cut parameter

Of the four high-low adjustable parameters, the over-cut parameter was the least trivial to implement.

As discussed in Section 4.4, the over-cut parameter accounts for surface roughness along the edges of EDM cuts. Gravitationally, the average of the peaks and valleys is what

determines the edge location.

For the 42-hole ISL experiment of [6], we found that accounting for this phenomenon with a 4.4 μm correction to the hole diameters greatly improved the quality of fit. We have therefore included this effect as a parameter of our torque tables, despite this experiment having much smaller roughness values.

Over-cut corrections were applied only to those surfaces in the model that were EDM'd (most n-glue wedges and the glue protrusion required no correction). The parameter ϵ was a positive value that represented shifting the edge location to enlarge the slots. The wedge geometry does not accommodate this type of correction to the straight walls of the wedge, but the average effect can be approximated by a change in β. The various surface corrections were

$$ir = ir - \epsilon \qquad \text{(tungsten \& glue \& rim-tungsten)} \tag{5.1}$$

$$or = or + \epsilon \qquad \text{(tungsten \& glue)} \tag{5.2}$$

$$or = or - \epsilon \qquad \text{(rim-tungsten)} \tag{5.3}$$

$$\beta = -2 \ \arctan\left(\frac{2\ \epsilon}{ir + or}\right)\frac{180}{\pi} \qquad \text{(tungsten \& rim-tungsten)} \tag{5.4}$$

$$\beta = +2 \ \arctan\left(\frac{2\ \epsilon}{ir + or}\right)\frac{180}{\pi} \qquad \text{(glue)} \tag{5.5}$$

The corrections to the radii have an $\mathcal{O}(\epsilon)$ effect on the calculated torques, while the corrections to β have an effect on the torque of $\mathcal{O}(\epsilon^2)$ when β nominally equals half the symmetry angle. This means the over-cut correction's net affect is to increase signal sizes due to radially-longer wedges.

5.4 Capacitance model geometries

The capacitance models needed to accurately represent the surface details of the pendulum and attractor, particularly for surfaces in close proximity to the copper shield. However, they also needed to respect the limitations of our finite element software, COMSOL Multiphysics, which meant simplifying the details where prudent. In this section we will discuss the physical geometries of the models and how we implemented them in COMSOL.

5.4.1 Physical capacitance models

The pendulum and attractor were modeled independently because the copper shield isolated their electrostatic environments. The models relied on design drawings for most dimensions, and on SmartScope data for the surfaces closest to the copper screen.

Pendulum model

The elements of the pendulum model were the shield, gold can, fiber, and pendulum. The model truncated at the top of the gold can's chimney, as any additional capacitance from the fiber and shroud would be independent of z_p, contributing only to an offset.

To simplify the model, many surfaces were assumed to have cylindrical symmetry. The non-cylindrical aspects that were modified or ignored were: the 8-fold symmetry of the shield stretcher, the "cuckoo hole" in the gold can, the 6-fold holes of the calibration sphere holder, the mirror cube, and the 4-fold ventilation holes on the side of the pendulum body. All these surface modifications were reasonably assumed to have little if any effect on the shape of the calculated capacitance function, $C_p(z_p)$.

To account for dishing, the exposed surface of the tungsten was modeled by azimuthally sweeping a smooth curve. To construct this curve, all tungsten (r, z) laser data ($\sim$50000 points) were averaged down to a dozen or so points that served as anchors for a spline interpolation. The end points of the curve were at radii determined from optical edge scans, with z values extrapolated from the laser data.

Similarly, the glue-fill surface of the 120-fold slots was modeled by azimuthally sweeping a spline-interpolated curve based on averages of data in the glue regions. Plots of all the curves used for capacitance model surfaces are shown in Figure 5.3.

The glue-fill and crater surfaces of the 18-fold slots were modeled as in the gravity models, with flat surfaces at the average bulk-glue height and the average crater height.

We did not specifically address the rim-protrusion anomaly in the capacitance model. The shape of the rim was inconsequential so long as the total area was properly counted with the choice of outer radius.

Attractor model

The elements of the attractor model were the shield, attractor, and cup supporting the attractor. The model truncated just above the flywheel of the bearing assembly.

All elements of this model, besides the top surface of the attractor, respected cylindrical symmetry in actuality and required no approximations. The top surface of the attractor was modeled analogous to the bottom surface of the pendulum described above, but with the inclusion of the 120-fold craters treated in a similar manner to the glue-fill.

5.4.2 COMSOL capacitance models

Our COMSOL models were not simply full-3D re-creations of the physical capacitance models. Instead, we found that separating each model into sub-models and taking full advantage of symmetries achieved improved accuracy and fewer compiling errors. This was due to significantly higher mesh densities that more accurately sampled the solution volume, and less complex geometries that did not test the limits of the (often finicky) meshing algorithms.

Our models took advantage of three types of symmetry: cylindrical symmetry modeled in 2D, repeated rotational symmetry modeled in 3D but with limited angular scope, and reflection symmetry that cut the angular scope of the rotational symmetry in half. Thus, our physical models that had 3-fold, 18-fold, and 120-fold features had sub-models with angular extent of 60°, 10°, and 1.5°, respectively.

Pendulum sub-models

The pendulum and its environment were modeled with 4 quasi-independent sub-models (Figure 5.7).

A 2D axial-symmetric sub-model modeled the entire pendulum environment minus the details of the glue surfaces and calibration spheres. It had artificial interior boundaries (r1, r2, r3, and z1) from which the solution was extrapolated to corresponding surfaces on the 3D models. It was also used to integrate capacitance in the volumes not addressed by the 3D sub-models. Most significantly, it solved near the inner and outer radius edges where

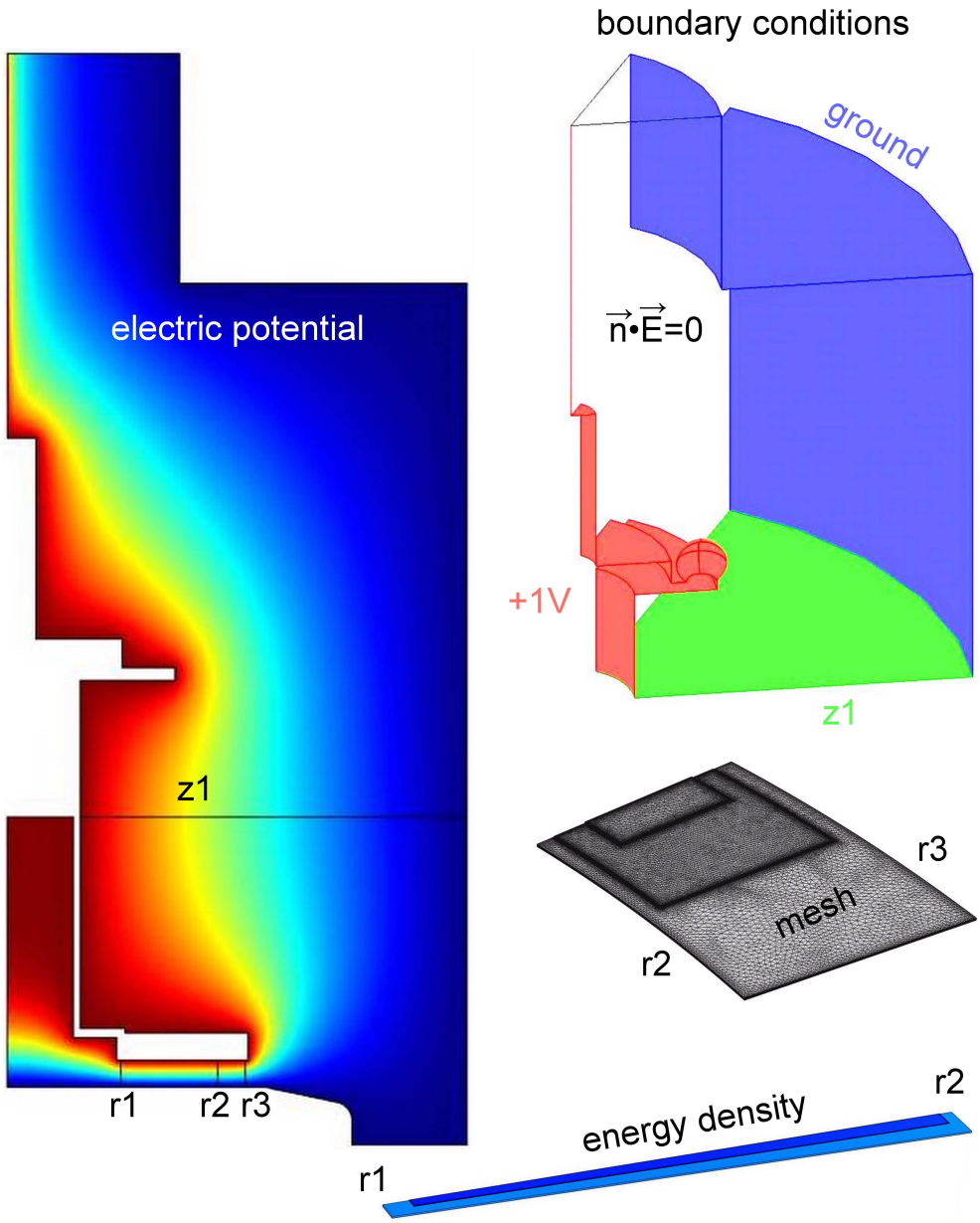

Figure 5.7: Pendulum COMSOL model. LEFT: the 2D axial-symmetric sub-model with potential solution for $z_p = 3$ mm. The boundaries r1, r2, r3, and z1 provide boundary conditions to the corresponding surfaces of the 3D models. RIGHT TOP: A 60° section including half a calibration sphere models the upper half of the pendulum. The $\vec{n} \cdot \vec{E} = 0$ boundary condition applies to the side walls and chimney top. RIGHT MIDDLE: the 18-fold sub-model with representative mesh. Points are purposely concentrated near edges where field lines are most divergent. RIGHT BOTTOM: the 120-fold sub-model with surface colors representing energy density for $z_p = 0.03$ mm. The darker region beneath the glue has less energy density and therefore contribute less to the capacitance.

electric field lines were most divergent. Because this model was 2D, it could be meshed at extremely high densities yet solved with relatively little computing overhead.

The top portion of the pendulum (everything above the z1 boundary) had its own sub-model to properly account for the three calibration spheres. While this portion of the model makes a negligible contribution to the capacitance when z_p is very small, at large z_p the proximity of the pendulum to the top of the can contributes more significantly to the total capacitance.

The 120 and 18-fold sub-models modeled the remaining volumes between r1 and r2, and r2 and r3, respectively, including the glue regions.

Boundaries r1, r2, and r3 were placed at radii far from the slot radii (distance from slot $\gg$ slot depth) so that their use as boundary conditions in the slotted models would not artificially coerce the fields. For similar reasons, the z1 boundary was placed well below the calibration sphere height.

Attractor models

Three quasi-independent sub-models modeled the attractor and its environment: a 2D axial-symmetric sub-model (Figure 5.8), a 120-fold 3D sub-model, and an 18-fold 3D sub-model. As with the pendulum models, the 2D sub-model provides boundary condition solutions at r1, r2, and r3 for use in the 3D sub-models.

5.5 Determining z_p and z_a

The COMSOL models were used to generate the capacitance functions $C_p(z_p)$ and $C_a(z_a)$. These functions, along with a few modeling parameters, were then used to fit "z-scan" data (Section 5.5.2) to produce capacitance functions $\bar{C}_p(z_p)$ and $\bar{C}_a(z_a)$ representing the true response of our system. The $\bar{C}$ functions were then inverted to create functions $Z_p(\bar{C}_p)$ and $Z_a(\bar{C}_a)$ to provide z_p and z_a values given measured capacitances. All these functions are discussed in greater detail in the following sections.

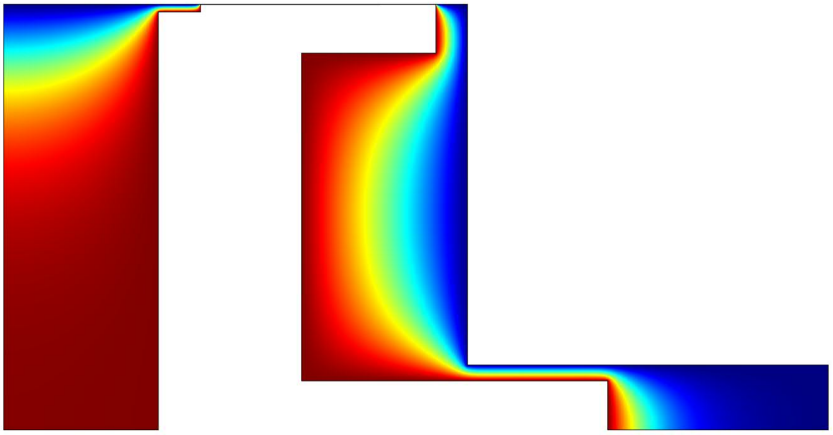

Figure 5.8: Attractor 2D axial-symmetric COMSOL sub-model with potential solution for $z_a = 0.014$ mm. The left edge of the model is the rotation axis. The attractor model also had 18 and 120-fold sub-models (not shown) that were similar to the pendulum sub-models shown in Figure 5.7

5.5.1 Capacitance from COMSOL

To calculate capacitance from our COMSOL models, we used the electrostatic energy identity

$$U = \frac{1}{2}CV^2. \tag{5.6}$$

In our models, we chose $V = 1$ by setting boundary conditions on the pendulum and attractor at +1 volt and setting the screen and contiguous surfaces at ground. COMSOL explicitly solved the models for the electric potential, but COMSOL also provided the solution as components of the vector electric field, $\vec{E}$, at each mesh point. The total energy, U, was calculated by integrating the energy density, $\epsilon_0\vec{E}^2/2$, over all model volumes. Therefore,

$$C_p = \epsilon_0 \left(2\pi \int_{S_{2D}} r\vec{E}^2 + 240 \int_{V_{120}} \vec{E}^2 + 36 \int_{V_{18}} \vec{E}^2 + 6 \int_{V_{top}} \vec{E}^2 \right) \tag{5.7}$$

for the pendulum, and C_a had a similar expression without the V_{top} term. Adjusting z_p or z_a effected both the $\vec{E}$ solutions as well as the integration volumes. Figure 5.9 shows the contribution of each sub-model to $C_p(z_p)$.

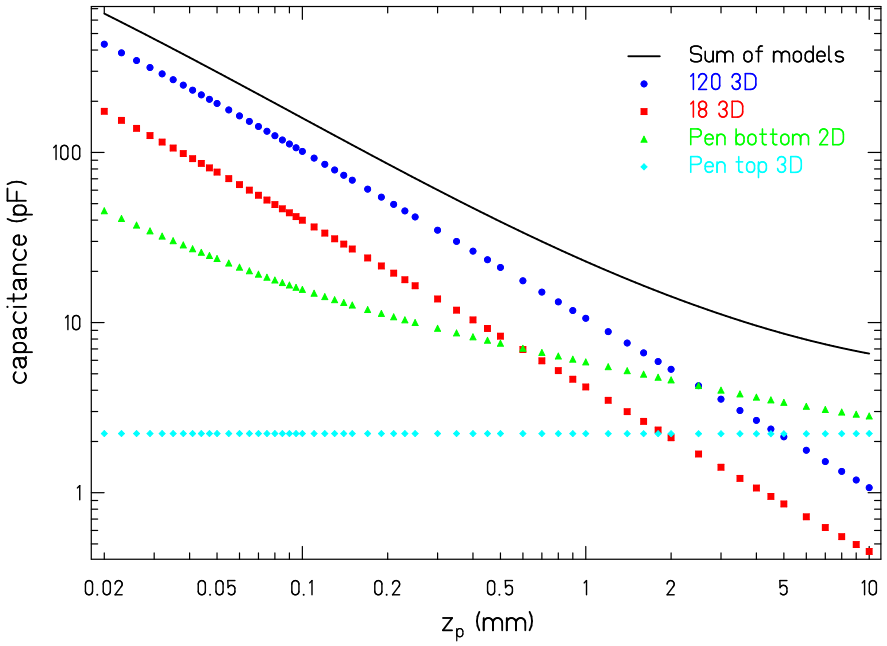

Figure 5.9: Sub-model contributions to the pendulum capacitance calculation.

5.5.2 Fitting z-scans

The COMSOL functions were used to fit z-scan data and provide an empirical model of our system. We collected z-scan data by physically adjusting z_p or z_a and recording both the capacitance and an independently measured z-height. The z_p adjustment was performed with the motorized phi-top assembly, with position information provided by the z-micrometer on the phi-top stage. The z_a adjustment was performed by hand, loosening the three spring-loaded, screen-leveling screws by the same amount (± 2 μm, roughly) for each measurement, while the attractor assembly was mounted on the SmartScope. The SmartScope laser provided position information for the change in height of each individual leveling screw, as well as the overall change in z_a.

We fit the z-scan data with the function

$$\bar{C}(z) = a_1 + a_2 C(z - a_3) + \frac{1}{2} C''(z - a_3) a_4^2, \tag{5.8}$$

where a_1 accounts for stray capacitance in the system, a_2 accounts for gain error in the capacitance meter, a_3 accounts for the arbitrary origin of the independent z-height measurement, and a_4 accounts for RMS z-averaging in the measurement resulting from pendulum bounce and non-parallelism of the screen with the pendulum or attractor surfaces. Since C was calculated at discrete z-heights in COMSOL, a spline interpolation of C was used to create $\bar{C}$. The fitting procedure minimized χ^2 using solution-dependent data uncertainties of

$$\sigma^i(z) = \sqrt{{\sigma_c^i}^2 + \left(\sigma_z \frac{\mathrm{d}\bar{C}(z)}{\mathrm{d}z}\right)^2}, \tag{5.9}$$

where σ_c^i is the uncertainty in the capacitance measurement of the i^{th} data, and σ_z is the uncertainty in z-height measurements. Figure 5.10 shows z-scan data for the pendulum with best-fit $\bar{C}_p(z_p)$.

5.5.3 $Z(\bar{C})$ functions

$\bar{C}(z)$ provided the expected physical capacitance reading for a given z-position as measured by the z-micrometer or SmartScope laser of the pendulum or attractor. The endgame of the capacitance models, however, was to translate the physical capacitance readings into z-heights relative to the screen surface. To create the function $Z_p(\bar{C}_p)$ we spline-interpolated the array of points $\left\{\bar{C}_p(z_p + a_3), z_p\right\}$, where the z_p's were the same values used in the COMSOL models to create $C_p(z_p)$. Note that $Z_p(\bar{C}_p)$ is actually independent of a_3, the arbitrary zero height of the z-micrometer, as would be expected. The $Z_a(\bar{C}_a)$ function was built in the same manner.

The pendulum z-heights of all data runs, and the set-distance of the attractor, were determined with these functions. Additionally, all plots within this thesis that display data vs. z_p or z_a have used these functions to convert the physical capacitance data.

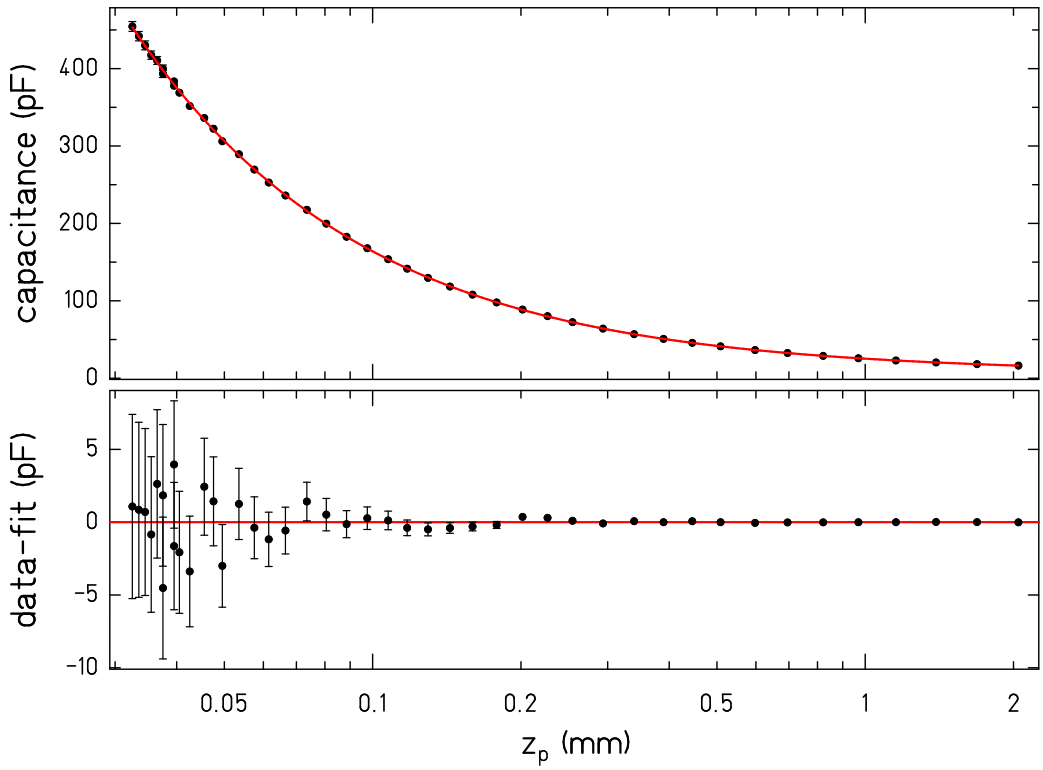

$\bar{C}_p(z_p)$ fit parameters

stray (a_1)	2.1 ± 0.003 pF
gain (a_2)	1.012 ± 0.0001
$z0$ (a_3)	20.5 ± 0.1 μm
RMS bounce/tilt (a_4)	6.2 ± 0.5 μm
χ^2/DOF	38.7/40

Figure 5.10: Fit of pendulum z-scan data with $\bar{C}_p(z_p)$. The $\sigma^i(z_p)$ uncertainties (Equation 5.9) blow up at small z_p due to $\sigma_z = 0.5$ μm for the digital micrometer which reads to 1 μm. The data and fit function have been shifted by a_3 in order to plot vs. z_p.

Chapter 6

EXPERIMENTAL METHODS

This chapter details the procedures used to align the apparatus, clear dust from the critical regions, and collect data.

6.1 Alignments

The pendulum and attractor needed to be aligned (Figure 6.1) to achieve maximal sensitivity to new physics and reduce modeling complexity. Many of our alignment techniques evolved from previous generations of this experiment. The most important innovations were acquisition of the SmartScope system which provided new methods for measuring component alignments, and the development of spring-loaded attractor and screen mounts that greatly improved adjustment precision.

6.1.1 Estimated Impact of Misalignments

When aligning parts, it is useful to know what impact misalignments will have on the experiment so one can judge when things are "aligned enough". The following is the general framework we used for calculating these estimates.

Consider the Taylor series expansion of $f(x+\delta)$ around the point x:

$$f(x+\delta) = f(x) + \delta f'(x) + \frac{1}{2}\delta^2 f''(x) + \mathcal{O}(\delta^3). \tag{6.1}$$

The average of δ-sized excursions in either direction about x is

$$\begin{aligned} \bar{f}(x,\delta) &= \frac{1}{2}\left(f(x+\delta) + f(x-\delta)\right) \\ &= f(x) + \frac{1}{2}\delta^2 f''(x) + \mathcal{O}(\delta^4). \end{aligned} \tag{6.2}$$

If f (the numerical model) is a linear function, or effectively linear over the range $x \pm \delta$, then $\bar{f}$ (the lab measurement) is well approximated by f. But if f is highly nonlinear and

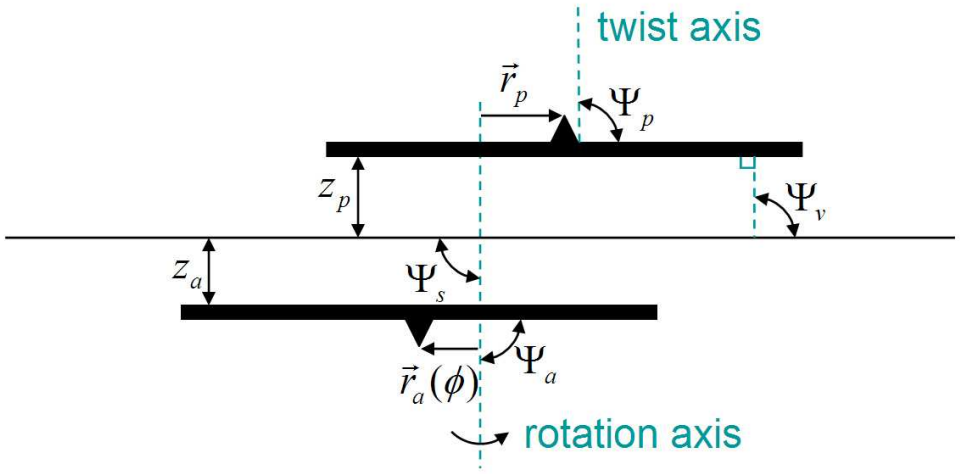

Figure 6.1: Alignment schematic of the pendulum, attractor, electrostatic screen, and apparatus. The attractor and screen were aligned to the axis of rotation, the pendulum was aligned to the twist axis, and the whole apparatus was aligned to bring the screen parallel with the pendulum. In most cases we measured alignment angles $\theta_x = \Psi_x - \pi/2$. All alignments, once made, were fixed except for z_p and r_p, which were adjustable with phi-top. The torque signals were insensitive to misalignment of the pendulum's center (small triangle) with the twist axis.

f'' is large, $\bar{f}$ can differ significantly from f for even modest values of δ. With regards to this experiment, f represents the gravity and capacitance models, both of which were highly non-linear.

For time-varying oscillations δ is easily interpreted as the RMS oscillation amplitude, assuming the oscillation period is short with respect to the measurement time. For the purpose of angle alignments, δ may also represent spatial variance from tilts, provided the geometry is symmetric about an arbitrary tilt axis.

6.1.2 Attractor Alignment

The attractor had to be aligned so that the top plane was perpendicular to the axis of rotation, and the wedge pattern was centered on the axis. To achieve this, we developed a kinematic adjustment system that allowed us to tune the tip-tilt degrees of freedom independent of the centering degrees of freedom (Figure 6.2). These alignments were performed

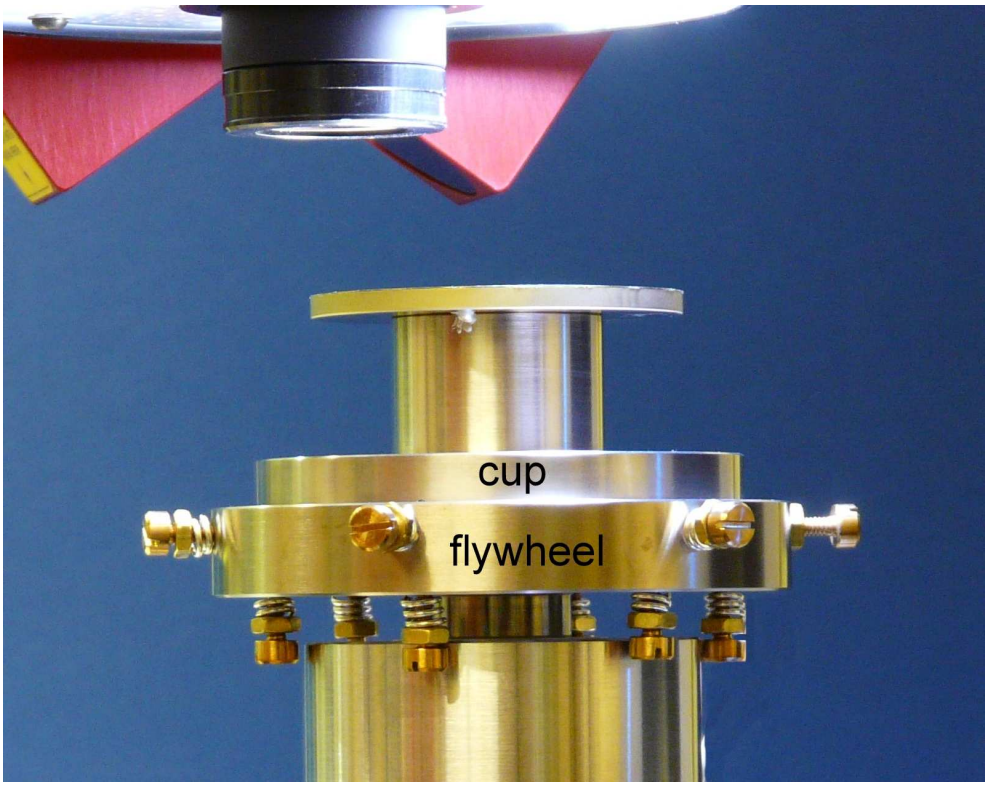

Figure 6.2: Picture of the attractor's kinematic adjustment. Two horizontal screws provided centering adjustment of the cup, and three vertical screws provided tip-tilt adjustment. Additional dummy screws maintained a six-fold symmetry to prevent gravitational interaction with the three calibration spheres on the pendulum. Compression springs located between the cup and flywheel held the cup horizontally against the centering adjustment screws, and compression springs on the three dummy vertical screws pulled the cup down onto the three tip-tilt adjustment screws.

with the attractor assembly securely mounted to the SmartScope.

Center on axis of rotation

We defined the center of the attractor by the outside radius of the 120-fold pattern. The SmartScope optics were aligned such that the tangent of a single 120-fold outside edge in the field of view was parallel to the x-axis. The y-location was measured for these edges as the bearing was rotated by hand, and centered alignment was achieved by minimizing the 1ω component of the runout (Figure 6.3 top). We found it feasible to tune the attractor

center to within 10 μm of the rotation axis.

A centering misalignment of the attractor, $\vec{r}_a(\phi)$, along with $\vec{r}_p$, the corresponding offset of the pendulum, creates a time-dependent r-offset vector $\vec{r}(\phi) = \vec{r}_p - \vec{r}_a(\phi)$ due to the attractor's rotation. These offsets modulate the torque amplitudes but their phases are unaffected. We can define maximum and minimum offset quantities $r_+ = r_p + r_a$ and $r_- = |r_p - r_a|$, whose mean represents the average offset and whose difference represents the peak-to-peak modulation amplitude. Using Equation 6.2, the time-average of the torque amplitudes can be expressed as

$$\bar{N}_m(\vec{r}(\phi)) = N_m\left(\frac{r_+ + r_-}{2}\right) + \frac{1}{2}\left(\frac{r_+ - r_-}{2\sqrt{2}}\right)^2 N''_m\left(\frac{r_+ + r_-}{2}\right), \tag{6.3}$$

where $N_m(r)$ is the torque as a function of r-offset for the signal with m symmetry. This expression can be tidied up by defining $r_>$ as the greater value of r_p and r_a and $r_<$ as the lesser value of r_p and r_a, so that

$$\bar{N}_m(\vec{r}(t)) = N_m\left(r_>\right) + \frac{r_<^2}{4}\, N''_m\left(r_>\right). \tag{6.4}$$

Figure 6.4 shows the relative impact attractor misalignments have on the torque.

Perpendicular to axis of rotation

Height measurements of the top surface were taken near the outside rim. The SmartScope laser probe was stationary as the attractor bearing was rotated by hand, and perpendicular alignment was achieved by minimizing the 1ω component (Figure 6.3 middle). The interpretation of this leveling data assumes the absence of "rumble". Coherent vertical motion of the attractor at 1ω would be degenerate with surface tilt when measured with the fixed laser. We checked for this effect by averaging surface height data taken with the laser at two positions on opposite sides of the attractor. We found our bearing assembly to have negligible 1ω rumble (Figure 6.3 bottom).

The consequence of an attractor leveling misalignment can be estimated by the torque expression

$$\bar{N} = N(\bar{s}) + \frac{1}{2}a_s^2(\theta_a)N''(\bar{s}), \tag{6.5}$$

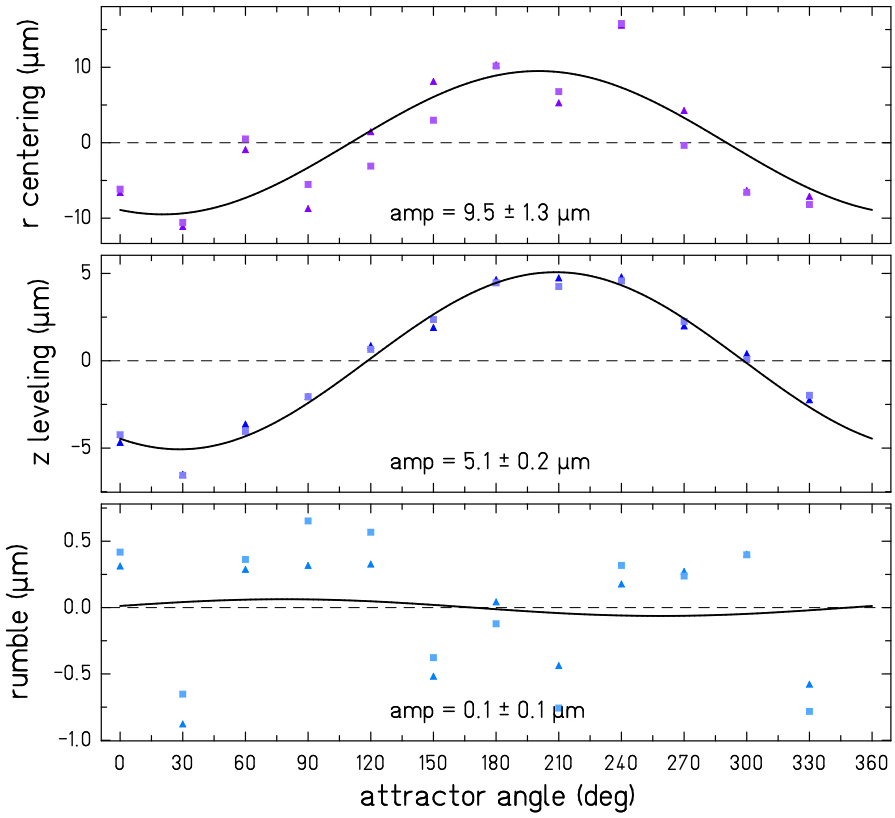

Figure 6.3: Attractor alignment to axis of rotation for W3 data set. The attractor was rotated by hand two full revolutions, collecting data every 30° (as judged by eye with the aid of screws located every 60°). Square points are from first rotation, triangle points from second. TOP: final centering of the 120-fold pattern to the rotation axis. Middle: final leveling of the top attractor surface, with intentional slope to accommodate an upward poking protrusion on the outer rim near 25°. BOTTOM: data for this plot were taken with the laser at two opposite positions near the attractor outer rim and the plotted points are their average. The small 1ω signal indicates leveling data was truly measuring the tip-tilt angle and not coherent z-motion of the attractor.

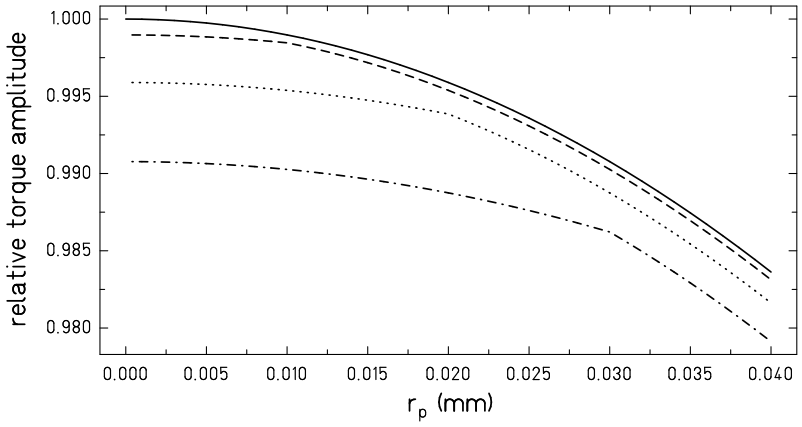

Figure 6.4: Relative impact of attractor misalignment on the time-averaged 120ω torque amplitude. Attractor misalignments of r_a = 0, 10, 20, and 30 μm are shown. When r_p becomes less than r_a the effect on the torque amplitude transitions from 2$^{\text{nd}}$ order to 1$^{\text{st}}$ order.

where $N(s)$ is the torque as a function of separation and $a_s(\theta_a)$ is the RMS height of the area contributing to the torque signal with respect to the average separation distance $\bar{s}$. This definition of a_s assumes patches of equal area contribute equally to the torque. If the change in height due to tilt θ_a is given by $r\sin(\theta_a)\sin(\phi)$, where ϕ is the azimuthal angle, then

$$\begin{aligned} a_s^2(\theta_a) &= \frac{1}{\pi\left(or^2 - ir^2\right)} \int_0^{2\pi} \int_{ir}^{or} \left(r\sin(\theta_a)\sin(\phi)\right)^2 \, r\, dr\, d\phi \\ &= \frac{1}{4}\left(or^2 + ir^2\right)\sin^2(\theta_a). \end{aligned} \tag{6.6}$$

Plugging in the appropriate radii gives ${}^{18}a_s = 17.5\sin(\theta_a)$ mm and ${}^{120}a_s = 13.2\sin(\theta_a)$ mm.

The final attractor adjustment was set intentionally non-perpendicular to accommodate an anomalous $\approx$ 10 μm protrusion sticking up on the outer rim. To put the attractor as close to the screen as possible (on average), the attractor was tilted to bring the protrusion away from the screen and roughly even with the opposite side. The 5 μm of tilt measured near the outside rim corresponds to $\theta_a = 200$ μrad and scales the torque by 1.00015 for the 120ω signal at the closest separations, which is a modification well below the cumulative statistical certainty. The modification is even less for the 18ω signal.

This tilt also modifies the interpretation of capacitance measurement used to determine z_a, as discussed in Section 5.5.2.

6.1.3 Electrostatic Screen Alignment

The electrostatic screen also needed to be perpendicular to the axis of rotation and as close to the attractor as possible without making contact. In previous versions of this experiment, we manipulated the bearing assembly mounts to bring the attractor into alignment with the fixed screen, which was a difficult and tedious procedure. We simplified this process and improved precision by performing the final adjustments to the screen itself. To do this, we added spring washers between the screen stretcher and the mounting tube it sits on and adjusted the three fastening screws.

We attempted to set the screen utilizing the precision of the SmartScope, but found the alignment changed considerably after mounting the assembly in the apparatus. Securing the base plate of the assembly to the "spider" structure warped it slightly, moving the attractor away from the screen by a few microns. Additionally, temperature changes from the lab environment to the vacuum environment revealed thermal expansion differences between the attractor and screen mounts. We addressed these issues by performing all final adjustments with the assembly mounted in the spider (with vacuum can removed), and by replacing the screen's aluminum mounting tube with one made of G10 epoxy laminate which had a CTE similar to the titanium components of the attractor mount.

Our tool for measuring the screen alignment was capacitance. With a rotating attractor, observing a 1ω attractor-screen capacitance modulation indicated screen-tilt. This sensitivity was thanks to the 200 μrad leveling misalignment of the attractor to the rotation axis. Using Equations 6.6 and 6.2, we calculated the capacitance modulation amplitude as a function of screen tilt

$$\tilde{C}(\theta_s) = \frac{1}{2}\left(\bar{C}(\theta_a + \theta_s) - \bar{C}(\theta_a - \theta_s)\right). \tag{6.7}$$

We were able to bring the screen within 20 μrad of normal to the axis of rotation. We set the overall attractor-screen separation near $z_a = 17$ μm, but the gap slowly shrank by

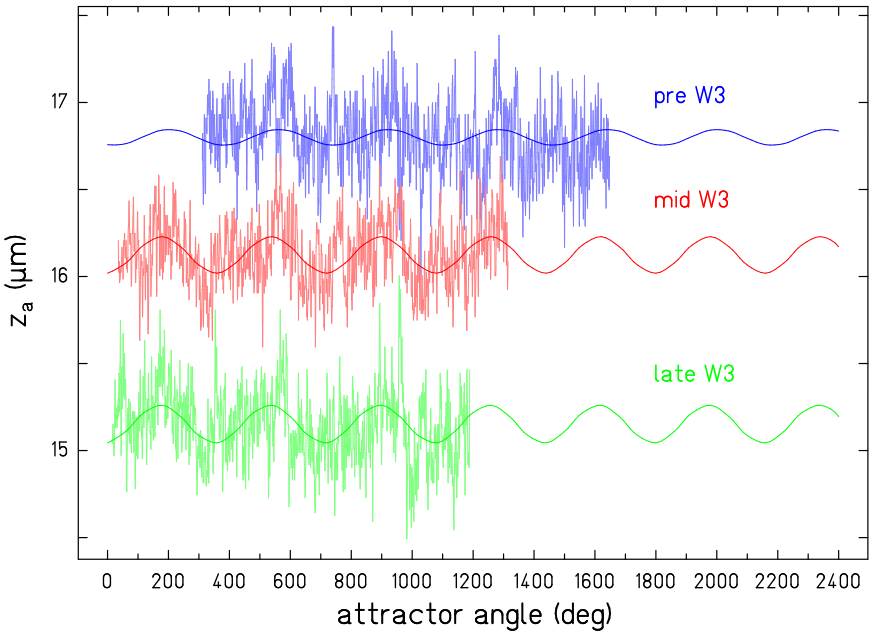

Figure 6.5: Attractor-screen capacitance data collected periodically during the W3 data set as a check of alignment stability is plotted in units of μm of z_a. A z_a-drift of nearly 2 μm was observed over the two month collection period. With a conversion factor of 200 μrad of tilt per micron of modulation amplitude at these separations, the 1ω modulations indicate screen misalignments of $\theta_s = 10 \pm 2$ μrad in the pre W3 trace, and $\theta_s = 20 \pm 2$ μrad in the other two.

almost 2 μm over the course of the data set. Figure 6.5 shows the capacitance data used for these alignments interpreted in units of μm of z_a.

6.1.4 Pendulum Alignment

We aligned the bottom surface of the pendulum to be perpendicular to the twist axis of the fiber. Our procedure for this alignment was unchanged from the previous experiment[9]. We achieved pendulum misalignment of $\theta_p < 100$ μrad. Because the attractor is aligned to the pendulum regardless the pendulum's angle (discussed below), these misalignments only affect the moment arm of the torques acting on the pendulum, scaling the 18ω and 120ω signals by $1/2\,(1 + \cos(\theta_p)) = 1 - 2.5{\times}10^{-9}$. The effect of our measured pendulum

misalignment was completely negligible.

6.1.5 Apparatus Alignment

We brought the screen into parallel alignment with the pendulum by adjusting the tilt of the vacuum vessel. This procedure was also unchanged from the previous experiment.

While setting the apparatus alignment can be done with precision of $\theta_v \approx 10$ μrad, a relevant question is whether the apparatus retains that alignment over the course of data collection (Figure 6.6). Such operations as installing the calibration table (W1) and changing the apparatus temperature (W2) produced gross shifts in the apparent tilt of the apparatus. Despite these events, the total divergence from the set points was $\theta_v < 100$ μrad.

Unfortunately, we neglected to align the apparatus before data set W3. Limits on θ_v can be extrapolated, however, from the capacitance model fit to z-scan data of the pendulum (Section 5.5.2). If the bounce-tilt fit parameter of 6.2 ± 0.5 μm is interpreted purely as tilt misalignment between the pendulum and screen, then Equation 6.6 sets $\theta_v < 450$ μrads. The tilt misalignment was likely considerably less than this limit since pendulum bounce was surely nonzero. The effect of this tilt on the gravitational signals is analogous to attractor tilt, discussed above.

Of greater concern than a static θ_v misalignment is a changing tilt. The primary effect of a changing tilt is to translate the attractor relative to the pendulum due to the ≈ 1 m length of the pendulum and fiber. If the pendulum was initially centered over the attractor, but a tilt change of 50 μrads moved the attractor by 50 μm, the 120ω signal would be systematically decreased by 2% (see the solid line of Figure 6.4). The observed tilt drift of the W3 data set, ≈ 20 μrads, may have decreased the 120ω signal by as much as 0.5%, a significant effect.

A portion of the tilt signal may have been due to temperature response of the AGI sensors themselves and not actual apparatus tilt. Fine temperature control of the AGI environment would remove this ambiguity in future measurements.

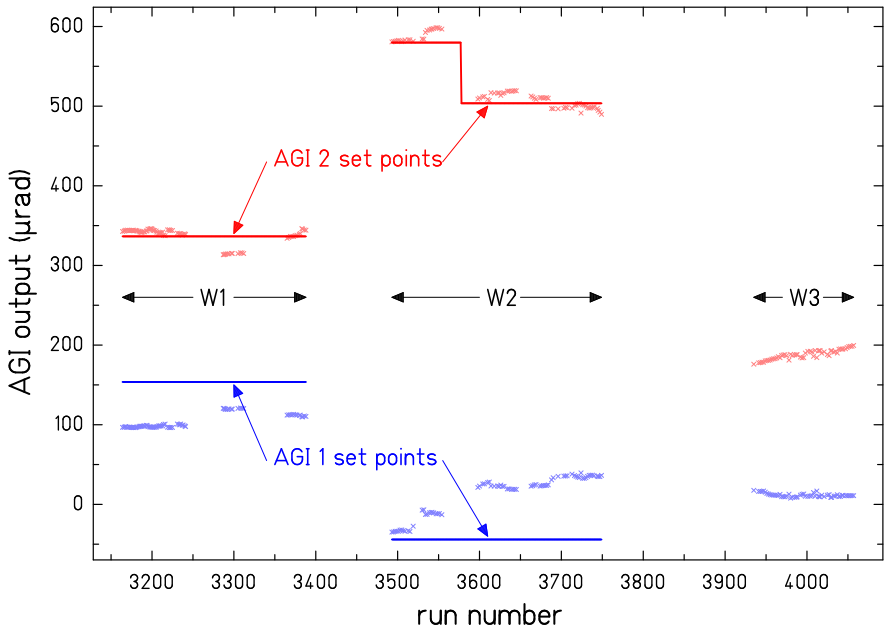

Figure 6.6: Apparatus tilt as monitored with a two-axis Applied Geomechanics, Inc. (AGI) tilt sensor for data runs in sets W1, W2, and W3. The set points represent the determined proper tilt from the apparatus leveling procedure, θ_v is measured as deviation from these lines. In data set W1, the gross offset of AGI 1 data from its set point resulted from installing the calibration table after the leveling procedure was done. Midway through data set W2, the temperature of the apparatus was changed and only AGI 2 was re-leveled. The leveling procedure was accidentally neglected for data set W3 so there are no set points shown.

6.1.6 Alignment Summary

The goal of the total alignment procedure was to achieve attractor-pendulum parallelism with the attractor well centered on its axis of rotation and as close to the electrostatic screen as possible. With a total angular misalignment < 450 μrad and attractor runout < 11 μm, the effect of misalignments was a $< 0.15\%$ deviation from the ideally aligned model for the 120ω signal, which was well below the cumulative statistical certainty of the data set. The angular misalignments had much greater impact on the interpretation of capacitance measurements, and were accounted for in the capacitance models.

6.2 Dust Removal

Small particles between the pendulum and screen or attractor and screen could prevent attaining the desired attractor-pendulum separation distance, as well as produce electrostatic noise. Debris located between the attractor and screen, that dragged along either of the surfaces, could have more dire consequences by increasing noise or creating false signals. We developed several techniques to detect and remove dust from those critical regions.

6.2.1 Pendulum-side dust

Detecting dust between the pendulum and screen was relatively simple. As the pendulum was lowered toward the screen, any contact with dust typically kicked the pendulum off the detector. Checking the vertical position where this occurred required replacing the vacuum can to prevent wind on the pendulum, but did not require pulling vacuum which was a great time saver. We had a goal of reaching $z_p \leq 25$ μm ($\bar{C}_p \geq 600$ pF) without being kicked.

Dust was removed by placing the pendulum at $z_p \approx 100$ μm and sweeping a single 0.003" diameter tungsten fiber, about 4" in length, through the gap. Shining a bright light from behind the pendulum helped make large pieces of dust easily visible. Lowering the pendulum and inducing a large twist helped identify smaller particles; raising the pendulum again let them be swept out. We checked for dust with the pendulum-kick method after no dust could be identified visually.

6.2.2 Attractor-side dust and attractor-screen touching

Identifying dust between the attractor and screen was more difficult. Larger particles produced upward dimples in the screen that were easily visible by eye. Some smaller pieces of dust (or possibly part of the attractor coming into contact with the screen) could be seen by rotating the attractor and noticing a distortion in the screen reflections. Both of these techniques were applied with the attractor on the bench. Two further checks were made once the attractor was installed. The first was to look for glitches in the attractor-screen capacitance as the attractor rotated. This was a clear sign of attractor-screen touching, but not necessarily a sensitive test for dust. The final check was to look for a 1ω modulation of the pendulum-screen capacitance, which was indicative of something pushing on the screen.

Dust was cleaned away by removing the screen from the screen stretcher and swabbing both the attractor and screen with an alcohol soaked, lint free wipe.

6.3 Data Collection

After all alignments were complete, three types of data were collected. *Data runs* provided short-range gravitational data. Those runs were always followed by *sweep runs* which provided nonlinear corrections to the angle measurements and the free torsion period, τ_0. *Calibration runs* provided the twist-to-torque conversion scale.

In contrast to [9] and the W1 data set, data sets W2 and W3 did not employ a full-time calibration signal. Instead, calibration data were collected as a separate series of runs, and the calibration turntable was removed for the *data* and *sweep runs*. This was done because the various hookups (water cooling lines, encoder and vacuum sensor data cable, etc.) required to run the attractor impeded the turntable's range of motion and persistently rubbed on the rotating table, creating an undesirable mechanical coupling of the turntable to the vacuum system.

6.3.1 Science data collection

After alignments and dusting were complete, we performed a few other procedures before beginning data collection:

1. Baked the fiber ($\approx 50^\circ$ C) to remove drift in θ_0.
2. Closed thermal enclosure and turned on water and air circulation systems. It typically took 2-3 days for the apparatus to reach thermal equilibrium.
3. Roughly centered pendulum to attractor. We used half-day runs stepping in x and y to search for the peak in the gravitational torques. When the initial alignment was far off ($r_p \geq 1$ mm, or so), the 18ω signal was more useful as the 120ω quickly lost strength.
4. Rechecked minimum achievable z_p and looked for evidence of attractor touching the screen. Centering the pendulum may have moved it over a piece of dust and thermal expansion movement as the system equilibrated may have moved the attractor (or dust on the attractor) into contact with the screen.
5. Re-leveled the apparatus. Temperature change may have tilted the apparatus slightly. (This step was neglected for the W2 and W3 data sets.)
6. Performed z-scan to determine $Z_p(\bar{C})$ function (Section 5.5.3).

With the system properly prepared, the science runs repeated the following procedure:

1. Moved pendulum to desired (x, y, z) coordinate.
2. Centered the pendulum's angle on the detector and minimized its free torsion amplitude.
3. Started attractor turning. The attractor period was set at $78\tau_0$ (where $\tau_0 \approx 300$ sec was the free torsion period). The multiplier 78 was chosen because it was not an integer harmonic or sub-harmonic of the 18ω and 120ω signals, it was divisible by 6 which provided an integer number of pendulum periods per 60° sub-cut, and it placed the 120ω signal near the minimum of the torque noise spectrum (Figure 7.1).
4. Took data run. Data run lengths ranged from 14-54 hrs., with an average length of 23 hrs. Close-in runs that were maintaining a small free-amplitude (typically on weekends) were allowed to run longer than the usual 1 day. Runs were stopped short if the free-amplitude became too large.
5. Stopped attractor turning.

6. Set pendulum free-amplitude to cover the full extent of the detector covered in the data run, but not by too large a margin (factor of 2 at most).
7. Took sweep run. Sweep run lengths were at a minimum $6\tau_0$. Close-in runs, which had poor noise performance, required longer sweep runs to get an accurate measure of τ_0 and reasonable nonlinearity coefficients.

Table 6.1 lists all *data runs* of the W3 data set with their pendulum positions and measured in-phase (γ) and out-of-phase (β) torque components of the 18ω and 120ω signals.

Table 6.1: Pendulum positions and measured torques of the W3 data set. The position units are in mm and torque units are in fNm. A value in parentheses is the uncertainty for the value to the immediate left. The z_p values have been adjusted based on calendar date to account for z-drift of the attractor. The torque data have been rotated to place the signal primarily in the γ component. These adjustments are discussed in Section 8.2.

Run Name	x-mic	y-mic	z_p	β_{120}	γ_{120}	β_{18}	γ_{18}
run3935	-0.069	-0.44	0.0796 (0.0001)	-0.0033 (0.0093)	0.3744 (0.0057)	-0.0062 (0.0098)	0.5012 (0.0097)
run3941	-0.168	-0.44	0.0789 (0.0001)	-0.006 (0.0118)	0.5117 (0.0066)	0.015 (0.0208)	0.487 (0.02)
run3943	-0.219	-0.439	0.0787 (0.0001)	0.0148 (0.0128)	0.5377 (0.0076)	-0.0138 (0.0159)	0.502 (0.0158)
run3945	-0.298	-0.439	0.0787 (0.0001)	0.0017 (0.0143)	0.5324 (0.0085)	-0.0092 (0.0131)	0.5035 (0.0148)
run3947	-0.376	-0.44	0.0785 (0.0001)	0.0099 (0.0219)	0.4724 (0.01)	0.0104 (0.01)	0.4754 (0.01)
run3949	-0.452	-0.44	0.078 (0.0002)	0.0024 (0.0136)	0.3684 (0.0124)	0.0127 (0.0167)	0.479 (0.0147)
run3951	-0.25	-0.438	0.079 (0.0001)	-0.0053 (0.0143)	0.5525 (0.0083)	0.0064 (0.0087)	0.4938 (0.0094)
run3953	-0.25	-0.419	0.0787 (0.0001)	-0.0052 (0.0146)	0.5722 (0.0081)	0.0005 (0.0114)	0.4706 (0.0117)
run3955	-0.25	-0.518	0.0789 (0.0001)	0.0152 (0.0132)	0.4338 (0.024)	-0.0264 (0.0219)	0.4676 (0.0221)
run3957	-0.25	-0.6	0.0789 (0.0001)	0.0172 (0.0168)	0.2022 (0.0356)	0.0334 (0.05)	0.3503 (0.0545)
run3959	-0.25	-0.331	0.0782 (0.0001)	-0.0022 (0.0111)	0.5894 (0.011)	-0.0218 (0.0145)	0.4799 (0.0152)
run3961	-0.25	-0.23	0.078 (0.0002)	0.0073 (0.0113)	0.4929 (0.0136)	-0.0137 (0.0119)	0.4766 (0.0124)
run3963	-0.25	-0.13	0.0778 (0.0001)	-0.0126 (0.0153)	0.2858 (0.0199)	0.0193 (0.02)	0.4901 (0.021)
run3965	-0.251	-0.364	0.0366 (0.0002)	-0.0159 (0.0312)	0.7652 (0.0232)	-0.002 (0.0549)	0.4662 (0.0533)
run3969	-0.251	-0.364	0.035 (0.0001)	-0.0052 (0.0246)	0.7412 (0.0196)	-0.0205 (0.0284)	0.5201 (0.0285)
run3971	-0.251	-0.364	0.0336 (0.0001)	0.0386 (0.0315)	0.7768 (0.0148)	-0.0176 (0.0362)	0.4842 (0.0362)
run3973	-0.251	-0.364	0.0328 (0.0001)	-0.0375 (0.0258)	0.8152 (0.0225)	0.0087 (0.0564)	0.5018 (0.0565)

continued on following page

Table 6.1 continued

Run Name	x-mic	y-mic	z_p	β_{120}	γ_{120}	β_{18}	γ_{18}
run3975	-0.251	-0.364	0.0492 (0.0001)	0.0074 (0.0155)	0.6975 (0.0102)	-0.0059 (0.0256)	0.4694 (0.0304)
run3978	-0.251	-0.364	1.9775 (0.0054)	0.0043 (0.0031)	-0.0064 (0.002)	-0.0069 (0.0053)	0.088 (0.005)
run3980	-0.251	-0.364	0.1971 (0.0002)	0.0072 (0.0071)	0.2752 (0.0042)	-0.0065 (0.0066)	0.4295 (0.0066)
run3982	-0.251	-0.364	0.0418 (0.0001)	-0.0166 (0.018)	0.7224 (0.0123)	0.0429 (0.0278)	0.5405 (0.0277)
run3985	-0.251	-0.364	0.0343 (0.0001)	-0.0161 (0.0215)	0.7663 (0.0169)	-0.0137 (0.0265)	0.5271 (0.0251)
run3987	-0.251	-0.364	0.0341 (0.0001)	-0.0266 (0.0216)	0.7746 (0.0175)	0.0429 (0.027)	0.54 (0.0303)
run3988	-0.251	-0.364	0.0595 (0.0001)	-0.0051 (0.0168)	0.6587 (0.0105)	0.0161 (0.0152)	0.5174 (0.0157)
run3992	-0.251	-0.364	0.0869 (0.0001)	-0.0029 (0.0149)	0.559 (0.0096)	-0.0029 (0.0098)	0.4847 (0.0096)
run3994	-0.25	-0.364	0.1315 (0.0001)	0.0117 (0.0082)	0.4202 (0.0076)	0.0126 (0.0074)	0.4792 (0.0081)
run3996	-0.251	-0.364	0.1836 (0.0002)	0.0071 (0.0069)	0.3157 (0.0053)	-0.0005 (0.0069)	0.4603 (0.0071)
run3998	-0.251	-0.364	0.054 (0.0001)	0.0031 (0.0166)	0.6911 (0.0106)	-0.0198 (0.0152)	0.5263 (0.0176)
run4001	-0.251	-0.364	0.0335 (0.0001)	0.0275 (0.0256)	0.778 (0.0174)	0.0271 (0.0329)	0.5004 (0.031)
run4006	-0.251	-0.364	0.0385 (0.0001)	-0.0418 (0.0251)	0.7664 (0.025)	-0.1269 (0.098)	0.5564 (0.097)
run4008	-0.251	-0.364	0.4551 (0.0004)	0.0009 (0.0028)	0.0557 (0.0026)	0.0036 (0.0061)	0.3283 (0.0066)
run4010	-0.251	-0.364	0.2787 (0.0003)	0.0097 (0.0059)	0.17 (0.0041)	0.0115 (0.0069)	0.4121 (0.0076)
run4012	-0.251	-0.364	0.9815 (0.0014)	-0.001 (0.0032)	0.0027 (0.0029)	0.0168 (0.007)	0.2137 (0.0071)
run4014	-0.251	-0.364	0.0419 (0.0002)	0.0013 (0.0197)	0.7562 (0.0122)	-0.0356 (0.0236)	0.5064 (0.0252)
run4015	-0.251	-0.364	0.0417 (0.0001)	-0.0165 (0.0342)	0.7443 (0.0242)	0.0173 (0.0374)	0.4951 (0.037)
run4016	-0.251	-0.364	0.0417 (0.0001)	-0.0167 (0.0258)	0.7641 (0.0189)	-0.0056 (0.0236)	0.4926 (0.0231)
run4018	-0.251	-0.364	0.1041 (0.0002)	0.0036 (0.0114)	0.4976 (0.0063)	-0.0004 (0.0077)	0.4777 (0.0084)
run4021	-0.251	-0.364	0.0708 (0.0001)	0.0045 (0.0174)	0.6157 (0.011)	-0.0112 (0.0138)	0.5127 (0.0135)

continued on following page

Table 6.1 continued

Run Name	x-mic	y-mic	z_p	β_{120}	γ_{120}	β_{18}	γ_{18}
run4025	-0.251	-0.364	0.3798 (0.0003)	0.0023 (0.0029)	0.0892 (0.0032)	0.0038 (0.0067)	0.3694 (0.0071)
run4027	-0.251	-0.364	0.7134 (0.0008)	-0.0003 (0.0032)	0.0173 (0.0029)	0.0039 (0.0049)	0.2691 (0.0053)
run4029	-0.251	-0.364	0.0333 (0.0001)	0.0103 (0.0261)	0.7753 (0.0164)	-0.0252 (0.0247)	0.5199 (0.0245)
run4030	-0.251	-0.364	0.0334 (0.0001)	0.0147 (0.0268)	0.7865 (0.0167)	0.0053 (0.0275)	0.5183 (0.0238)
run4033	-0.251	-0.364	0.0322 (0.0001)	-0.0059 (0.0199)	0.7736 (0.0129)	0.0664 (0.0454)	0.5303 (0.0387)
run4035	-0.251	-0.364	0.034 (0.0002)	0.0023 (0.0292)	0.781 (0.0249)	-0.0648 (0.0415)	0.556 (0.0444)
run4037	-0.251	-0.364	0.1559 (0.0001)	0.0029 (0.0084)	0.3579 (0.0056)	-0.0114 (0.0092)	0.4488 (0.0084)
run4039	-0.251	-0.364	0.0444 (0.0002)	0.0191 (0.0175)	0.7337 (0.0131)	-0.0409 (0.0266)	0.5315 (0.0284)
run4041	-0.251	-0.364	0.0422 (0.0007)	-0.0043 (0.0254)	0.7474 (0.0145)	-0.0109 (0.029)	0.5623 (0.0291)
run4043	-0.251	-0.364	0.0362 (0.0001)	0.007 (0.0243)	0.7771 (0.0169)	-0.1151 (0.0926)	0.4862 (0.0893)
run4044	-0.251	-0.364	0.0362 (0.0002)	-0.0161 (0.0183)	0.7623 (0.0163)	-0.0796 (0.079)	0.6337 (0.0831)
run4047	-0.251	-0.364	0.0394 (0.0003)	-0.0082 (0.0193)	0.7729 (0.0122)	-0.0743 (0.0477)	0.5465 (0.0509)
run4049	-0.251	-0.364	0.0393 (0.0003)	-0.01 (0.0172)	0.7504 (0.0127)	-0.0206 (0.0279)	0.5003 (0.028)
run4051	-0.251	-0.364	0.035 (0.0002)	-0.0146 (0.0162)	0.7544 (0.0163)	-0.0458 (0.0398)	0.5801 (0.0413)
run4053	-0.251	-0.364	0.0339 (0.0003)	0.0043 (0.0174)	0.8008 (0.0168)	-0.0269 (0.0487)	0.5108 (0.0483)
run4055	-0.251	-0.364	0.0336 (0.0002)	-0.0277 (0.0186)	0.7545 (0.0189)	-0.0865 (0.0674)	0.6283 (0.0699)
run4057	-0.251	-0.364	0.0333 (0.0003)	0.0104 (0.0292)	0.7814 (0.0264)	0.3902 (0.1779)	0.7542 (0.1934)

6.3.2 Calibration data collection

1. Removed all attractor connections from vacuum can and installed calibration turntable.
2. Moved pendulum far from screen where noise performance was good ($z_p \approx 2$ mm).
3. Started calibration turntable rotating. The turntable period was set at $2.5\tau_0$ to place the $3\omega_{\rm cal}$ signal near the 120ω frequency (a speed of $2\tau_0$ would have set it closer to the 120ω frequency, but the turntable was not capable of running at that speed).
4. Roughly centered the table on the pendulum in xy. An additional 2 spheres were placed on the turntable to aid with centering (discussed in Section 6.4.1).
5. Moved xy-centered calibration turntable in z.
6. Took full day data run.
7. Repeated steps 5-6 to adequately map torque function $N_{\rm cal}(z)$.
8. Took sweep run. Only one sweep run was necessary as the pendulum never moved.

Table 6.2 lists all *calibration runs* with their turntables positions and measured $3\omega_{\rm cal}$ and $4\omega_{\rm cal}$ twist amplitudes. Analysis of the calibration data is found in Section 6.4.

Table 6.2: Turntable positions and measured twists of the calibration data set. The position units are in mm and twist units are in μrad. A value in parentheses is the uncertainty for the value to the immediate left. Runs 4069-4074 were used only for centering.

Run Name	x-cal	y-cal	z-cal	β_3	γ_3	β_4	γ_4
run4069	0	0	0			-0.0095 (0.0016)	0.0109 (0.0015)
run4070	1.97	0	0			0.0079 (0.0012)	0.0131 (0.0013)
run4071	-2	0	0			-0.0206 (0.0009)	0.0117 (0.0011)
run4072	0	1.98	0			-0.01 (0.0011)	0.0287 (0.001)
run4073	0	1.01	0			-0.0037 (0.0012)	0.0192 (0.0012)
run4074	0	-1.98	0			-0.0045 (0.0009)	-0.0035 (0.0009)
run4075	0.48	-1.5	0	0.9489 (0.0012)	-0.5422 (0.001)	0.0005 (0.0012)	-0.0003 (0.0009)
run4076	0.48	-1.5	-5	0.9953 (0.0011)	-0.5402 (0.0009)	-0.0002 (0.001)	0.0013 (0.0012)
run4077	0.48	-1.5	-10	1.0262 (0.001)	-0.5565 (0.0009)	-0.0008 (0.0011)	0.0023 (0.001)
run4078	0.48	-1.5	-20	1.0711 (0.0014)	-0.5605 (0.0013)	0 (0.001)	-0.0002 (0.001)
run4079	0.48	-1.5	-30	1.0684 (0.0008)	-0.5826 (0.0009)	0.0004 (0.0008)	-0.0003 (0.001)
run4080	0.48	-1.5	-40	1.0469 (0.0011)	-0.5593 (0.001)	-0.0003 (0.0015)	-0.0004 (0.0015)
run4081	0.48	-1.5	-50	0.9927 (0.0011)	-0.5268 (0.001)	0.0009 (0.001)	-0.0025 (0.001)
run4082	0.48	-1.5	-55	0.9445 (0.0012)	-0.531 (0.0013)	0.0003 (0.0013)	0.0006 (0.001)
run4083	0.48	-1.5	-27	1.0635 (0.001)	-0.5934 (0.0009)	0.0012 (0.0011)	0.0008 (0.0008)

6.4 Torque Scale Calibration

The torsional spring constant, κ, defines the conversion of twist amplitude to torque amplitude

$$N = \kappa\theta \ , \tag{6.8}$$

and also relates the free-torsion period of the pendulum to its moment of inertia

$$\kappa = \frac{(2\pi)^2 \ I_p}{\tau_0^2} \ . \tag{6.9}$$

In addition to describing the intrinsic properties of the torsion fiber, κ also encompasses restoring forces on the pendulum due to local electrostatic, magnetic, or gravitational potential wells. The potential wells are known to vary with pendulum location (both in z and xy), so the value of κ, and hence τ_0, can change from run to run.

Our experiment was designed to have a continuous calibration signal to account for these changes in κ. With this method of calibration, the torque signal for each run is determined by

$$N_\omega^i = \theta_\omega^i \ \frac{N_{\rm cal}}{\theta_{\rm cal}^i} \ , \tag{6.10}$$

where $N_{\rm cal}$ is the calculated calibration torque and θ_ω^i and $\theta_{\rm cal}^i$ are the measured signal and calibration twist amplitudes of the ith data run. Problems arose during data set W1, however, when the many cables running to the bottom of the vacuum can interfered with the operation of the calibration turntable, making measurements unreliable. Therefore, we chose to change our calibration method for data sets W2 and W3. We collected a stand-alone calibration data set where all systems running the attractor were unplugged and no longer an interference. From this data we extracted a measurement of the pendulum's moment of inertia about the twist axis, I_p, with which to calibrate our short-range twist data. With this method of calibration, the torque signal for each run is

$$N_\omega^i = \theta_\omega^i \ \frac{(2\pi)^2 \ I_p}{\tau_0^{i2}} \ , \tag{6.11}$$

where τ_0^i is extracted from the *sweep run* immediately after the *data run*. Because the fiber attachment and pendulum level were unchanged between sets W2, W3, and the calibration set, we believe it is reasonable to assume I_p remained constant for all these sets.

6.4.1 Calibration Data

The calibration signal came from three 2.5" diameter brass balls on a rotating turntable outside the vacuum can gravitationally pulling on three 0.25" diameter aluminum balls located near the top of the pendulum. This interaction created a $3\omega_{\rm cal}$ twist signal on the pendulum that we measured at various $z_{\rm cal}$ heights of the turntable, while leaving the pendulum stationary (Figure 6.8). The procedure we used for centering the turntable on the pendulum is discussed in the next section.

The calibration torques were not the only data constraining our determination of I_p. Similar to our strategy with fitting the short-range data, the adjustable parameters that fit the calibration torques were independently measured, when possible, and served as data points (Table 6.3). An additional data point we used was the free-torsion period of the pendulum with and without balls. The period of the pendulum with balls was $\tau_0 = 301.65 \pm 0.12$ sec., and removing the balls resulted in a period of $\tilde{\tau}_0 = 295.40 \pm 0.02$ sec.

Calibration Centering

We centered the turntable on the pendulum in the same manner described in [9]. Two additional 2" diameter brass balls were placed on the turntable and the Q_{44} gravitational moment of the balls coupled to the q_{44} moment of the off-center pendulum balls. This interaction scaled linearly with the xy-offset of the pendulum, vanishing when the pendulum balls were centered on the rotation axis of the turntable, and was a much more sensitive measure of center than monitoring the change in the $3\omega_{\rm cal}$ signal. Figure 6.7 shows the measured $4\omega_{\rm cal}$ signals for the centering runs as well as the calibration runs that were nominally on-center.

The average $4\omega_{\rm cal}$ amplitude of all calibration runs taken after centering was 0.31 ± 0.35 nrad. This would correspond to a centering misalignment of 35 ± 40 μm given the observed change in twist amplitude per change in xy-offset of 8.7 nrad/mm. However, the pendulum body also had a q_{44} moment (that was small by design, though nonzero) that when coupled to the Q_{44} of the brass balls should account for ≈ 1.7 nrad of twist. The systematic test with pendulum balls removed (Section 7.2.1) provided a direct measure of the

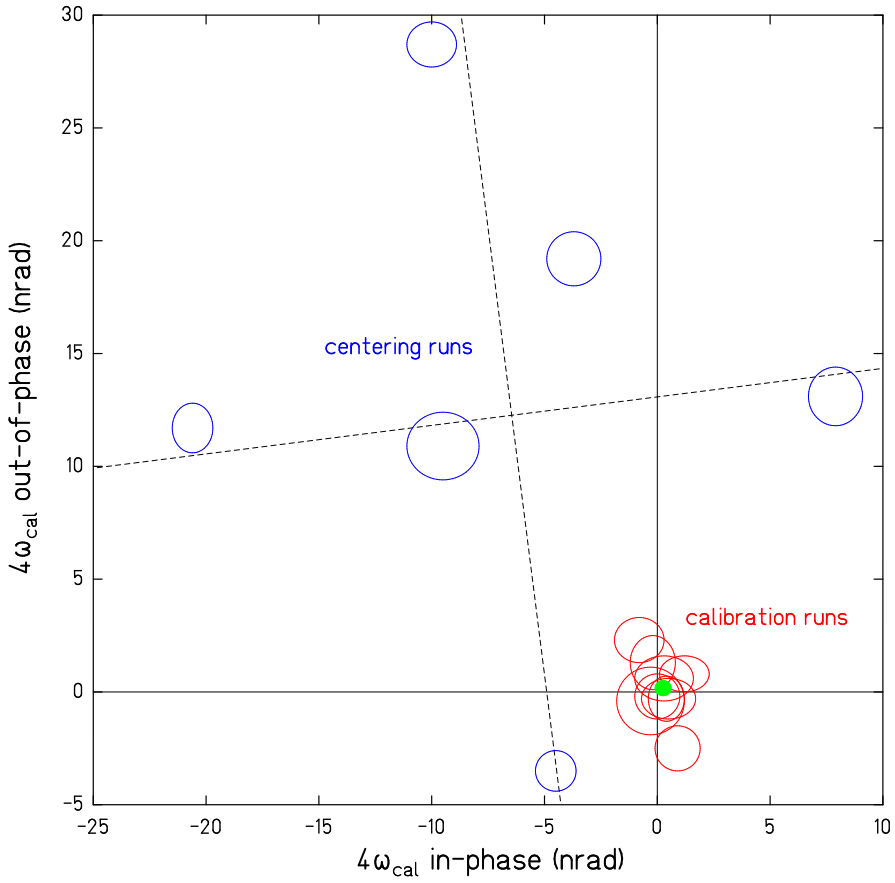

Figure 6.7: Data showing the centering of the calibration turntable on the pendulum using the $4\omega_{\rm cal}$ torque signal. The dashed lines indicate the axes of torque variation as $x_{\rm cal}$ or $y_{\rm cal}$ were modulated by up to ± 2 mm. The calibration runs were all taken with the turntable at a fixed $(x_{\rm cal}, y_{\rm cal})$ location. The green dot indicates the average value of all calibration runs.

$4\omega_{\rm cal}$ signal attributable to the pendulum body and was in agreement with the calculation at 1.3 ± 0.8 nrad. Using these measured values leads to an overall centering misalignment of 150 ± 70 μm.

As mentioned, the $3\omega_{\rm cal}$ signal is fairly insensitive to xy-offsets. A 220 μm misalignment only produces a $3{\times}10^{-6}$ relative change to the calibration signal. The noise-to-signal of the most resolved *calibration run* was $7{\times}10^{-4}$, so the centering misalignment was negligible.

6.4.2 Calibration Model

The calibration model provided the expected twist of the pendulum at $3\omega_{\rm cal}$ as well as the expected change in the free-torsion period from removing the pendulum's balls. Both calculations treated the balls as perfect spheres. The adjustable parameters of the model were

- r_1, r_2 : The average distance from the pendulum's twist axis for the pendulum balls (r_1) and for the turntable balls (r_2).
- m_1, m_2 : The average mass of a single ball for the pendulum balls (m_1) and for the turntable balls (m_2).
- τ_0 : The free-torsion period of the pendulum with balls.
- z_0 : The z-height in turntable indicator units where the centers of the turntable balls and pendulum balls are co-planar.
- θ_0 : Systematic parameter accounting for extraneous turntable-to-pendulum gravitational couplings at 3ω (Section 7.2.1).
- $\hat{I}_p$: The moment of inertia of the pendulum about its twist axis, calculated from the design drawings and measured masses of all parts. Adjusting this parameter accounts for dimensional variations from machining and misalignments during construction.

The 3ω twist amplitude as a function of the adjustable parameters was

$$\begin{aligned}\theta_3(z_{\rm cal}) &= \frac{N_3(z_{\rm cal})}{\kappa} + \theta_0 \\ &= \frac{m_1\ m_2\ \tau_0^2}{I_p\ (2\pi)^2}\ \hat{N}_3(r_1, r_2, z_{\rm cal} - z_0) + \theta_0 \end{aligned} \tag{6.12}$$

$$I_p = \hat{I}_p - I_b(\hat{m}_1, \hat{r}_1) + I_b(m_1, r_1) \tag{6.13}$$

$$I_b(m, r) = 3m(r^2 + \frac{2}{5}\ R^2)\ , \tag{6.14}$$

where $\hat{N}_3(r_1, r_2, z)$ is the predicted torque for co-axial pendulum and turntable point-mass arrays of unit mass. I_p adjusts with r_1 and m_1 by subtracting the pre-calculated moment of the balls from the pre-calculated moment of the pendulum and adding back the moment of the balls with the adjustable values. R is the spherical radius of the pendulum balls.

The free-torsion period of the pendulum with the balls removed was calculated as

$$\tilde{\tau}_0 = \tau_0\ \sqrt{\frac{\tilde{I}_p}{I_p}} \tag{6.15}$$

$$\tilde{I}_p = \hat{I}_p - I_b(\hat{m}_1, \hat{r}_1)\ . \tag{6.16}$$

This assumes κ remained constant when removing the spheres from the pendulum (the change of stress on the fiber likely effected κ by some very small amount).

6.4.3 Calibration Fit

The calibration model fit the calibration data, the independently measured adjustable parameter values, and the ball-less pendulum period very well. Figure 6.8 and Table 6.3 show the results of the fit. From this fit, the true value for the moment of inertia of the pendulum about the twist axis was determined to be $I_p = 73.39 \pm 0.32$ g cm^2. We used this central value, along with the τ_0^i measurements from each *sweep run*, to convert the *data run* twist measurements into torque units. The error bar was folded into the multiplicative systematic error budget for both the 18ω and 120ω signals (Section 7.2.8).

6.5 Run Analysis

Each *data run* recorded a digital time series of the difference and sum outputs, Δ and Σ, of the autocollimator. To extract the driving torques, the raw data was passed through the

Table 6.3: Measured and fitted values of calibration parameters. All measured values helped constrain the fits (unless noted). The parameters of the upper box were adjustable in the fit, and the parameters in the lower box were calculated using fitted values of the adjustable parameters.

Parameter	Measured	Fitted	Units
r_1	1.651 ± 0.0025	1.651 ± .0024	cm
r_2	15.24 ± 0.006	15.240 ± .005	cm
$3 \times m_1$	1.0852 ± 0.0002	1.0852 ± 0.0002	g
$3 \times m_2$	3410.535 ± 0.005	3410.55 ± 0.005	g
τ_0	301.65 ± 0.12	301.63 ± 0.02	sec
z_0		-2.693 ± 0.008	cm
θ_0	0 ± 0.0016	0.0003 ± 0.0016	μrad
$\hat{I}_p$	72.702 *	73.386 ± 0.315	g cm^2
$\tilde{\tau}_0$	295.40 ± 0.02	295.40 ± 0.07	sec
I_p		73.386 ± 0.324	g cm^2

* calculated value – does not constrain parameter

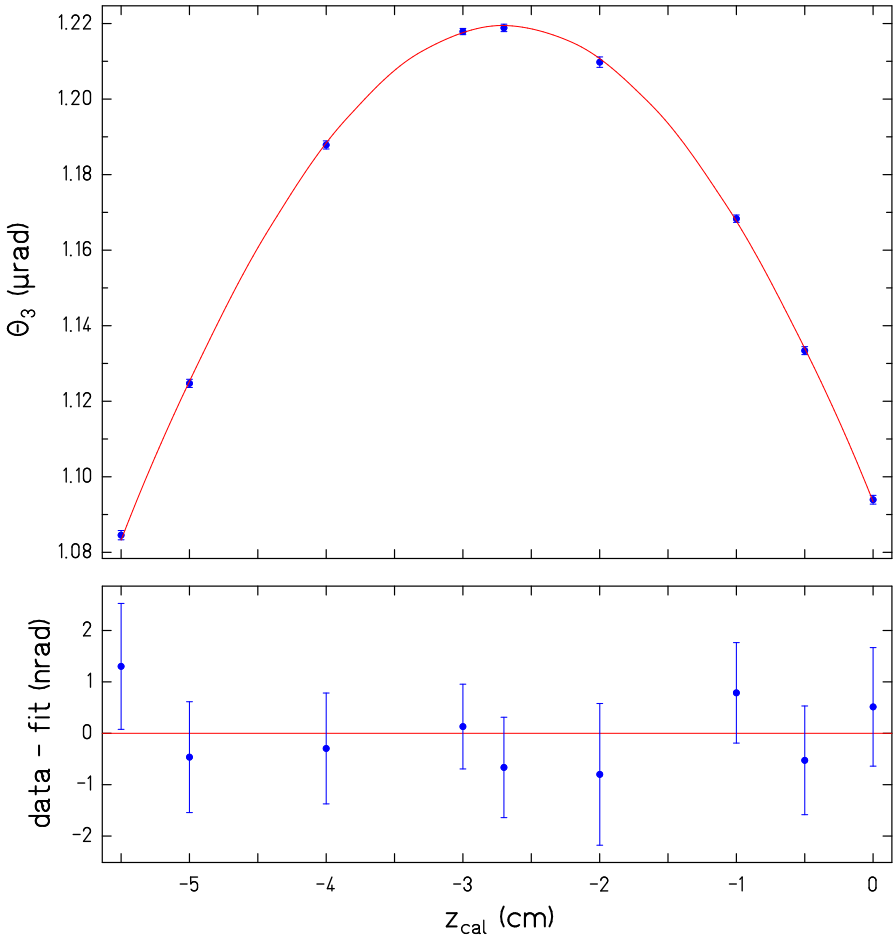

Figure 6.8: Fitted $3\omega_{\mathrm{cal}}$ calibration data.

following analysis pipeline:

1. Created linearized $\theta(t)$ from $\mathcal{O}\left((\Delta/\Sigma)^4\right)$ polynomial provided by *sweep run*
2. Removed free torsion oscillations with 4pt filter, $\hat{\theta}_4(t)$
3. Cut data into 60° sections of attractor rotation
4. Fit 60° $\hat{\theta}_4(t)$ cuts with 18ω and 120ω harmonic amplitudes and a linear background
5. Removed cuts whose χ^2 fit residuals were anomalously large with respect to the distribution of the remaining cuts
6. Averaged harmonic amplitudes of remaining cuts, inferring uncertainties from scatter in fits
7. Scaled average harmonic amplitudes by attenuation factors that accounted for pendulum inertia, torsion filter response, and electronic time constants
8. Converted harmonic amplitudes to torque by multiplying them by $\kappa = I_p(2\pi/\tau_0)^2$

Many of these steps have been well discussed in previous publications [10][9]. The following sections discuss the aspects of this analysis that were new to this measurement.

6.5.1 Nonlinear Corrections

Following each *data run* was a *sweep run* that used the assumed linearity of the pendulum's un-driven oscillations to correct nonlinearities in the autocollimator. The nonlinearities were accounted for by defining $\theta(t)$ with an $\mathcal{O}\left((\Delta/\Sigma)^4\right)$ polynomial. Determining the coefficients, c_i, that linearize θ was discussed in [9].

While fitting the sweep runs removed nonlinearity, the fitting procedure did not constrain the c_i coefficients to respect the angle calibration of the autocollimator. For data with a continuous torque calibration signal, this sloppiness in angle calibration was inconsequential as it effected data and calibration signals equally. However, the torque calibration was not continuously present for data set W3 (as well as W2), so it was important to ensure a (nominally) consistent angle calibration for all *data* and *calibration runs*. This was done by rescaling the c_i coefficients such that the $(\Delta/\Sigma)^1$ coefficient (c_0 in the language of [9]) remained a consistent value.

This procedure did not completely remove angle calibration uncertainty as the variable c_i coefficients ($i > 0$) necessarily changed the effective angle calibrations at some level. These changes may, or may not, have reflected actual changes in the calibration of the optics (curvature of the pendulum's mirror could possibly change the angle calibration for different z_p heights). To gauge the possible effect these uncertainties might have had on our data, the rescaled c_i coefficients for all W3 data were applied to idealized, perfectly sinusoidal fake data, which had a driving torque and free-torsion amplitudes equal to those observed in the W3 data. These data were then fit to see the error in the deduced driving torque created by the nonlinearities. The fits were statistically consistent with the known driving torque and had a standard deviation of $\approx 0.1\%$. This was comparable to the uncertainty in the free-torsion periods ($\approx 300 \pm 0.1$ sec) used to convert angle to torque (Section 6.4). Moreover, the fit errors did not exhibit any correlation with z_p. Therefore, the lack of continuous calibration, and the associated uncertainty in angle calibration, was not a significant contributor to the overall experimental uncertainty.

6.5.2 Torsion Filter

We filtered $\theta(t)$ with an ω_0-notch filter to lessen the impact of free-torsion amplitude changes on the fit quality. The filtering translated a shift in free-torsion amplitude to a noise spike at a given time. In other words, a non-filtered noise event diverted all points from the best fit curve, while a filtered noise event diverted only a few points from the best fit curve.

Filtering also lessened the impact of a drifting equilibrium position, $\theta_0(t)$, on the fit quality. Drift, modeled with high order polynomial terms, was not necessarily orthogonal to the harmonic torques and could therefore pollute the harmonic fits. The original Eöt-Wash short-range experiment [10] used the 2pt filter which did not suppress drift. We have since developed filters that do (Figure 6.9). The 5pt filter, used for the 2006 Eöt-Wash experiment [6], aggressively suppressed drift by effectively taking the second derivative of $\theta_0(t)$. With this filter, the first nonzero polynomial term of the filtered data was proportional to the 2nd order term in the non-filtered data, and so on. The 4pt filter, utilized in this work, suppressed drift like the first derivative of $\theta_0(t)$ and was better suited for simultaneous

analysis of the 18ω and 120ω signals (discussed in detail below).

The definition of the 5pt filter and the response of twist amplitudes was

$$\hat{\theta}_5(t) = \frac{1}{2}\left(\theta(t) + \theta(t+\frac{\tau_0}{3}) + \theta(t-\frac{\tau_0}{3}) - \frac{3}{2}\left(\theta(t+\frac{\tau_0}{4}) + \theta(t-\frac{\tau_0}{4})\right)\right) \tag{6.17}$$

$$\hat{R}_5(\omega) = \frac{1}{2}\left(1 + 2\cos(\omega\frac{2\tau_0}{6}) - 3\cos(\omega\frac{\tau_0}{4})\right). \tag{6.18}$$

The definition of the 4pt filter and the response of twist amplitudes was

$$\hat{\theta}_4(t) = \theta(t+\frac{\tau_0}{8}) - \theta(t-\frac{\tau_0}{8}) + \theta(t-\frac{3\tau_0}{8}) - \theta(t+\frac{3\tau_0}{8}) \tag{6.19}$$

$$\hat{R}_4(\omega) = -2\left(\sin(\omega\frac{\tau_0}{8}) - \sin(\omega\frac{3\tau_0}{8})\right). \tag{6.20}$$

6.5.3 5pt vs 4pt filter

The 5pt and 4pt filters gave significantly different results for the size of the 18ω error bars and for the magnitude of the 120ω amplitudes. To determine which filter was providing more accurate results, we developed a dynamic computer model of the pendulum's twist with which we could fake data and study our analysis pipeline. The model calculated the pendulum's response, according to the equation of motion for an internally damped harmonic oscillator, to sinusoidal driving torques, 1/f noise, and polynomial drift applied to the equilibrium position at each time step. We simulated 200 noisy data runs with a fixed driving amplitude and looked at the statistics of the final harmonic amplitudes after running these data through the analysis pipeline. As Figure 6.10 illustrates, our model faithfully reproduced both trends observed in the data and showed that the 4pt, 120ω amplitudes were too small and the 5pt, 18ω error bars were too large.

The 4pt suppression of the 120ω amplitudes is understood by our choice of data point spacing. We collected 60 data points per free-torsion oscillation. This spacing is commensurate with the 5pt filter which samples points at $\tau_0/3$ and $\tau_0/4$ (and is why that spacing was originally chosen), but is not commensurate with the 4pt filter samples at $\tau_0/8$ and $3\tau_0/8$. The suppressed 4pt, 120ω amplitudes are the result of estimation error from the linear interpolation between sample points. This suppression goes away when commensurate

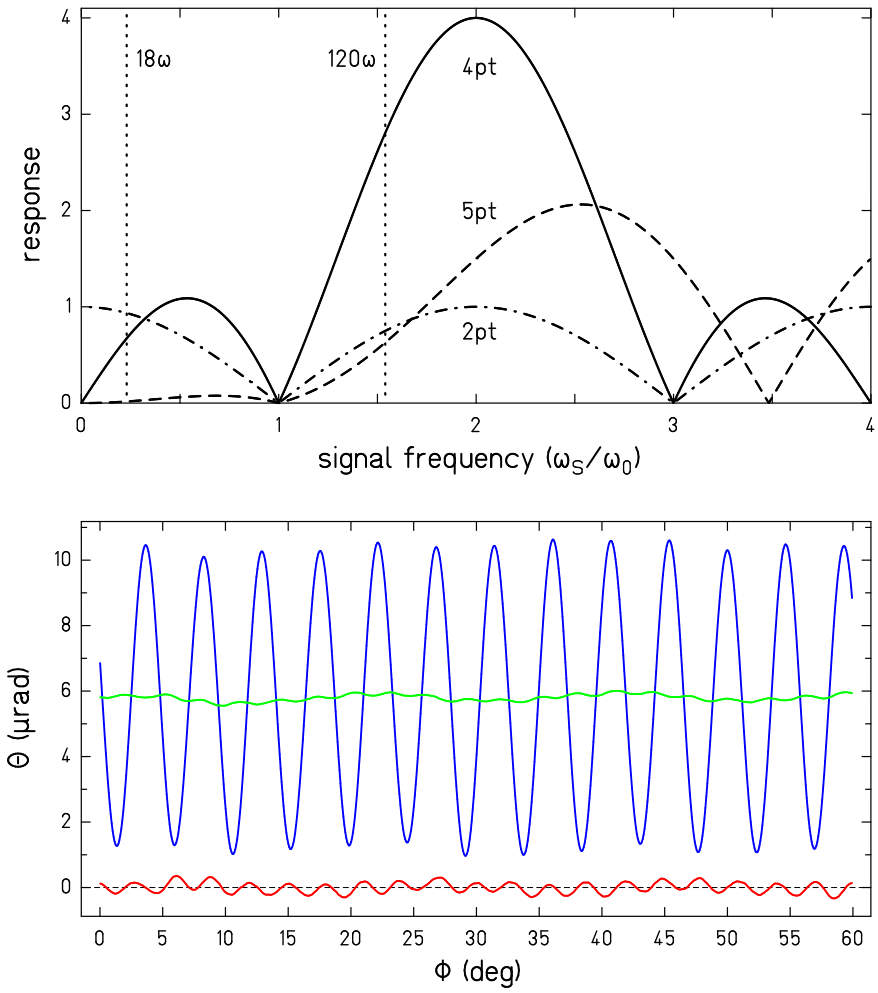

Figure 6.9: Response of notch filters. TOP: Behavior of the 2pt, 4pt, and 5pt filters as a function of signal frequency. By design, all filters remove ω_0 from $\theta(t)$. BOTTOM: A 60° cut of raw data (blue) filtered with the 2pt (green) and 4pt (red) notch filters. The 4pt filter, which has a notch at $\omega_s = 0$, behaves like a single derivative on drifts, e.g. the average offset from 0 μrad in the 4pt filtered data is proportional to linear drift in the raw data. The ratio of the 120ω to 18ω signals is 5 times larger for the 4pt filter than the 2pt filter.

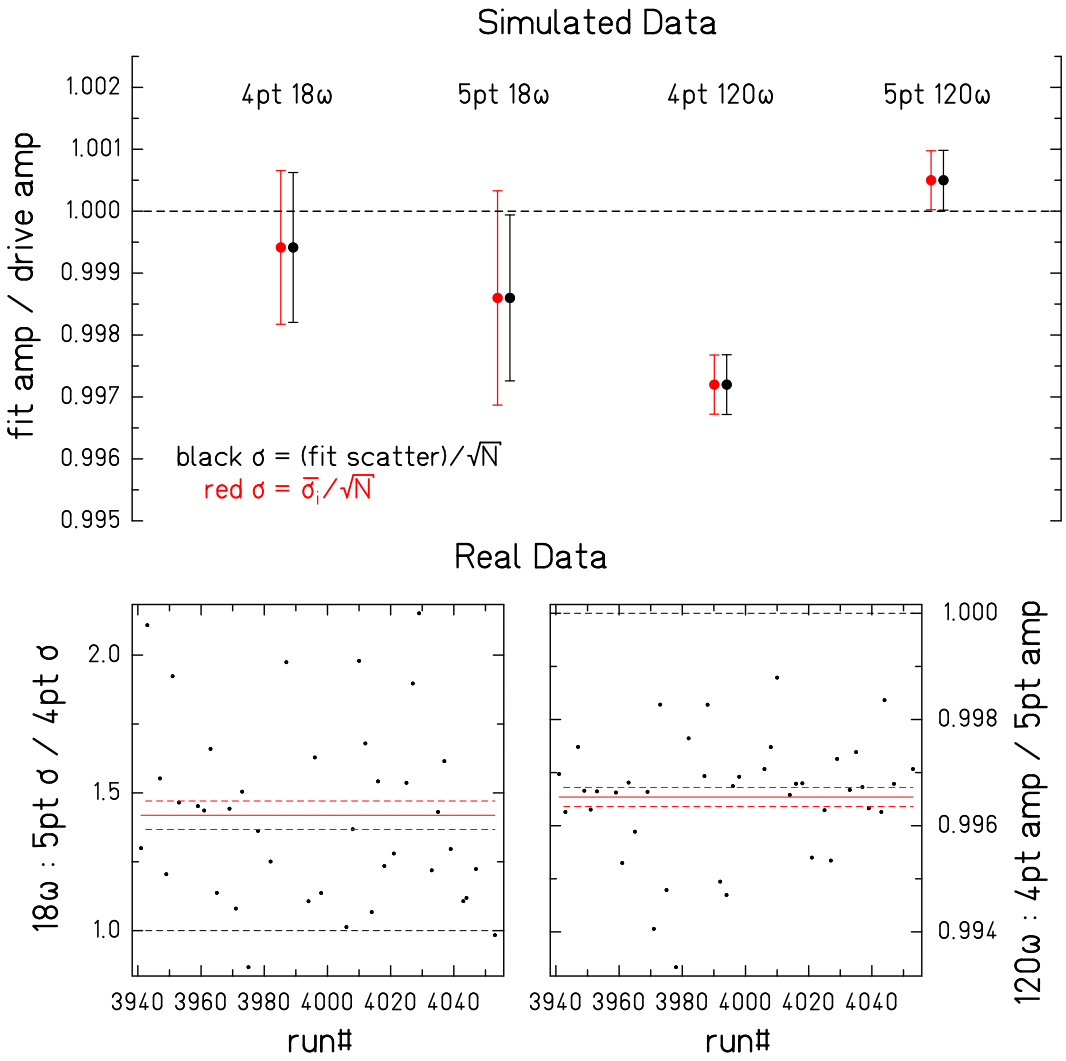

Figure 6.10: Comparison of 4pt and 5pt filters in simulated and real data. TOP: Statistical summary of 200 simulated data runs analyzed with the 5pt and 4pt filters. The red error bars are proportional to the average error extracted from a single run; ideally they should equal the black error bars which represent actual scatter of the data runs. For the 5pt, 18ω data, the error bars extracted from single runs were clearly too large ($\chi^2/DOF = 0.6$). Also, the 4pt, 120ω amplitudes were clearly too small. BOTTOM: The W3 data set exhibits the same relations, with the ratio of 18ω 5pt to 4pt error bars > 1 (left), and the ratio of 120ω 4pt to 5pt amplitudes < 1 (right).

points are chosen for the 4pt filter (e.g. 64 samples per τ_0) or a higher order interpolation method is used to filter the data.

The increased 18ω error bars of the 5pt filter are less well understood. They are thought to be related to the 18ω frequency being well below ω_0 and the high degree of drift suppression present in that filter.

Because the observed problem with the 4pt filter is better understood, we chose to analyze all data with the 4pt filter and correct the 120ω suppression by scaling the 120ω model by $\gamma_{120} = 0.997$. (Implementing a higher-order interpolation in the filter would have fixed this problem without scaling, but this has not yet been incorporated into our analysis software.)

Chapter 7

STATISTICAL AND SYSTEMATIC UNCERTAINTIES

7.1 Understanding Statistical Noise

The fluctuation-dissipation theorem states that any mechanism that dissipates energy from a system also introduces noise to the system. The two common descriptions of dissipative noise relevant to torsion balances are internal damping and velocity damping[11]. We also identified a noise contribution for this experiment that arose from the combination of seismic pendulum excitations and the electrostatic patch-fields.

7.1.1 Internal Damping

When considering frictional losses within a twisting torsion fiber the equation of motion is

$$I\ddot{\Theta} + \kappa(1 + \frac{i}{Q})\Theta = 0 \ , \tag{7.1}$$

giving rise to a power spectral density (thermal noise limit) that looks like

$$\Theta^2(\omega) = \left(\frac{4k_bT}{\kappa Q\omega}\right)\left[\frac{1}{(1-\omega^2/\omega_0^2)^2 + \frac{1}{Q^2}}\right], \tag{7.2}$$

where I is the rotational inertia of the pendulum, κ is the torsional spring constant, Q is the quality factor of the fiber, k_b is Boltzmann's constant, T is the absolute temperature, and ω_0 is the free-resonant frequency of the pendulum. The quantity in parentheses represents the torque power spectrum, and the expression in brackets represents the inertial response of the pendulum. Measured noise spectra when the pendulum-screen separation, z_p, is large are consistent with Equation 7.2, though they are also consistent with a velocity damped description (Equation 7.4).

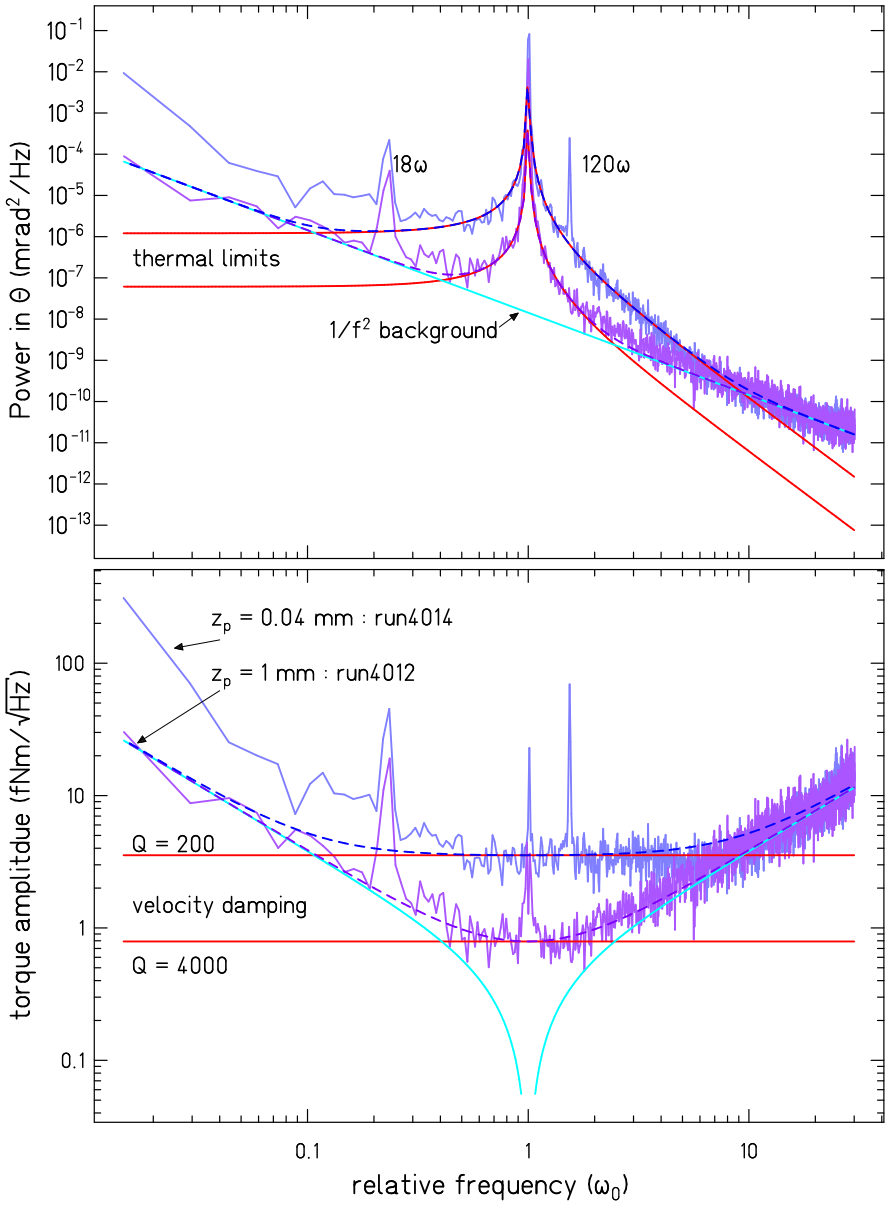

Figure 7.1: Noise spectrum of near and far data runs. TOP: Power spectral density of twist angle. Curves for velocity damped thermal limits with Qs of 200 and 4000 are shown. The apparent $1/f^2$ background was likely due to temperature drifts of the apparatus and autocollimator noise. Dashed curves are the quadrature sum of the thermal and $1/f^2$ lines. BOTTOM: Torque amplitude spectral density, which is the data from upper plot divided by the inertial response of the pendulum. We attempted to place the 120ω signal near the torque noise minimum while maintaining good separation from the free torsion frequency. The $z_p = 0.04$ mm spectrum indicates we could have run the attractor faster at close separations to improve the noise performance of the 18ω signal without sacrificing the performance of the 120ω signal.

7.1.2 Velocity Damping

Velocity damping, from either residual gas or eddy currents, has an equation of motion

$$I\ddot{\Theta} + \frac{I\omega_0}{Q}\dot{\Theta} + \kappa\Theta = 0 \tag{7.3}$$

and a power spectral density

$$\Theta^2(\omega) = \left(\frac{4k_bT}{\kappa Q\omega_0}\right)\left[\frac{1}{(1-\omega^2/\omega_0^2)^2 + (\frac{\omega/\omega_0}{Q})^2}\right] . \tag{7.4}$$

A significant difference between Equations 7.4 and 7.2 is that the torque noise for velocity damping (square root of term in parentheses) is white, whereas the torque noise for internal damping is pink ($1/\sqrt{\omega}$). Figure 7.1 shows the noise spectra of a near and a far data run. Either internal or velocity damping could reasonably describe the noise floor of the far run, but the near run clearly has a white noise floor which is the signature of velocity damping.

We have long observed that the statistical error bars grow in magnitude as z_p gets small. Figure 7.2 plots the amplitude error bars for all runs in data sets W1, W2, and W3. This increase in noise is likely due to a combination of residual gas trapped between the pendulum and foil (a phenomenon known as squeeze film damping[12]), eddy currents due to free charges on the pendulum or foil, and the seismic patch-field interaction discussed below.

7.1.3 Seismic Patch-field Noise

It has been our assumption that the increase in noise at short separations is in part related to electrostatic patch-fields on the gold-plated pendulum and gold-plated beryllium-copper screen. Keeping our capacitance meter on while collecting data has led to a better understanding of these patch-field interactions.

The patch-fields are present on the screen and pendulum surfaces presumably due to randomized crystal alignment of the gold coatings, surface flaws (scratches, dents, burrs), and contaminations (dust, residues). The interplay of these patch fields has a potential energy minimum that is likely not aligned with the equilibrium angle Θ_0 of the pendulum, so that as z_p gets small and the interaction force increases, the effective equilibrium angle

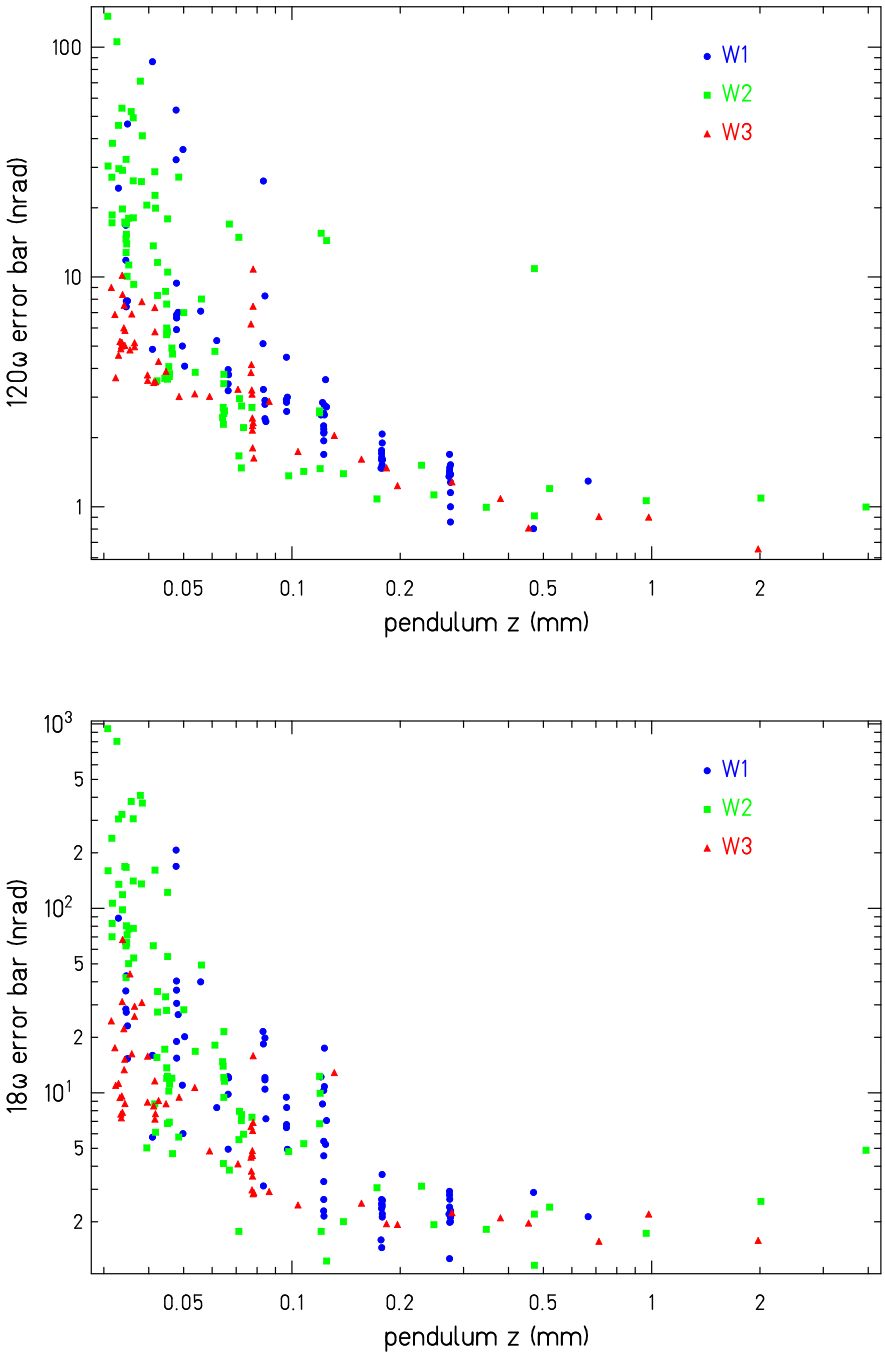

Figure 7.2: Observed amplitude error bars from data sets W1, W2, and W3.

changes. The gradient of this $\Theta_0(z_p)$ function couples the slight z-translations of the non-torsional modes of the pendulum (swing, wobble, bounce) into the torsion mode. According to Equation 6.2, random seismic excitations of the non-torsional modes will result in kicks to Θ_0 such that

$$\delta\Theta_0 = \frac{1}{2}a_z^2\Theta_0{}''(z_p), \tag{7.5}$$

where a_z is the effective amplitude in the z-direction of the excited pendulum. Figure 7.3 illustrates this with excitations of the pendulum's non-torsional modes (as observed by fluctuations in z_p) clearly correlated in time to kicks of Θ. That nearly all Θ-kicks in the 2-pt. filter data are in the same direction (downward in plot) and are roughly proportional in size to the corresponding z_p spike is evidence of noise described by Equation 7.5.

The normalized run errors also exhibit this correlation. Figure 7.4 maps $\Theta_0(z_p)$ as observed post W3 data collection and compares the functional shape to Θ noise in the W3 data set. The characteristic exponential length scale of $\Theta_0(z_p)$ (about 17μm, which is also the length scale of $\Theta_0{}''(z_p)$) is consistent with length scales observed in the errors of both the 120ω and 18ω data.

The value of $\Theta_0{}''(z_p)$ at a given z_p can vary greatly as a function of xy-position, even changing sign (Figures 7.3 and 7.4 exhibit opposite signs of $\Theta_0{}''(z_p)$). After opening the vacuum vessel, changes in screen alignment and shifting dust will also change the patch-field topography. Measuring the gradient $\Theta_0{}'(z_p)$ (which is proportional to $\Theta_0{}''(z_p)$ when $\Theta_0(z_p)$ is a simple exponential) by moving the pendulum a small step in z_p and observing the change in Θ_0 becomes a quick yet powerful tool to predict the noise performance of the pendulum. It was fortuitous that a local minimum of this gradient was found near the pendulum-attractor center alignment for W3. This may explain why the noise performance of W3 was much improved over W1 and W2. We did not make detailed studies of $\Theta_0(z_p)$ before W3, so we have no hard data for comparison.

7.2 False Signals

Spurious twist signals can potentially mimic or hide new short-range physics. There are several possible categories for such torques: gravitational, magnetic, electrostatic, thermal,

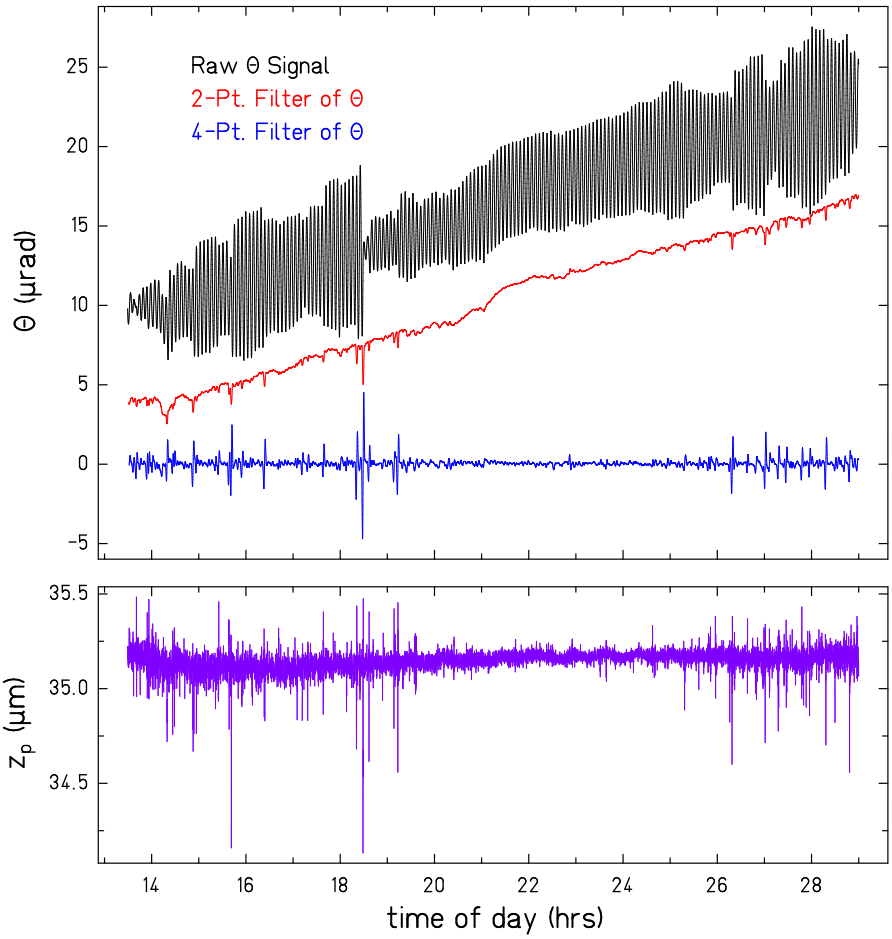

Figure 7.3: Correlations between seismically induced pendulum excitations and Θ noise are observed. Some spikes in the filtered data clearly correspond to spikes in the pendulum-screen separation data, and a quiet period at night is observed in all data. The 2-pt. filter data represent $\Theta_0(t)$ and have been offset from the raw Θ data for clarity. The 4-pt. filter data are proportional to $d\Theta_0/dt$. The z_p data were collected at 0.2 Hz (with sub-sampling near 5 Hz), while the excitation modes of the pendulum fall in the 1-10 Hz band. The attractor was not turning for this data.

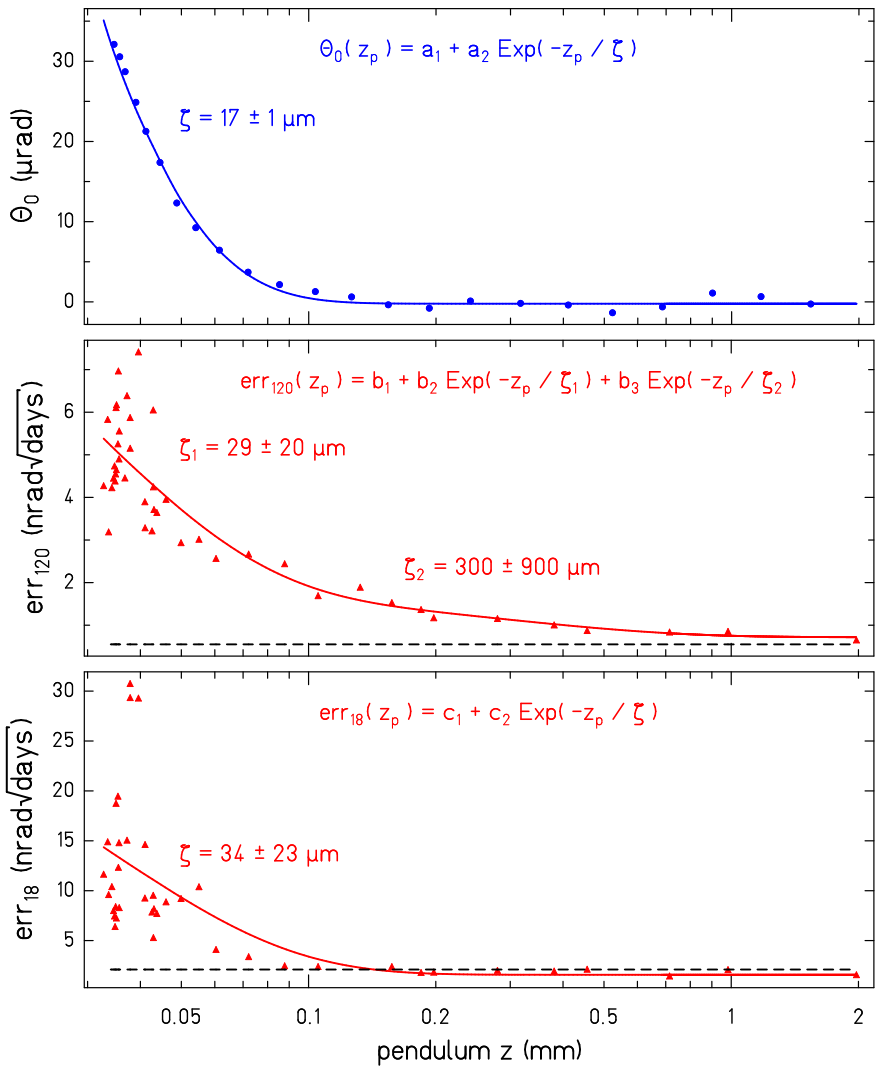

Figure 7.4: The equilibrium position of the pendulum after the W3 data set (top), and the normalized W3 120ω (middle) and 18ω (bottom) run errors as a function of z_p. Θ_0 data have been corrected for tilt feed-through, so changes here are due to patch-field effects. The run errors have been scaled by the square root of the number of cuts in the run to account for varying run lengths. The errors at both frequencies are proportional to $\Theta_0{}''(z_p)$ at the smallest values of z_p, though there appears to be another noise source dominating at intermediate lengths of the 120ω data. All centering runs were removed from run errors, and three clear outliers were removed from the 18ω data.

seismic and mechanical. Each of these are discussed in the following sections.

We exaggerated (when possible) by a factor f_e each identified systematic effect. The general framework for estimating the spurious effects was

$$\vec{a}_s \pm \vec{\sigma}_s = \frac{1}{f_e}(\vec{a}_e \pm \vec{\sigma}_e), \tag{7.6}$$

where $\vec{a}_s$ is our estimate of the spurious twist in the normal data, and $\vec{a}_e$ is the twist contribution of the exaggerated systematic. We calculate the effective uncertainty as

$$\hat{\sigma} = |\vec{a}_s| + |\vec{\sigma}_s|. \tag{7.7}$$

If $\hat{\sigma}$ is of the order of the statistical uncertainty (≈ 1 nrad at 120ω and ≈ 2 nrad at 18ω), then $\vec{a}_s$ is subtracted from all data points while $|\vec{\sigma}_s|$ contributes to the systematic error budget. Otherwise $\hat{\sigma}$ simply adds in quadrature to the systematic error budget.

Section 7.2.8 discusses how the systematic errors are incorporated into the data-fitting.

7.2.1 Gravitational Systematics

Gravitational systematics are unintended interactions of mass distributions at or near the signal frequencies. The rim-protrusion anomaly (Section 5.1.5) is one such systematic; its contribution proved so significant that it had to be incorporated into the 18ω torque model. Our exploration of other possible gravitational couplings is discussed below.

Calibration

All torque measurements were calibrated by the measured $3\omega_{\rm cal}$ interaction between 3 brass balls on a calibration turntable outside the vacuum and 3 aluminum balls near the top of the pendulum. If the pendulum had any residual mass distribution other than the aluminum balls that could couple to the 3 brass spheres, then the calibration could be in error. Similarly, if the calibration turntable had any residual mass distribution other than the brass spheres that could induce a $3\omega_{\rm cal}$ torque on the pendulum, the calibration could be in error.

We took data in two configurations to check for a systematic calibration error: pendulum without spheres but turntable with ($|\vec{a}_{s1}| = 2.92 \pm 0.97$ nrad), and pendulum with spheres

but turntable without ($|\vec{a}_{s2}| = 1.54 \pm 1.12$ nrad). Because these systematics were not exaggerated ($f_e = 1$) and are comparable to the statistical noise of the calibration runs, calibration twists $\vec{\theta}^{\vec{i}}$ are corrected such that

$$\vec{\theta}^{\vec{i}}_{\text{true}} = \vec{\theta}^{\vec{i}}_{\text{meas}} - \vec{a}_{s1} - \vec{a}_{s2}, \tag{7.8}$$

with vector notation indicating that both magnitude and phase were accounted for.

Coupling to other symmetries

Azimuthally periodic mass distributions can have non-vanishing harmonic components at n times the azimuthal symmetry number. Could the 6-fold symmetric leveling and centering mechanisms on the attractor (or 6-fold symmetric hole pattern of the pendulum's calibration tray) also contribute a gravitational torque at 18ω ($n = 3$) and 120ω ($n = 20$)? Or perhaps the pendulum's dominant 4-fold symmetry couple to the 120ω ($n = 30$) signal? The $n = 3$ coupling to 18ω is expected to be the largest (signals vanish exponentially as n increases), and a rough calculation indicates a torque contribution at the $1{\times}10^{-10}$ fNm level, or $\hat{\sigma}_{18} = 3{\times}10^{-8}$ nrad. These effects were therefore negligible.

7.2.2 Magnetic Systematics

A magnetic interaction could torque the pendulum at the signal frequencies through 1) a rotating field sourced somewhere on the attractor, and 2) interaction with a static field sourced either on the pendulum or external to the experiment.

Rotating field

We studied the possibility of a rotating magnetic systematic by measuring the pendulum's response to an exaggerated 1ω field sourced on the attractor. We placed a magnetized washer in the center hole of the attractor, creating a field of 11,400 μGauss at 1ω (with just 270 μGauss at 2ω), as measured with a giant magnetoresistance (GMR) probe approximately 1mm above the attractor and just inside the outer radius of the 120-fold wedges.

The GMR probe was then removed, the vacuum vessel replaced, and the pendulum placed approximately 1mm above the attractor. Turning the attractor with a 1200 sec

period, we observed pendulum twist of 24 ± 6 nrad at 1ω and 35 ± 5 nrad at 2ω. We interpret both signals as arising primarily from the 1ω component of the field, with the 1ω twist resulting from a ferromagnetic coupling of the pendulum to the field, and the 2ω twist from a paramagnetic coupling of the pendulum to the square of the field. With these values we deduce coupling constants $C_{\rm ferro} = 0.003$ nrad/μGauss and $C_{\rm para}$ =3×10^{-7} nrad/μGauss^2.

We then removed the washer and measured the nominal field of the attractor without exaggeration. The probe was placed in the same location as before. We took magnetic field readings for several rotations of the attractor. Fitting the data, we found fluctuations of 0.4 ± 0.2, 0.2 ± 0.2, 0.1 ± 0.1, and 0.1 ± 0.1 μGauss at 9ω, 18ω, 60ω, and 120ω.

The uncertainty in the science data due to this systematic is calculated as

$$\hat{\sigma}_h \leq (B_h + dB_h)\ C_{\rm ferro} + (B_{h/2} + dB_{h/2})^2\ C_{\rm para}, \tag{7.9}$$

where $B \pm dB$ is the GMR probe measurement of the non-exaggerated field and h is the harmonic of the attractor frequency. We find $\hat{\sigma}_{18} \leq 0.0012$ nrad and $\hat{\sigma}_{120} \leq 0.0006$ nrad.

External static field

A static field will induce a magnetic moment proportional to a material's magnetic susceptibility, χ. Tungsten is nominally non-magnetic, with $\chi = 6.8 \times 10^{-5}$. Nonetheless, if the tungsten plates or any components on the attractor and pendulum become magnetized by a constant external field, the magnetic interaction may alter the 120ω and 18ω signals.

To check for this systematic, an external field was applied using a pair of Helmholtz coils. The coils were 64 cm in diameter, separated by 32 cm, with 150 turns each, driven at 1 Amp, producing an additional field at the pendulum-attractor of approximately 4 Gauss. The residual field with the coils off was measured to be < 1 Gauss. Measurements were taken with the field in two perpendicular horizontal directions and with two polarizations in the vertical direction as well as with the field off. Table 7.1 summarizes the results of these measurements.

The exaggeration factor for these systematics is

$$f_e = \frac{B_{\rm on}}{B_{\rm off}} f_s, \tag{7.10}$$

Table 7.1: Summary of the external magnetic field systematics. The $B_{\rm on}$ measurements are the average of up and down for vertical, and the quadrature sum of 0° and 90° for horizontal. All units are nrad (right 4 columns).

direction	harmonic	$B_{\rm on}$	$B_{\rm off}$	$a_e \pm \sigma_e$	$\hat{\sigma}$
vert	120	193.65 ± 2.9	193.24 ± 2.4	0.41 ± 3.77	0.021
	18	160.93 ± 2.2	164.01 ± 2.9	-3.08 ± 3.64	0.034
horiz	120	182.64 ± 3.3	179.81 ± 4.4	2.83 ± 5.51	0.017
	18	151.02 ± 6.8	155.28 ± 3.7	-4.26 ± 7.73	0.024

where f_s is the shielding factor of the mu-metal shield on the vacuum can, which was removed for these tests. Because the mu-metal shield is a cylinder with no end caps, f_s is different for the vertical and horizontal tests. Using the GMR probe, we determined $f_s \approx 125$ in the horizontal direction, and $f_s \approx 50$ in the vertical direction. Therefore, we had $f_e \approx 500$ and $f_e \approx 200$ in the horizontal and vertical directions.

As Table 7.1 indicates, the systematic contribution of an external magnetic field is $\hat{\sigma} < 0.04$ nrad.

7.2.3 Electrostatic Systematics

Although the pendulum was inside a nearly hermetic, grounded Faraday shield, electrostatic cross-talk between the attractor and pendulum is still possible. The worry lies in the elasticity of the beryllium-copper screen separating the attractor from the pendulum. If there is a potential difference V between the attractor and screen, it will exert a force F on the screen

$$F = \frac{1}{2}\frac{\partial C}{\partial z}V^2 \quad \rightarrow \quad F \propto \frac{1}{z^2}V^2, \tag{7.11}$$

where C is the capacitance. Any movement of the screen will alter the local patch-field potential wells at the pendulum and likely cause a torque. Modulation of the screen at or near the 120ω or 18ω signal frequencies could directly interfere with the science signals.

Table 7.2: We investigated the attractor-screen contact potential systematic by applying an additional potential V_{as} and observing the change in signals a_{120} and a_{18}. The average of $V_{as} = \pm 3$V signals are used to determine a_{sys}, with amplification factor $f_e = 1100$. All units are are in nrad.

Signal	$V_{as} = 3$V	$V_{as} = -3$V	$V_{as} = 0$V	a_{sys}	$\hat{\sigma}$
a_{120}	219 ± 5	214 ± 2	217 ± 3	-0.5 ± 3	0.003
a_{18}	170 ± 6	168 ± 8	173 ± 7	-3 ± 8	0.010

Although science data were typically collected with the attractor and screen shorted to one another through BNC cables and grounded through the capacitance meter, multiple dissimilar metal junctions and the long cable lengths can easily produce a contact potential difference. We measured this potential difference by adding a bias voltage to the cap-meter and observed the change in capacitance, and therefore z_a, due to the added force pulling down on the screen (Figure 7.5). We then reversed the cap-meter's leads to provide the reverse bias scenario (the cap-meter does not accept negative bias voltages). The bias voltage of minimum screen deflection corresponded to a contact potential of -50 ± 20 mV. For the purposes of the systematic test, the conservative value of $V_c = -50 - 2 \times 20 = -90$ mV was used.

To exaggerate the contact potential while taking data, we used two AAA batteries ($\pm$3V) with one side connected to screen and ground, and the other connected to the attractor through a 1 megohm resistor. The exaggeration factor for this test is

$$f_e = \text{Mean}\left[\left(\frac{3 \pm 0.09}{0.09}\right)^2\right] = 1100.$$

We set the pendulum to a relatively close separation of $z_p = 50\mu$m (but not closer to achieve better error bars) to ensure sensitivity to screen movement. Table 7.2 details the signal amplitudes observed.

We placed systematic limits by assuming that the induced torque on the pendulum

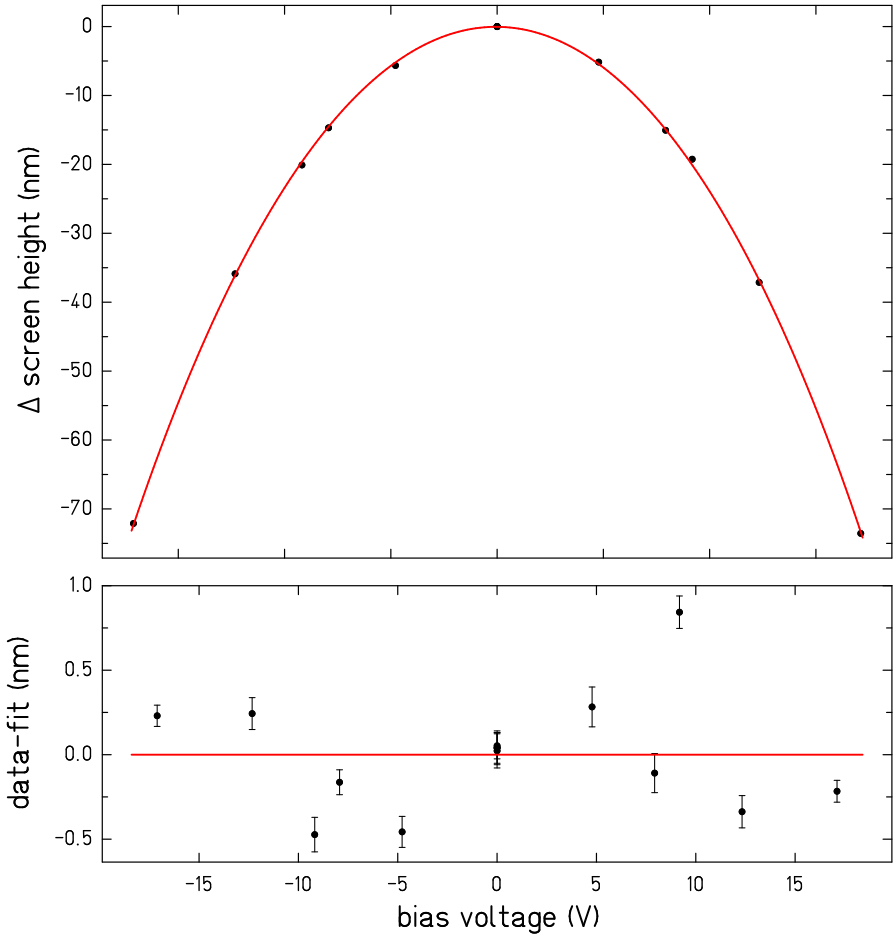

Figure 7.5: The attractor-screen contact potential is measured by applying a bias voltage and observing the deflection of the screen. The data were fitted with the function $\Delta z_a(V_b) = Z_1 + Z_2(V_b - V_c)^2 + Z_3(V_b - V_c)^4$, where V_c is the contact potential. The error bars represent the statistical uncertainty of each measurement, but the scatter of the residuals indicates these error bars are undersized. The best fit gives $V_c = -50 \pm 20$ mV, weighting all data equally.

varied linearly with the applied force on the screen. This test found a negligible systematic error of $\hat{\sigma} = 0.003$ nrad at 120ω, and $\hat{\sigma} = 0.010$ nrad at 18ω.

7.2.4 Temperature Systematics

We considered two thermal effects that could introduce apparent twist signals by changing the equilibrium angle of the torsion fiber, or by deflections of the optical system components. The first was fluctuation of the air temperature inside the thermal enclosure. The air temperature was regulated with a recirculating water bath coupled to a heat exchanger (car radiator) and circulation fans. The temperature of the water bath was locked in feedback to a sensor inside the enclosure. The air temperature couples to the entire apparatus, and the temperature sensor mounted on the autocollimator was used as a proxy for the system's response to changes in air temperature. The second effect investigated was temperature fluctuations of the attractor stepper motor. The motor's temperature was held constant with a Peltier element. The stepper motor coupled directly to the attractor bearing through a shaft, and the in-vacuum temperature sensor located on the attractor-bearing mounting plate was used as a proxy for the system's response to changes in motor temperature.

In looking for a coherent systematic effect, we are only concerned with observed temperature variations that occurred at the signal frequencies in phase with the attractor. Averaging over all science data we observed autocollimator sensor fluctuations of 3.3 ± 1.5 μK at 120ω and 4.3 ± 3.3 μK at 18ω, and plate sensor fluctuation of 0.2 ± 0.2 μK at 120ω and 1.0 ± 1.1 μK at 18ω.

We exaggerated the effects of temperature fluctuations by separately driving the air and motor temperatures sinusoidally at 0.005 Hz, near the typical frequency of the 18ω signal. (The heat capacity of the apparatus made it difficult to modulate temperatures at higher frequencies.) We modulated the air temperature by varying the recirculated water temp by $\pm 1^\circ$ K, which produced a fluctuation in the autocollimator sensor of 16.2 mK ($f_e = 16200/(4.3 + 3.3) \approx 2000$) and induced an apparent twist of 205 ± 3 nrad on the pendulum. The air-temperature systematic contribution is therefore $\hat{\sigma} = 0.10$ nrad. Modulating the motor temp by $\pm 3.5^\circ$ K produced a 140 μK fluctuation in the plate sensor

($f_e = 140/(1.0+1.1) \approx 65$) and induced an apparent twist of 12 ± 2 nrad of the pendulum. The motor systematic contribution is therefore $\hat{\sigma} = 0.22$ nrad. The magnitude of these systematics at the 120ω frequency will necessarily be smaller due to the thermal inertia of the system, so the values described here are conservative upper bounds on the 120ω signal.

7.2.5 Modulated z_p Systematic

A modulation of z_p, with amplitude ζ_m, will couple with the patch-field induced $\Theta_0(z_p)$ (Section 7.1.3) and create a spurious twist

$$\Theta_m(z_p) = \zeta_m \; \Theta_0{}'(z_p), \tag{7.12}$$

where m denotes the harmonic frequency. The driving of ζ_m could be thermal in nature (the thermal tests discussed above were performed at large z_p to avoid coupling to $\Theta_0(z_p)$), or conceivably an alternate mechanism. Regardless, the effect would be evident in the capacitance data collected during our science runs.

Fitting capacitance data from the W3 data set for harmonics at our signal frequencies, and converting to units of z_p, show average amplitudes $\zeta_{18} = 0.22 \pm 0.17$ nm and $\zeta_{120} = 0.33 \pm 0.17$ nm for runs with $z_p < 0.1$ mm. Working from the best fit function found in Figure 7.4, the Θ_0 gradient takes the form

$$\Theta_0{}'(z_p) = -\frac{240}{0.017} \; \exp(\frac{-z_p}{0.017}) \tag{7.13}$$

and has units of μrads/mm. We estimate the largest contribution of this systematic effect (at the smallest value of z_p achieved, 0.033 mm) to be $\hat{\sigma}_{18} = 0.8$ nrad and $\hat{\sigma}_{120} = 1.0$ nrad.

7.2.6 Seismic Systematic

The capacitance modulations observed in the previous section could alternatively be interpreted as modulations in *seismic activity*, rather than literal modulations of z_p. Because the capacitance is nonlinear and the bounce frequency of the pendulum (~ 8 Hz) is fast compared to the integration time of the cap meter, a change in bounce amplitude offsets the capacitance reading similar to a change in z_p.

The capacitance model, $C(z_p)$, when corrected to account for a bounce amplitude β, has the form

$$\bar{C}(z_p, \beta) = C(z_p) + \frac{1}{2}\ \beta^2\ C''(z_p)\ . \tag{7.14}$$

If that bounce amplitude is sinusoidally modulated by $\delta\beta_m$, where m refers to the signal frequency harmonic, the measured capacitance has a modulation amplitude

$$\begin{aligned}\tilde{C}_m(z_p) &= \bar{C}(z_p, \beta + \delta\beta_m) - \bar{C}(z_p, \beta) \\ &= (\beta\ \delta\beta_m + \frac{1}{2}\delta\beta_m^2)\ C''(z_p)\end{aligned} \tag{7.15}$$

Similarly, the twist amplitude induced in the pendulum from bounce amplitude modulation, given the $\Theta_0(z_p)$ function of Section 7.1.3, has the form

$$\tilde{\Theta}_m(z_p) = (\beta\ \delta\beta_m + \frac{1}{2}\delta\beta_m^2)\ \Theta_0''(z_p)\ . \tag{7.16}$$

Combining Equations 7.15 and 7.16 provides the twist modulation without requiring any direct measurement of the bounce amplitude or its modulation:

$$\tilde{\Theta}_m(z_p) = \frac{\tilde{C}_m(z_p)}{C''(z_p)}\ \Theta_0''(z_p)\ . \tag{7.17}$$

If we assume β and $\delta\beta_m$ were effectively constant (i.e. the seismic drivers responsible for these terms did not appreciably change from run to run – especially with respect to z_p), then the ratio $R_m = \tilde{C}_m(z_p)/C''(z_p)$ is constant. We averaged R_m for all runs with $z_p < 0.1$ mm to determine $R_{18} = (4.5 \pm 4.5)\times10^{-9}$ mm^2 and $R_{120} = (8.8 \pm 4.4)\times10^{-9}$ mm^2. We estimate the largest contribution of this systematic effect (at the smallest value of z_p achieved, 0.033 mm) to be $\hat{\sigma}_{18} = 1.1$ nrad and $\hat{\sigma}_{120} = 1.6$ nrad, just slightly greater than the z_p-modulation interpretation of the capacitance data. This effect is not negligible.

7.2.7 Mechanical Systematics

Attractor-Screen Contact

The attractor touching the screen (either directly or by dragging dust caught between the two) can create spurious torques on the pendulum, likely by disturbing the patch-field potentials.

We investigated this effect by intentionally setting the screen alignment so the attractor made significant contact with the screen for about half the rotation. We found that the touching amplified the 18ω signal while it left the 120ω signal relatively unchanged (Figure 7.6). It is probable that the 18ω pattern on the attractor rim is responsible for amplifying the 18ω signal, as it could modulate the screen at that frequency while in contact.

As seen in the uppermost plot of Figure 7.6, attractor-screen touching can also create a 1ω signal in the pendulum-screen capacitance. Looking at the pendulum-screen capacitance data for all of W2, we see a z_p modulation of 14.1 ± 0.4 nm at 1ω (vector average over entire data set), which is 2.5 times larger than observed during W3 (11 times smaller than observed in this test), confirming touching was likely. Additionally, upon disassembly of the apparatus after the W2 data set, we observed a small piece of debris near an 18-fold wedge on the attractor that was likely making contact with the screen during data collection. This test in conjunction with the observed debris strongly implies the anomalies observed in the 18ω signal in the W2 data set may have been a result of attractor-screen touching.

The W1 data set also seems to have spurious 18ω signal. While we do not have pendulum-screen capacitance data and no touching or debris was directly observed, the additional signal measured in that set could also have been a result of attractor-screen contact.

Attractor Friction

As the attractor turns, spurious torques on the apparatus could be produced by friction in the bearing. This could twist the "spider" framework that holds a mirror in the autocollimator optical path and introduce false signal. To check for this systematic, the attractor disk was removed from the bearing assembly, and the assembly rotated at the normal speed. Without the attractor disk in place the pendulum should feel no gravitational torque, but any movement of the mirror should be unchanged.

To obtain a statistical error comparable to our other systematics we ran this measurement for about 15 days. Figure 7.7 shows the best fit for 18ω and 120ω signals in each run. We found resolved signals of 1.7 ± 0.5 and 1.0 ± 0.2 nrads at the 18ω and 120ω frequencies.

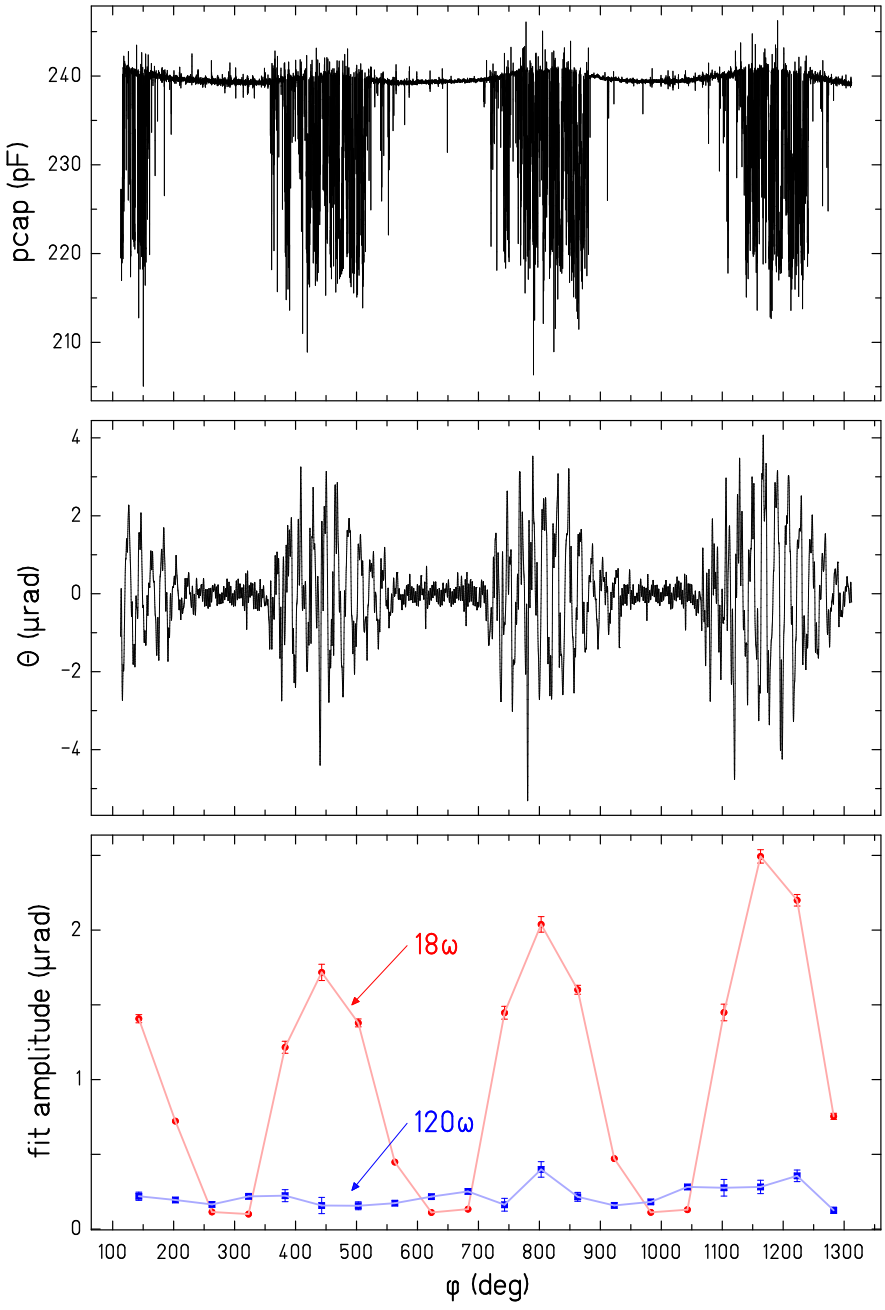

Figure 7.6: The attractor was set to touch the screen for about half a rotation. The capacitance drop-out noise (top) indicates the times of contact (electrical contact to the screen changes the capacitance circuit), and physical displacement of the screen is also seen in the upper limit modulation at 1ω. The touching clearly affects the pendulum oscillations (middle) and amplifies the 18ω signal much more than the 120ω (bottom).

These values are comparable in magnitude to the daily error bars of our science data and were therefore subtracted from the data.

A Fourier analysis of the data collected for this systematic revealed broad peaks at 12ω, 48ω, and 144ω (the 12ω and 144ω peaks responsible for contaminating the 18ω and 120ω signals). During the systematic test we saw 1.9 ± 0.3 nrads at 144ω, and during all of W3 we saw 3.6 ± 0.3 nrads at 144ω, indicating this effect was indeed present during science data.

7.2.8 Systematic Error Accounting

Most systematic effects we investigated can be segregated into those whose magnitude should vary with pendulum height, and those that are independent of pendulum height.

The z_p dependent effects have a variety of functional forms, most of which we do not accurately know, so treating each one independently in the data-fitting routine is not practical (the seismic systematic is an exception, see below). Instead, we treat these effects as though they simply scale with gravity. We determine each systematic's error contribution, $\bar{\sigma}$, by normalizing $\hat{\sigma}$ to the measured signal amplitude in the science data, A, at the z_p the test was performed,

$$\bar{\sigma} = \frac{\hat{\sigma}}{A(z_p)}. \tag{7.18}$$

These errors are then quadrature-summed and used to constrain the parameters that freely scale the gravitational models in the fit. All multiplicative systematic effects are listed in Table 7.3. Overall, we have about 0.04% scaling uncertainty in the 18ω and 120ω signals.

We incorporate the z_p independent effects into the data-fitting model as additional torque vectors (one for 120ω and one for 18ω) whose magnitudes are free to vary within the determined error budget and whose phases are unconstrained. The systematic effects that do not vary with z_p are listed in Table 7.4. We find an additive uncertainty of 0.6 and 0.3 nrad (.002 and .001 fNm) for the 18ω and 120ω signals .

The calibration systematic (Section 7.2.1) is treated as an additional effect (z-independent) in the calibration fit, which extrapolates the calibration constant. The calibration constant uncertainty, though, is synonymous with a multiplicative error and is included in the multiplicative systematic error budget.

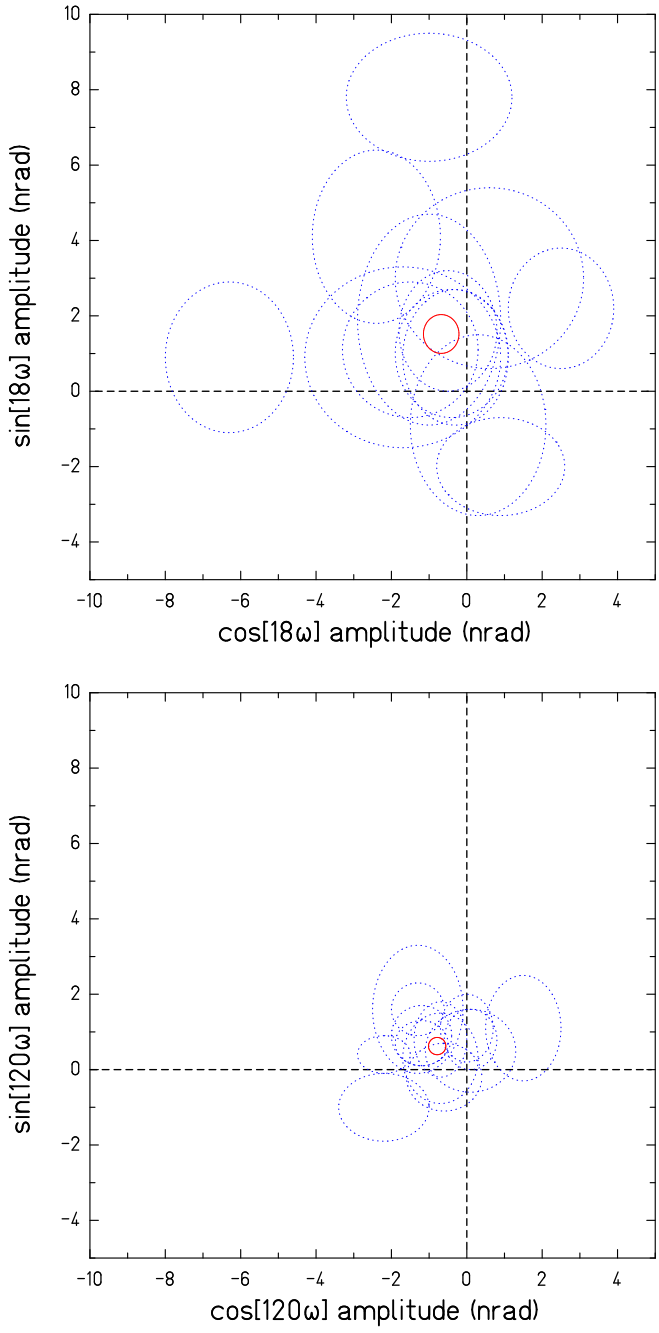

Figure 7.7: Apparent torque on pendulum with attractor disk removed. The dotted ellipses represent the best fit for each run and the solid ellipse is the cumulative average.

Table 7.3: Summary of multiplicative systematic uncertainties for 120ω and 18ω signals. A is the gravitational amplitude for the separation at which the systematic test was performed and $\bar{\sigma}$ is the ratio of $\hat{\sigma}$ to A. $\hat{\sigma}$ and A are in nrad while $\bar{\sigma}$ is unit-less.

Systematic effect	$\hat{\sigma}_{18}$	$\hat{\sigma}_{120}$	A_{18}	A_{120}	$\bar{\sigma}_{18}\times 10^4$	$\bar{\sigma}_{120}\times 10^4$
Gravitational Calibration*	–	–	–	–	3.3	3.3
Rotating Magnetic Field†	0.0012	0.0006	149	160	0.08	0.03
Static Magnetic Field						
Vertical	0.034	0.021	154	195	2.2	1.1
Horizontal	0.024	0.017	152	182	1.6	0.9
Attractor Bias Voltage	0.010	0.003	157	220	0.6	0.1
Total					4.3	3.6

* value extrapolated from model-fit to calibration data

† z_p not well defined for this test, $z_p = 0.1$ mm used

Table 7.4: Summary of additive systematic errors for 120ω and 18ω signals. All units are nrad.

Systematic effect	$\hat{\sigma}_{18}$	$\hat{\sigma}_{120}$
Temperature Fluctuations		
Air*	0.10	
Motor*	0.22	
Mechanical: Friction	0.5	0.2
Total	0.6	0.3

* Upper limit calculated for both frequencies

The seismic systematic (Section 7.2.6) is the one z_p dependent systematic that has an explicit functional form (Equation 7.17), which makes it trivial to include in the fitting model. Accounting for a seismic systematic, then, the torque model is

$$N = N_{\text{grav}} + \alpha N_{\text{yuk}} + \kappa \frac{1}{2} \delta\beta^2 \Theta''(z_p), \tag{7.19}$$

where $\delta\beta$ is a fit parameter. While we analyzed the systematic separately for 18ω and 120ω, we chose to treat them the same in the model as neither was well resolved and it is unknown how robust $\Theta'(z_p)$ was during the W3 data set. Therefore we used $a_z = 0 \pm 0.6$ nm.

Chapter 8

FITTING AND RESULTS

We tested gravity by comparing our measured torques, $N_m(\vec{x}_i) \pm \delta N_m(\vec{x}_i)$ at frequencies $m\omega$, to our model, $\tilde{N}_m(\vec{x}_i, \vec{p})$, where $\vec{x}_i = (x_i,\ y_i,\ z_i)$ is the pendulum position for the ith data run and $\vec{p}$ is an array of adjustable fit parameters. Most of the adjustable fit parameters $\vec{p}$ (listed in Table 8.1) were treated as both free parameters and independent data points. In this way the fit minimizes χ^2 by adjusting their values, but if it attempts adjusting them outside their measured error bars it pays for it with added contributions to χ^2. Additionally, we accounted for uncertainties in the measured pendulum heights, δz_i, by multiplying them by the slope of the torque function and adding that value in quadrature with the measured torque error bars,

$$\delta\bar{N}_m = \sqrt{(\delta N_m(\vec{x}_i))^2 + \left(\delta z_i \frac{d\tilde{N}_m(\vec{x}_i, \vec{p})}{dz|_{z=z_i}}\right)^2} \ . \tag{8.1}$$

8.1 Fitting Functions and Fit Parameters

Our fitting function addressed Newtonian gravity, Yukawa-type new physics, and measured systematics by taking the form

$$\tilde{N}_m(\vec{x}_i, \vec{p}) = \gamma_m \left[\tilde{N}_m^{\rm grav}(\vec{x}_i, \vec{p}) + \alpha \tilde{N}_m^{\rm yuk}(\vec{x}_i, \vec{p}, \lambda)\right] + \tilde{N}_m^{\rm add} + \tilde{N}_m^{\rm seis}(\vec{x}_i, \vec{p}) \ . \tag{8.2}$$

γ_m, $\tilde{N}_m^{\rm add}$, and $\tilde{N}_m^{\rm seis}$ accounted for multiplicative, additive, and seismic systematics, respectively. The Newtonian torque function was

$$\tilde{N}_m^{\rm grav}(\vec{x}_i, \vec{p}) = G\frac{m_p m_a}{t_p t_a \beta_p \beta_a}\ T_m(\phi_m + \pi_i)\ R_m(r_i, r_a, s_i)\ \times \left[\tilde{N}_m(s_i, t_p, t_a, \hat{\rho}_g, \epsilon) + \frac{1}{2}\ [a_m(\theta_{pa})]^2\ \frac{d^2\tilde{N}_m(s_i, t_p, t_a, \hat{\rho}_g, \epsilon)}{ds_i^2}\right], \tag{8.3}$$

where β_p and β_a are the total areas of removed mass from the pendulum and attractor, $r_i = \sqrt{(x_i - x_0)^2 + (y_i - y_0)^2}$, and $s_i = z_i - z_0$, with $\vec{x}_0 = (x_0,\ y_0,\ z_0)$ as the location of the

attractor. $T_m(\phi)$ is a rotation operator that rotates the components of the torque function by $m\phi$. $R_m(r_i, r_a, s_i)$ is the relative torque response for $r_i \neq 0$ (Section 2.3), taking into account the centering misalignment of the attractor, r_a (Section 6.1.2). $\tilde{N}_m(s_i, t_p, t_a, \rho_g, \epsilon)$ is the Fourier-Bessel solution returned from the torque tables (Section 5.3), and the $a_m(\theta_{pa})$ term accounts for angle misalignment between the pendulum and attractor (Section 6.1.6). The Yukawa torque function was identical to Equation 8.3, but with the R and $\tilde{N}$ functions also accepting the Yukawa range, λ, as a parameter.

Our adjustable fit parameters were defined as

- $m_p,\ m_a$: The total missing mass from both the 120-fold and 18-fold slots for the pendulum and attractor respectively.
- $t_p,\ t_a$: The average thicknesses of the pendulum and attractor foils respectively.
- ρ_g : The glue density. The torque tables used the relative glue density, $\hat{\rho}_g \equiv \rho_g\sqrt{(t_p t_a \beta_p \beta_a)/(m_p m_a)}$ because they were were calculated with a tungsten density of $\rho_W = 1$.
- r_a : The centering misalignment of the attractor relative to its axis of rotation.
- θ_{pa} : The angle misalignment between the pendulum and attractor.
- ϵ : The overcut parameter which accounts for roughness of tungsten surfaces cut by the EDM. In addition to being an adjustable parameter of the torque tables, ϵ also effects the calculation of the slot areas β_p and β_a.
- $x_0,\ y_0,\ z_0$: The location of the attractor in terms of pendulum coordinates. $(x_0,\ y_0)$ locates the axis of rotation, and $z_0 \equiv -(z_a + t_s)$ locates the top surface of the attractor, where t_s is the thickness of the electrostatic screen.
- $\phi_{18},\ \phi_{120}$: Arbitrary rotations of the calculations to fit signals in both torque components. The torque data were rotated to nominally place the signals in a single component for the purposes of plotting.
- π_i : Each run has a phase uncertainty associated with the average scatter of phi-refs and the average scatter of equilibrium positions on the detector.
- $\gamma_{18},\ \gamma_{120}$: Multiplicative systematic factors that account for systematic uncertainties that change with pendulum height.

- $(N_{18}^{\mathrm{add}},\ \phi_{18}^{\mathrm{add}})$, $(N_{120}^{\mathrm{add}},\ \phi_{120}^{\mathrm{add}})$: Torque amplitude and phase of systematic uncertainties that are independent of pendulum height.
- $(A_{18}^{\mathrm{seis}},\ \phi_{18}^{\mathrm{seis}})$, $(A_{120}^{\mathrm{seis}},\ \phi_{120}^{\mathrm{seis}})$: z_p modulation amplitude and phase of the seismic systematic.
- λ^{seis} : Length scale of the seismic systematic.

8.2 Final Data Set Analysis

Section 6.5 discussed the analysis pipeline for a single run. The ensemble of the data set received further analysis and manipulation before being fit.

8.2.1 Data Rotation

The measured torque components had a phase relative to the once-per-turn phi-ref mark (which defined zero phase angle) that was arbitrarily set when the attractor was mounted to the bearing. To make plotting and interpretation easier, the data were rotated to place the signal primarily in one in-phase component, with the out-of-phase component nominally measuring zero. A single angle rotated all 120ω data, and a different angle rotated all 18ω data. We did not attempt to constrain the 120ω phase relative to the 18ω phase, though in theory we could have.

These rotations had an effect the quality of fit to data as they mixed the in-phase and out-of-phase error bars; the errors of the two components could start off different sizes but a rotation of 45°, for instance, gives both components the same size error bar. This mixing did not have a significant effect, however, on the limits set by the Yukawa fit.

8.2.2 Phase Uncertainty

Each data run had an adjustable phase parameter, π_i. We surveyed the scatter of average phi-refs per run and the scatter of average pendulum equilibrium position per run to set limits for these parameters. The W3 data set had phi-ref scatter of 1.1 milli-deg and equilibrium angle scatter of 0.8 milli-deg. The π_i parameters were all set to 0 ± 1.5 milli-deg.

8.2.3 z_a Drift

In Figure 6.5, the attractor is seen to drift toward the screen over the course of the W3 data set. This drift was linear with time and corresponded to a 28 nm per day decrease in pendulum-attractor separation. This drift was applied to the data as a modification of the pendulum height, z_i, for each run.

8.3 Results of Newtonian Fit

Our fit to the W3 data set using the Newtonian torque function ($\alpha = 0$) gave a minimized $\chi^2 = 234.2$ with $\nu = 216$ degrees of freedom (DOF). If the Newtonian model truly described the data, the probability that a larger χ^2 would occur by chance is $Q(\chi^2, \nu) = 0.19$. These data consisted of 55 data runs with two measured components for both the 120ω and 18ω torques (220 DOF). There were 75 constrained fit parameters (net 0 DOF) and 4 unconstrained fit parameters (-4 DOF). Table 8.1 lists our measured and fitted parameter values for this fit.

Figures 8.1 and 8.2 show the best fit to the in-phase components of centered and off-center runs, respectively. Though not shown in the plots, the out-of-phase components and 18ω off-center data were also included in the fit of the data.

Table 8.1: The measured and fitted parameter values for the Newtonian fit. The N_σ column is the fitted central value divided by the measured uncertainty. A fitted parameter uncertainty that is less than the measured uncertainty indicates the torque data provided a tighter constraint to that parameter.

Parameter	Measured	Fitted	Units	N_σ
m_p	0.7826 ± 0.001	0.7836 ± 0.0010	g	1.02
m_a	0.7847 ± 0.0005	0.7850 ± 0.0005	g	0.51
t_p	0.0545 ± 0.00105	0.0542 ± 0.0010	mm	0.26
t_a	0.0544 ± 0.00075	0.0542 ± 0.0007	mm	0.30
ρ_g	0.935 ± 0.007	0.933 ± 0.007	g/cm^3	0.34

continued on following page

Table 8.1 continued

Parameter	Measured	Fitted	Units	N_σ
r_a	0.0095 ± 0.005	0.0106 ± 0.005	mm	0.21
θ_{pa}	0.0001 ± 0.00045	0.00008 ± 0.00045	rad	0.04
ϵ	0.00025 ± 0.0002	0.00027 ± 0.0002	mm	0.10
x_0	N/A	-0.2529 ± 0.0026	mm	-
y_0	N/A	-0.3622 ± 0.0032	mm	-
z_0	-0.0293 ± 0.0015	-0.0303 ± 0.0007	mm	0.67
ϕ_{18}	N/A	0.014 ± 0.014	deg	-
ϕ_{120}	N/A	0.0005 ± 0.0019	deg	-
γ_{18}	1.00000 ± 0.00043	1.00018 ± 0.00043	-	0.42
γ_{120}	0.99700 ± 0.00036	0.99698 ± 0.00036	-	0.07
N_{18}^{add}	0.0017 ± 0.0005	0.0019 ± 0.0005	fNm	0.43
ϕ_{18}^{add}	-4.4 ± 0.9	-3.41 ± 0.89	deg	1.10
N_{120}^{add}	0.001 ± 0.0002	0.0010 ± 0.0002	fNm	0.16
$\phi_{120}^{\mathrm{add}}$	-2.04 ± 0.11	-2.03 ± 0.11	deg	0.06
A_{18}^{seis}	0.26 ± 0.26	0.42 ± 0.26	nm	0.62
$\phi_{18}^{\mathrm{seis}}$	7 ± 3	7.7 ± 2.9	deg	0.25
A_{120}^{seis}	0.52 ± 0.26	0.66 ± 0.25	nm	0.55
$\phi_{120}^{\mathrm{seis}}$	-2.37 ± 0.23	-2.46 ± 0.22	deg	0.40
λ^{seis}	0.017 ± 0.001	0.017 ± 0.001	mm	0.17

8.4 Results of Yukawa Fitting

The data favored inclusion of a Yukawa model to the fit. The best fit model was $\lambda =$ 10 mm (the largest value tested), with $\alpha = 0.021 \pm 0.005$, $\chi^2 = 219.0$ ($\nu = 215$ DOF), and $Q(\chi^2, \nu) = 0.41$. These $(\lambda, |\alpha|)$ values fall in a region previously excluded by experiment so are unlikely to be indicative of new physics. That the best fit λ is at long range suggests a

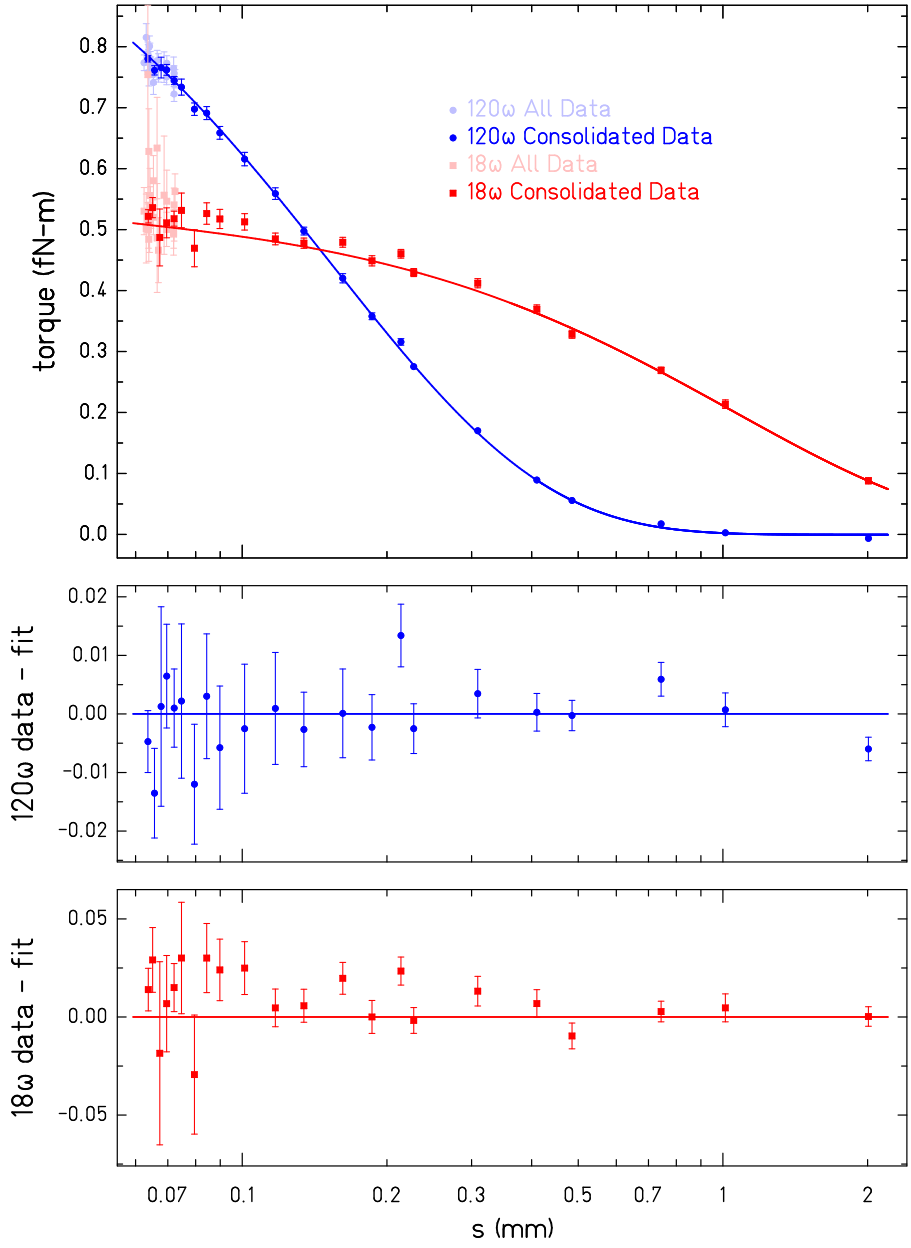

Figure 8.1: Newtonian fit of centered data. Runs at the closest separations have been consolidated merely for plotting purposes by averaging (inversely weighted by the square of error bars) data with s values $< 2\mu$m of each other. From the left, the consolidated points represent the average of (11,5,2,2,5,1...) runs. These plots do not show centering runs or out-of-phase components.

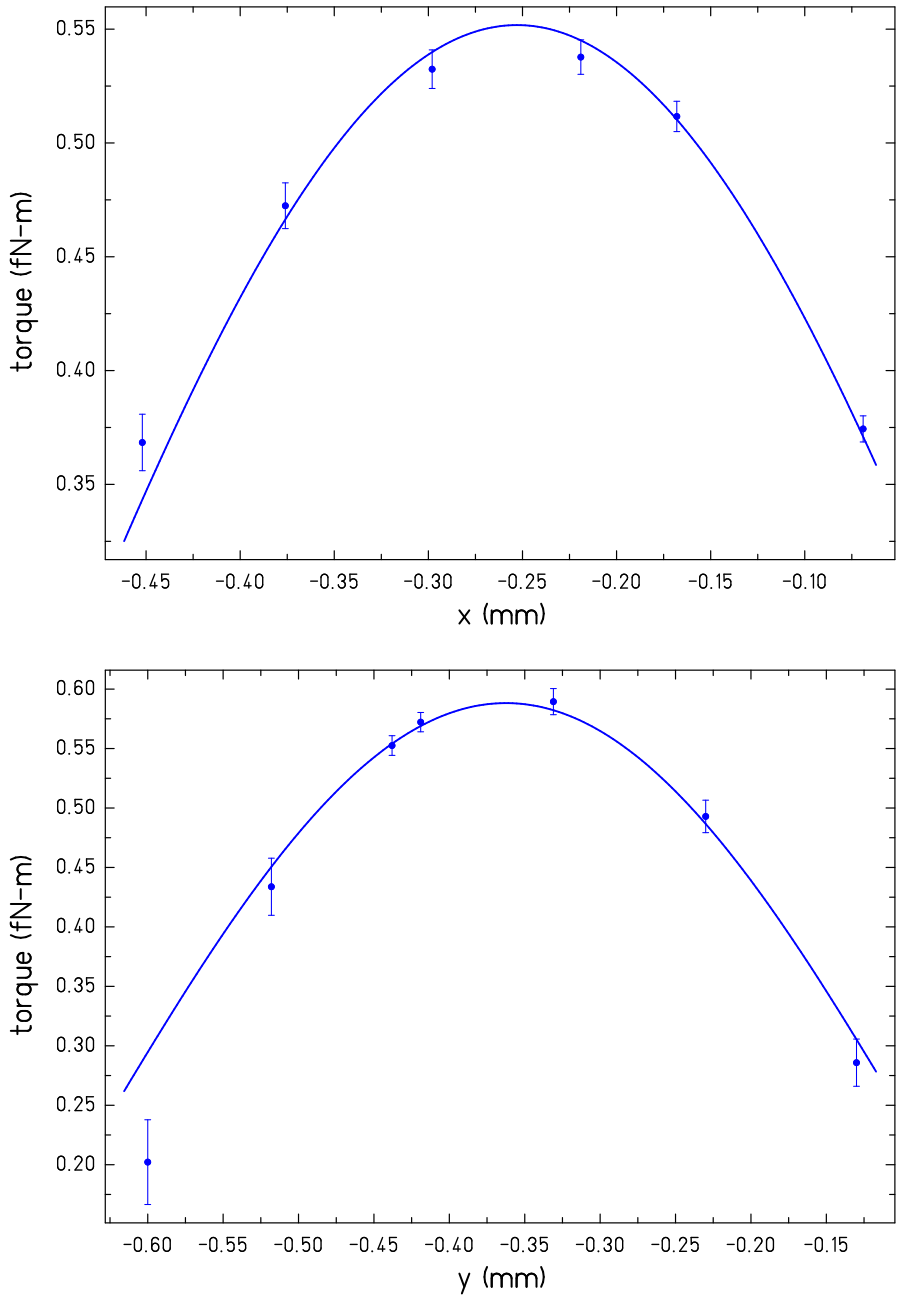

Figure 8.2: Newtonian fit of 120ω off-center data. Centering runs were taken at $s = 0.110$ mm. The variation in error bar sizes was due to spatially varying patch-field potentials.

systematic error in the torque calibration or possibly an error in a parameter measurement. For instance, reducing the measured thicknesses of the tungsten foils by 1 μm (see comment on foil thicknesses in Section 4.4) changes the $\lambda = 10$ mm fit from 4.1σ resolved α to 3.5σ.

To a lesser degree, the data also favored the addition of a short-ranged Yukawa, with a local minimum of $\chi^2 = 229.0$ at $\lambda = 0.070$ mm with $\alpha = -0.13 \pm 0.06$ ($Q(\chi^2, \nu) = 0.24$). Table 8.2 lists the results of Yukawa fits for all λ models tested.

Figure 8.5 shows the 120ω centered data fit with both Newtonian and $\lambda = 0.070$ mm Yukawa models. To see which data most influenced the fits, Figure 8.4 plots the residuals of the fits in terms of their contribution to χ^2, and shows how their contributions changed between the Newtonian and Yukawa fits. Interestingly, one run near $s = 0.2$ mm (a relatively far-away run) experienced the greatest shift in χ^2 contribution, indicating it had a strong influence on the Yukawa fit. Particularly in the Newtonian fit, the run clearly appears to be an outlier relative to the nearby runs. Removing this single run from the data results in a Newtonian $\chi^2/\nu = 1.02$, and a $\lambda = 0.070$ mm fit of $\alpha = -0.093 \pm 0.065$ ($< 2\sigma$ resolved). It also changed the $\lambda = 10$ mm fit to $\alpha = 0.018 \pm 0.005$. There were no abnormalities in any of the data channels for this run, or any other feature we could determine to indicate why it was an outlier, so we have left the run in the data set.

This data provides new 95% exclusion limits on α between $\lambda = 6$ μm and $\lambda = 80$ μm (Figure 8.6). The ISL can now be said to hold down to 42 μm ($\alpha = 1$ limit).

Because α is resolved at $> 2\sigma$ for some values of λ, this data also provides 95% inclusion limits (Figure 8.7). The long-range Yukawa fits are resolved at 4.1σ, and conventionally a 4σ measurement is the minimum resolution for discovery. However, because these values are in previously excluded parameter space it is premature to conclude a positive measurement of new physics.

Table 8.2: Fitting results from Yukawa fitting, showing best-fit α and its uncertainty; the 68% and 95% confidence limits on $|\alpha|$; and the χ^2 and Q from the best fit.

λ (mm)	α_{bf}	$\pm$	σ	$\lvert\alpha_{68}\rvert$	$\lvert\alpha_{95}\rvert$	χ^2	Q
0.005	-1.50×10^7	$\pm$	8.20×10^6	1.92×10^7	2.88×10^7	231.0	0.22
0.01	-2360	$\pm$	1220	2930	4370	230.7	0.22
0.015	-79.9	$\pm$	40.9	99.1	147.3	230.5	0.22
0.02	-12.5	$\pm$	6.3	15.5	22.9	230.3	0.23
0.025	-3.86	$\pm$	1.90	4.75	6.99	230.0	0.23
0.03	-1.70	$\pm$	0.822	2.09	3.05	229.8	0.23
0.035	-0.929	$\pm$	0.442	1.14	1.66	229.6	0.24
0.04	-0.584	$\pm$	0.274	0.712	1.03	229.5	0.24
0.045	-0.404	$\pm$	0.188	0.492	0.712	229.3	0.24
0.05	-0.299	$\pm$	0.138	0.363	0.526	229.2	0.24
0.055	-0.233	$\pm$	0.107	0.283	0.409	229.1	0.24
0.06	-0.188	$\pm$	0.086	0.229	0.330	229.1	0.24
0.065	-0.157	$\pm$	0.072	0.191	0.276	229.0	0.24
0.07	-0.134	$\pm$	0.062	0.163	0.235	229.0	0.24
0.075	-0.116	$\pm$	0.054	0.142	0.205	229.1	0.24
0.08	-0.103	$\pm$	0.048	0.125	0.181	229.1	0.24
0.09	-0.0826	$\pm$	0.0394	0.101	0.147	229.2	0.24
0.095	-0.0751	$\pm$	0.0363	0.0921	0.1348	229.3	0.24
0.1	-0.0687	$\pm$	0.0337	0.0845	0.1242	229.4	0.24
0.125	-0.0472	$\pm$	0.0256	0.0592	0.0894	230.1	0.23
0.15	-0.0344	$\pm$	0.0214	0.0444	0.0696	230.9	0.22
0.175	-0.0255	$\pm$	0.0189	0.0344	0.0566	231.7	0.21
0.2	-0.0188	$\pm$	0.0172	0.0270	0.0470	232.5	0.20
0.25	-0.00798	$\pm$	0.01513	0.0172	0.0334	233.7	0.18

continued on following page

Table 8.2 continued

λ (mm)	α_{bf}	$\pm$	σ	$\lvert\alpha_{68}\rvert$	$\lvert\alpha_{95}\rvert$	χ^2	Q
0.5	0.0182	$\pm$	0.0112	0.0234	0.0366	232.6	0.19
1	0.0261	$\pm$	0.00779	0.0298	0.0389	224.7	0.31
1.5	0.0244	$\pm$	0.0065	0.0274	0.0350	221.6	0.36
2	0.0231	$\pm$	0.0059	0.0258	0.0327	220.5	0.38
2.5	0.0223	$\pm$	0.0056	0.0249	0.0315	219.9	0.39
3	0.0218	$\pm$	0.0054	0.0243	0.0307	219.6	0.40
3.5	0.0215	$\pm$	0.0053	0.0240	0.0302	219.4	0.40
4.5	0.0211	$\pm$	0.0052	0.0236	0.0297	219.2	0.41
5	0.0210	$\pm$	0.0052	0.0234	0.0295	219.1	0.41
5.5	0.0209	$\pm$	0.0051	0.0233	0.0294	219.1	0.41
6	0.0209	$\pm$	0.0051	0.0233	0.0293	219.1	0.41
7	0.0208	$\pm$	0.0051	0.0232	0.0291	219.0	0.41
10	0.0207	$\pm$	0.0050	0.0230	0.0289	219.0	0.41

8.5 Limiting the fit

The error bars on α are due in part to the scatter in the torque data, and in part to the error bars of the fit parameters. To separate these effects, we locked the fit parameters at their best fit values for a given Yukawa potential and re-fit the data with α as the sole adjustable parameter. By doing this the error bar on α is determined purely by the scatter in the torque data.

For the $\lambda = 0.070$ mm potential, the torque-data-only fit gave $\delta\alpha = 0.024$, compared to the combined fit with $\delta\alpha = 0.062$ (as expected, the central value for α was the same in both fits). This indicates a little over half of the overall uncertainty in α results from the uncertainty in our determination of fit parameters. The covariance matrix of the full parameter fit indicates α is most strongly correlated to z_0, with a covariance of -0.74. The

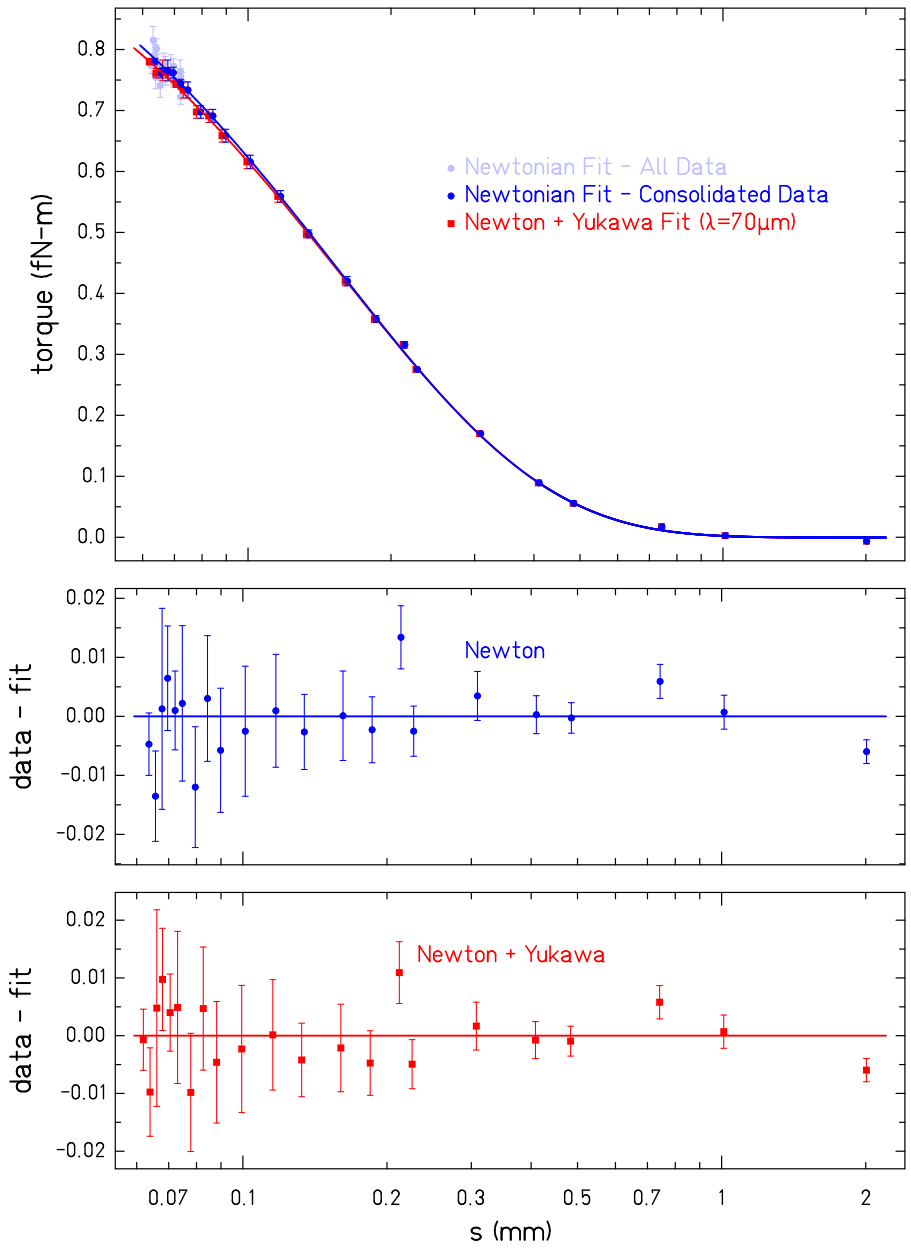

Figure 8.3: Newtonian and Yukawa fits of 120ω centered data. The $\lambda = 0.070$ mm Yukawa potential is the most resolved at short ranges, with $\alpha = -0.13 \pm 0.6$. The Yukawa data points are shifted left because the best fit z_0 changed by ≈ 2 μm.

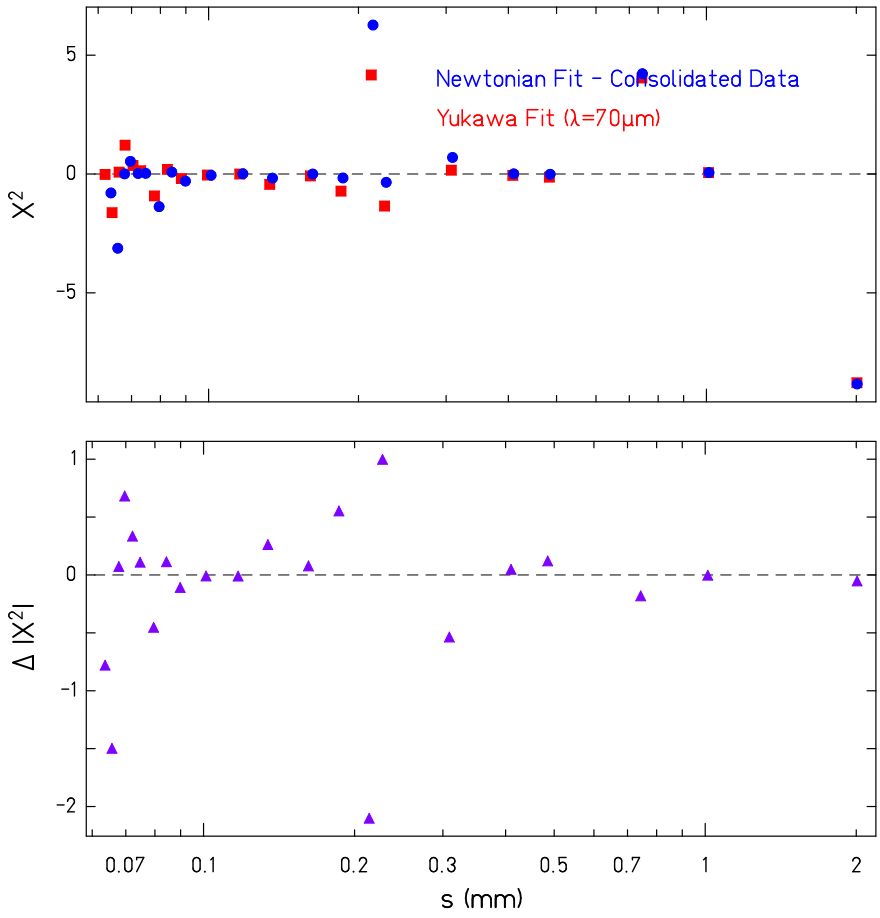

Figure 8.4: 120ω centered data contributions to χ^2 for Newtonian and Yukawa ($\lambda = 0.070$ mm) fits. TOP: The magnitude of each point is the contribution to χ^2 of the data run; the sign matches the sign of the residual, i.e. + sign means points lie above the curve on the torque plot. BOTTOM: The change in χ^2 contribution from Yukawa fitting vs. Newtonian fitting. A negative value indicates the Yukawa fit did a better job fitting that point than the Newtonian fit. The most significant runs driving the Yukawa fit were the two consolidated points at closest separations (16 runs total) and the single run near $s = 0.2$ mm. $\Delta|\chi^2|$ from 120ω off-center runs were all $< |\pm 0.1|$, and 18ω runs were all $< |\pm 1.0|$.

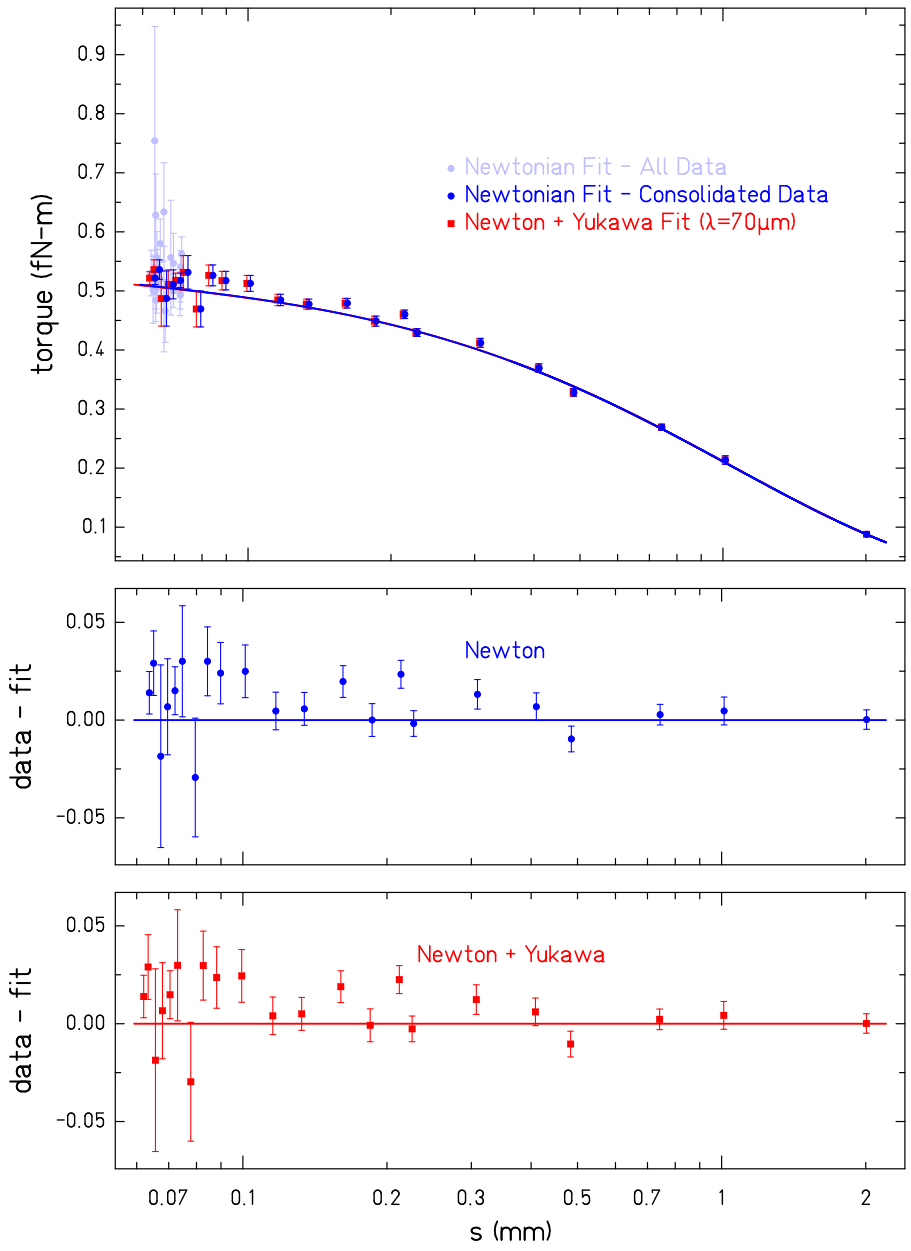

Figure 8.5: Newtonian and Yukawa fits of 18ω centered data. The Newtonian and Yukawa fits are nearly indistinguishable, except for the Yukawa data points shifted left because the best fit z_0 changed by ≈ 2 μm.

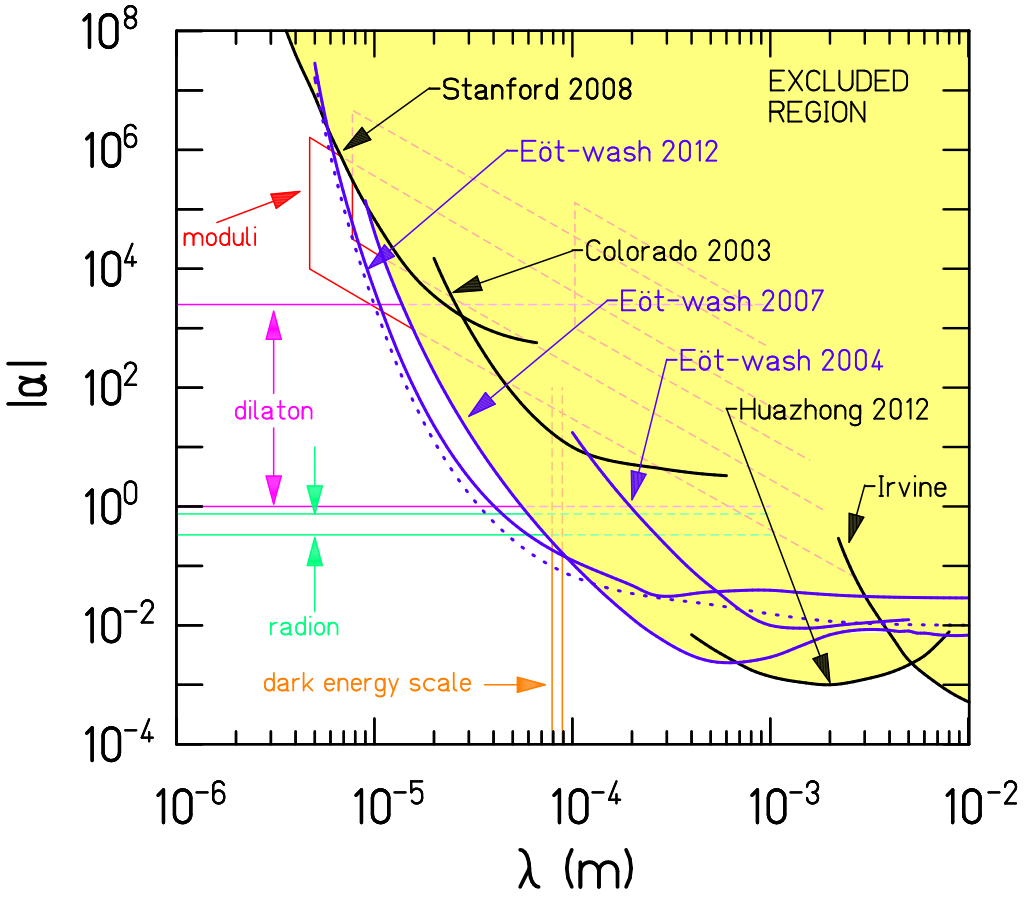

Figure 8.6: 95% Exclusion of Yukawa (λ, α) from the W3 data set. The solid line labeled "Eöt-Wash 2012" represents limits set by this work. The dotted line represents the sensitivity of the experiment, $S(\lambda) \equiv 2\sigma_\alpha$, and indicates the limits we *could have* set if the data did not favor Yukawa contributions.

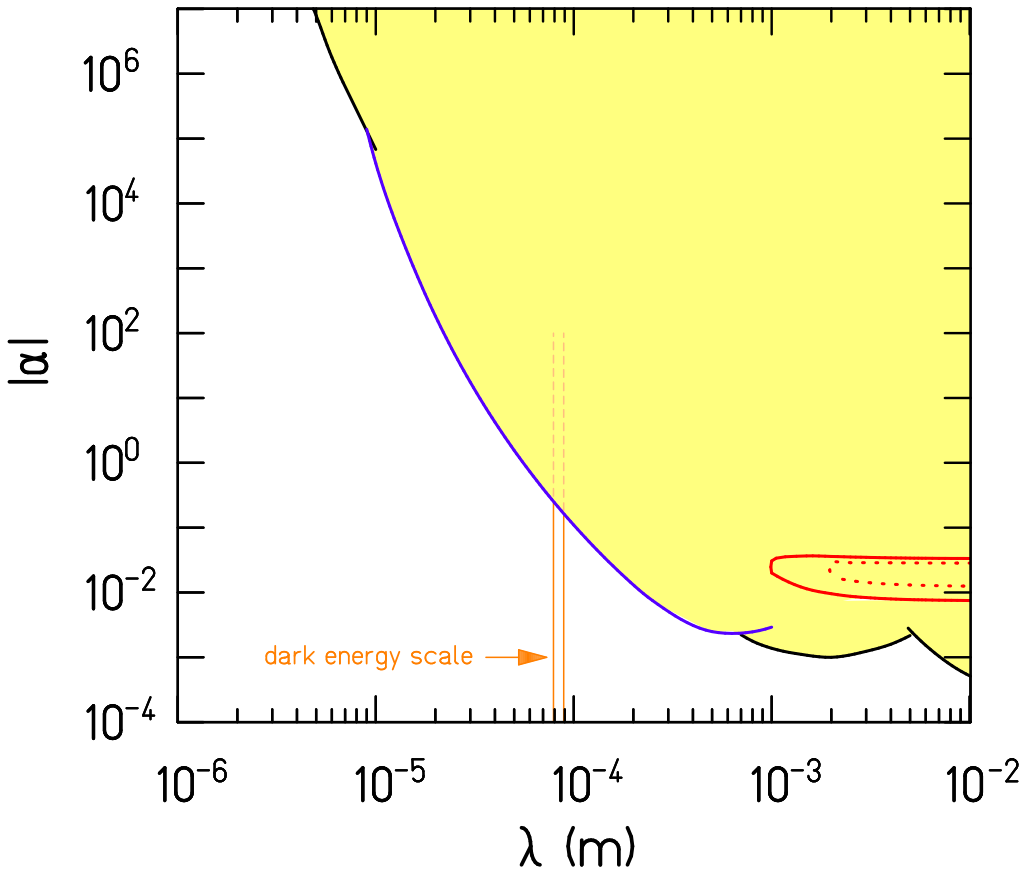

Figure 8.7: 95% (solid) and 68% (dashed) inclusion of Yukawa $(\lambda, |\alpha|)$ from the W3 data set. The inclusion region has been excluded by previous experiment which likely indicates a systematic error in our measurement at long length scales.

next most significant correlations are with $\phi_{120}^{\rm seis}$ (-0.25), t_p (0.18), and t_a (0.11).

Similarly, for the $\lambda = 10$ mm potential roughly half the uncertainty in α comes from the torque data ($\delta\alpha = 0.0024$) and half from the fit parameters (total $\delta\alpha = 0.0050$). The strongest parameter correlations are with z_0 (-0.60), m_p (-0.26), $\phi_{18}^{\rm add}$ (-0.21), t_p (0.20), t_a (0.15), and m_a (-0.13).

Placing better restrictions on these measured values should have a noticeable impact on future α limits.

Chapter 9

CONSIDERATIONS FOR FUTURE MEASUREMENTS

With the experience gained from this measurement, we have identified many areas for improvement in our apparatus design, data collection protocols, and data analysis.

9.1 Apparatus Improvements

- Flat Surfaces for Pendulum and Attractor

  We are developing a new gluing procedure to achieve flat surfaces, absent of craters, bulges, or dishing. This will greatly reduce modeling complexity and, we believe, improve noise performance at small separations.

- Round Outside Edges

  The final inner and outer radii of the tungsten foils will be cut round before gluing them to the Pyrex substrates to avoid repeating the 18-fold rim-protrusion issue.

- Thicker Foils

  To gain sensitivity at longer λ, the pendulum and attractor may utilize 100 μm thick foils instead of the current 50 μm thickness. Placing better limits in the theoretical dark energy regime ($\approx$ 80 μm, which also happens to be where our non-Newtonian signals are most resolved) would favor this change.

- In-vacuum Screen Adjustment

  Being able to adjust the attractor-screen separation after the vacuum system is closed will allow us to achieve the smallest possible values for z_a, as well as more robustly verify the absence of dust and attractor-screen touching. Three motor driven actu-

ators will manipulate the screen height at three points, providing full tip-tilt and z_a adjustment.

- Stiffen Vacuum Can and Optics

  The vacuum can and spider are being replaced with versions considerably larger in radius. This will provide much improved stiffness and hopefully eliminate the observed mechanical systematics.

- New Torsion Fiber

  The current experiment did not take full advantage of the lightweight design of the pendulum. Using a thinner torsion fiber than the 20 μm one currently used will improve the thermal signal-to-noise ratio. This will increase the free-torsion period, however, and may make the measurement more susceptible to low frequency noise sources.

- Modify Calibration Turn Table

  The bearing of the calibration table will be redesigned with a much larger aperture for passing cables to the bottom flange of the vacuum can. This will allow a return to the preferred method of run calibration.

- Motorized Tilt Control

  Motorized control of the apparatus tilt would make leveling procedures less invasive (they currently require opening the thermal box which introduces possible thermal drifts), and possibly allow for tilt corrections that ensure pendulum-attractor alignment remains constant.

- AGI Sensor Thermal Stability

  Implementation of tilt corrections would require a more thermally stable AGI sensor to ensure observed changes in tilt were real and not thermal artifacts. An insulated

box around the AGI and a peltier device with air-cooled heatsink would likely be sufficient.

9.2 Data Collection Improvements

- Foil thicknesses

  The resolved yukawa signals shifted considerably with the average thickness of the tungsten foils changing by merely 1 μm. The foils appear to the eye to have a surface modulation at the $\approx$ 1 mm lateral scale, but we were unable to resolve the vertical structure (thought to be at the 0.5 μm scale) with the AFM (scan area too small) or the SmartScope (resolution inadequate). Measuring this structure may have a significant impact for the interpretation of the next experiment.

- Full-time attractor-screen capacitance monitoring

  We found that monitoring the pendulum-screen capacitance full-time provided highly valuable data, leading to deeper understanding of our noise issues. It would be similarly valuable, particularly with the addition of dynamic attractor positioning, to monitor the attractor-screen capacitance with an independent LCR meter.

- Multiple z-scans

  The interpretation of capacitance data to determine z_p is a key feature of the experiment, but we have traditionally based this model wholly on a single collection of z-scan data. Given that the bounce of the pendulum is a necessary fit parameter in this model, and we know the bounce amplitude has day-night variation, a single z-scan seems inadequate. Taking z-scans under various conditions (day, night, weekend), and periodically through the course of a data set would provide more confidence in the accuracy of z_p determination.

- Tilt monitoring

Monitoring AGI levels and making necessary adjustments periodically will prevent long timescale temperature drifts of the apparatus from altering the pendulum's xy-alignment to the attractor.

- Continuous Calibration

  A continuous calibration signal removes ambiguity in the non-linearity correction procedure.

- Increased attractor rotation

  Particularly at close separations, noise spectra (Figure 7.1) indicate increased attractor speed would bring the 18ω signal to a lower noise floor without adversely effecting the 120ω noise.

9.3 Analysis Improvements

- Higher-order filtering

  Using 3rd-order interpolation, instead of linear interpolation, in the torsion filter will reduce contamination of fitted twist amplitudes due to data spacing that is incommensurate with the filter spacing. It should also provide improved performance when the true torsion period significantly differs from the value used to set data timing.

- Rotate runs before fitting twists

  The current method of data rotation mixes the error bars of the two orthogonal signal components which should be uncorrelated (Sec. 8.2.1). A preferred method would be to offset the interpreted location of phi-ref by the desired angle and re-fit the runs. This would allow for all the signal to appear in a single component without artificially convolving the error bars. Choosing a single angle that achieves this rotation for both the 120ω and 18ω signals would allow further constraints during fitting and may help reveal systematic errors.

- Dynamic $Z_p(C)$ fitting

The fit parameter most sensitive to different Yukawa models is z_0. z_p and z_0 are determined by fits to capacitance models that have their own set of free parameters and it is unknown how those parameter may correlate with α. It would be preferable to fit z-scan data and gravitational data simultaneously so any correlations are properly accounted.

Appendix 1

LIST OF RESOURCES

A.1 Personal contact info

Feel free to contact me with any questions regarding this thesis at:

tedcook@gmail.com

(206) 550-9372 (cell)

A.2 Computer programs and files

Table A.1: Computer resource locations

Fitting program	`\\kepler2\c\EWSR\code\fitting`
Fourier Bessel Monte Carlo 120ω	`\\kepler2\c\EWSR\code\fbmc`
Fourier Bessel Monte Carlo 18ω	`\\kepler2\c\EWSR\code\fbmc18`
Cartesian Monte Carlo 120ω	`\\kepler2\c\EWSR\code\wmc`
Cartesian Monte Carlo 18ω	`\\kepler2\c\EWSR\code\wmc18`
Program to build torque tables	`\\kepler2\c\EWSR\code\WedgeModel`
Spreadsheet of all data sets	`\\kepler2\c\EWSR\fitdata\Wedge_All.xls`
Pendulum body design	`\\kepler2\c\tpc\wc`
COMSOL models	`\\cavendish\Users\TedC\Comsol`
Solidworks models and renderings	`\\cavendish\Users\TedC\Documents`
Autocad drawings	`\\kepler2\C\Ted\ShortRange\Drawings`
SmartScope data	`\\smartscope\Partrtn\ted_cook`
Miscellaneous files and analysis	`\\kepler2\c\Ted\ShortRange`
This thesis	`\\kepler2\c\Ted\ShortRange\Thesis`

A.3 Hardware suppliers

Table A.2: Hardware suppliers

Mirror cubes and Pyrex disks	`www.redoptronics.com`
Tungsten foils	`www.alfa.com`
BeCu foils	Micro-Tek Associates Inc., Diamond Bar, CA
Ceramic ball bearings	`www.vxb.com`
Rotary encoder system	`www.microesys.com`
SmartScope service	`www.roscoprecisionmachinery.com`
Integral E100 adhesive film	`www.dow.com`

BIBLIOGRAPHY

[1] C.D. Hoyle, D.J. Kapner, B.R. Heckel, E.G. Adelberger, J.H. Gundlach, U. Schmidt, and H.E. Swanson. Sub-millimeter tests of the gravitational inverse-square law. *Physical Review D*, 70(042004), 2004.

[2] N. Arkani-Hamed, S. Dimopoulos, and G. Dvali. The hierarchy problem and new dimensions at a millimeter. *Phys. Lett. B*, 429, 1998.

[3] S.R. Beane. On the importance of testing gravity at distances less than 1cm. *Gen.Rel.Grav.*, 29, 1997.

[4] R. Sundrum. Fat gravitons, ,the cosmological constant, and sub-millimeter tests. *Physical Review D*, 69, 2004.

[5] Amol Upadhye, Steven S. Gubser, and Justin Khoury. Unveiling chameleon fields in tests of the gravitational inverse-square law. *Physical Review D*, 74, 2006.

[6] D.J. Kapner, T.S. Cook, E.G. Adelberger, J.H. Gundlach, B.R. Heckel, C.D. Hoyle, and H.E. Swanson. Tests of the gravitational inverse-square law at the dark-energy length scale. *Phys. Rev. Lett.*, 98(021101), 2007.

[7] Frank V. Marcoline. *Calculating torques on pendula due to Yukawa, $\sigma.r$ and $\sigma.\sigma$ interactions.* Find internally at CENPA: `kepler/for/ew/fbessels.pdf`,2004.

[8] W.H. Press, S.A. Teukolsky, W.T. Vetterling, and B.P. Flannery. *Numerical Recipes in C*. Cambridge University Press, 1996.

[9] Daniel J. Kapner. *A Short-Range Test of Newton's Gravitational Inverse-Square Law*. PhD thesis, University of Washington, 2005.

[10] Charles D. Hoyle, Jr. *Sub-millimeter Tests of the Gravitational Inverse-Square Law*. PhD thesis, University of Washington, 2001.

[11] Peter R. Saulson. Thermal noise in mechanical experiments. *Physical Review D*, 42(8), 1990.

[12] S. Schlamminger, C.A. Hagedorn, and J.H. Gundlach. Indirect evidence for Lévy walks in squeeze film damping. *Physical Review D*, 81(123008), 2010.

VITA

Ted Cook was born in Arcadia, California on June 21, 1977 and grew up outside of Denver, CO. He received both a B.S. in Phyiscs (May 2000) and a M.S. in Physics (May 2002) from Baylor University. He began work with the Eöt-Wash Gravity group in June, 2002 and entered the University of Washington Ph.D. program in September of that same year. On September 3, 2006 he was married to his lovely wife, Bethany. On April 18, 2009 they welcomed their first daughter, Darcy Ann, and on February 14, 2012 they welcomed their fist son, Samuel James. Ted began working for Micro Encoder Inc. in Kirkland, Washington in May of 2013.